



Central University of Technology, Free State

**Residual stress of Ti6Al4V (ELI) parts
manufactured by direct metal laser
sintering
-Ian van Zyl-**

Dissertation Submitted in fulfilment of the requirements for the degree

**MAGISTER TECHNOLOGIAE ENGINEERING:
MECHANICAL**

Supervisor: Prof. Ihar Yadroitsau, D. Eng.
Co-supervisor: Dr. Ina Yadroitsava, Ph.D.

Bloemfontein



February, 2016

Declaration of Independent Work

DECLARATION WITH REGARD TO INDEPENDENT WORK

I, *Ian van Zyl*, identity number [REDACTED] and student number [REDACTED], do hereby declare that this research project submitted to the Central University of Technology, Free State (CUT, BFN) for the MAGISTER TECHNOLOGIAE DEGREE ENGINEERING: MECHANICAL, is my own independent work; and complies with the code of Academic integrity, as well as other relevant policies, procedures, rules and regulations of the Central University of Technology, Free State; and has not been submitted previously to any institution by myself or any other person in fulfillment of the requirements for the attainment of any qualification.

SIGNATURE OF STUDENT.....DATE.....

Acknowledgements

I would like to thank both my supervisors Prof. Ihar Yadroitsau (Igor Yadroitsev) and Dr. Ina Yadroitsava for not only their guidance but also their timeous input into shaping my approach to scientific research. All the hours spent together in the office as well as their kind patience towards me. I also want to acknowledge the help of various individuals who by their kindness helped me along the way they are in no specific order, Dr. J.G. van der Walt, Prof. W.B. du Preez, Johan Els and Gerrie Booysen. Family and friends for their support throughout, Grobler and Schutte families, G. Levenson, E.B. Newby, A. Nel, A. Kinnear and “Die Presidensie”.

This work is based on the research supported by the South African Research Chairs Initiative of the Department of Science and Technology and National Research Foundation of South Africa (Grant №97994) and the Collaborative Program in Additive Manufacturing (Contract №CSIR-NLC-CPAM-15-MOA-CUT-01).

I dedicate this book to my parents, Adriaan and Noeline van Zyl, their love and support as well as sacrifice is something that cannot be quantified, but I can only strive towards.

Finally and most prominently I want to give honour and prominence to the Lord Jesus Christ, He is the purpose behind every step.

*“For My thoughts are not your thoughts, nor are your ways My ways,”
says the Lord.*

*“For as the heavens are higher than the earth, so are My ways higher
than your ways, and My thoughts than your thoughts.”*

Isaiah 55:8-9

Abstract

This study focuses on the residual stress in Ti6Al4V (ELI) parts manufactured by direct metal laser sintering (DMLS). During DMLS a laser beam scans over the powder layer thus melting the powder and previous layer. High-concentrated energy input leads to high thermal gradients. The track-by-track, layer-by-layer nature of DMLS technology and the thermocycling of the process leads to complex stress distribution and deformation of parts during manufacturing.

A literature review of the DMLS process is given; the capabilities of DMLS are overviewed, and a practical medical solution is demonstrated as a prominent market component of DMLS and its capabilities.

Types of residual stress, its origin and effect on the performance of materials are described. Focus is given to the methods for quantitative and qualitative determination of residual stress in DMLS objects. The thermal gradient and shrinkage play a vital role in the development of residual stresses. Methodology for the investigations of the microstructure, roughness, deformation and microhardness of the specimens are outlined.

Experiments which were conducted with their respective results are included, the results being scrutinized as well as the relevant interpretation to reach adequate scientific conclusions. Relative comparisons are also done in terms of received data and literature. Some numerical simulations are done for predictive and comparative purposes. The results show high values of residual stress in Ti6Al4V (ELI) specimens produced by DMLS. The residual stresses in samples with successively increasing thickness and in primitive 3D components were investigated. It was found that volumetric and shape relations in terms of residual stress and DMLS objects exist.

Applied post process heat treatment is adequate in relieving the majority of residual stress. The sensitivity of Ti6Al4V (ELI) alloy to interstitial elements is also indicated in the data during heat treatment. The consequences of residual stress experienced during this study demand creative solutions for the purpose of a wider application of this technology. Some promising directions for further investigation of residual stress in DMLS objects based on the study's findings are done.



Key words: DMLS, Titanium Alloy, Ti6Al4V, Residual Stress, Microstructure,

XRD

Table of Contents

Declaration of Independent Work	ii
Acknowledgements	iii
Abstract	iv
Table of Contents	v
List of Figures	viii
List of Tables	xii
Glossary	xiii
Nomenclature	xiv
Publications and Presentations to Date	xv
Chapter 1: Introduction	1
1.1. Background	1
1.2. The Aim of the Project	1
1.3. Thesis Statement	1
1.3. The Scope of the Project	2
1.4. Research Methodology	2
1.5 Objectives	3
1.6. Expected Contribution	3
Chapter 2: Literature Review	4
2.1. Introduction	4
2.2. Direct Metal Laser Sintering	6
2.2.1. Laser Processes During DMLS	8
2.2.2. Parameters Influencing DMLS	11
2.2.3. Single Track Formation	11
2.2.4. Single Layer Formation	14
2.2.5. 3D DMLS Object Density	18
2.2.6. 3D Functional Components	21
2.2.7. Summary	22



2.3. Residual Stress	22
2.3.1. Types of Residual Stress.....	22
2.3.2. Origin of Residual Stress and its Effect on the Performance of Materials.....	23
2.3.3. Definitions of the Stresses	28
2.3.4. Residual Stress Measurements.....	29
2.3.5. Summary	39
2.4. Residual Stress in DMLS objects	39
2.4.1. Origin and Cause of Residual Stress in As-built DMLS Specimens	39
2.4.2. Stress-Relieving Treatment of DMLS Specimens.....	51
2.4.3. Summary	53
Chapter 3: Material and Methods	58
3.1. Ti6Al4V (ELI) alloy	59
3.2. Ti6Al4V (ELI) powder characterization	64
3.3. Design of Specimens	65
3.4. Manufacturing of the samples by EOSINT M280 system	67
3.5. XRD Measurements of Residual Stress	67
3.6. Cantilever Curvature Method Analysis	69
3.7. Metallographic Analysis of Microstructure and Porosity	71
3.8. Deformation Estimation (3D Scanning of Specimens)	73
3.9. Surface Roughness Testing	74
3.10. Micro-Hardness Testing	75
3.11. Stress Relieving of Ti6Al4V parts	76
3.12. Oven Inert Box Design and Implementation	77
3.13. Simulation of the Heat Transfer for DMLS	78
3.14. Summary	80
Chapter 4: Results and Discussion	81
4.1. Temperature evaluation and microstructure of Ti6Al4V DMLS samples	81
4.2. Principal residual stresses measured by XRD	88
4.2.1. Residual stress in the samples with successively increasing thickness.....	89
4.2.2. Residual stress in 3D samples with different shapes	94
4.3. Cantilever Curvature Method	98
4.4. Hardness Test and Mechanical Properties	107



4.5. Stress Relieving in Inert Atmosphere	108
4.6. Summary.....	111
Chapter 5: Conclusion and Future work	114
Chapter 6: References.....	117
Appendix 1. Cross-section (in the building direction) of the middle block of the cantilever.....	126
Appendix 2. Normal and principal stresses near the surface in Ti6Al4V (ELI) DMLS samples	128
Appendix 3. Roughness of the top surface of DMLS samples (μm).....	138
Appendix 4. Vickers microhardness of as-built samples ($\text{HV}_{0.3}$)	139
Appendix 5. Vickers microhardness of stress-relieved samples	140
Appendix 6. Mechanical properties of as-built horizontal samples.....	141
Appendix 7. Mechanical properties of the stress-relieved samples.....	143

List of Figures

Fig. 2.1.1. Screenshot of CAD software that is used in AM technology (Solidworks Interface).	4
Fig. 2.1.2. A compressor wheel for a turbocharger being machined from a piece of billet material as an example of subtractive manufacturing.	5
Fig. 2.1.3. Craniofacial implant model using CAD for patient specific application (Jardini <i>et al.</i> , 2014).	5
Fig. 2.1.4. DMLS object manufactured layer by layer from powder material.	6
Fig. 2.2.1. Schematic of DMLS process (Additevely Ltd, 2013).	7
Fig. 2.2.2. EOSINT M280 machine as used by the CUT (EOS GmbH).	7
Fig. 2.2.3. Maxilla and mandible implants produced by DMLS in CRPM at Central University of Technology, 2014.	8
Fig. 2.2.4. Principle of fibre laser (Lackner, 2008).	9
Fig. 2.2.5. Normal-incidence reflectivity of metals as function of wavelength (Gray, 1972).	9
Fig. 2.2.6. Optical absorption depths for several materials over a range of wavelengths (Lide, 2001).	10
Fig. 2.2.7. Factors influencing on DMLS process (Klocke <i>et al.</i> , 2003; Yadroitsev, 2009).	11
Fig. 2.2.8. Single track formation (Yadroitsev, 2009).	12
Fig. 2.2.9. Cross-sections of laser sintered tracks from SS grade 904L ($-16 \mu\text{m}$) powder. Thickness of the deposited powder layer is $50 \mu\text{m}$, effective power input per unit speed $P/V = \text{const}$. (Yadroitsev, 2009).	12
Fig. 2.2.10. Cross section of a single track with metal powder on a steel substrate (Yadroitsev <i>et al.</i> , 2010).	13
Fig. 2.2.11. Single tracks at the substrate (a); single layer (b) and 3D DMLS objects (c).	13
Fig. 2.2.12. Surfaces of the first layer from SS grade 904L powder obtained at different hatch distances. Powder layer is $50 \mu\text{m}$ thickness, laser power is 50 W, and scanning speed is 0.14 m/s (Yadroitsev, 2009).	15
Fig. 2.2.13. Laser sintered thin walls from SS grade 316L powder. Thickness of powder layers varied from 40 to $80 \mu\text{m}$ with a step of $10 \mu\text{m}$, 20 layers for each thickness, $V=0.04-0.18 \text{ m/s}$, $P=50 \text{ W}$ (Yadroitsev, 2009).	15
Fig. 2.2.14. Different scanning strategies (patterns) of a single layer.	16
Fig. 2.2.15. Top view of single layer produced by one-zone (a) and two-zone strategy (b) of laser scanning. $P = 50 \text{ W}$; $h = 50 \mu\text{m}$; $V = 0.12 \text{ m/s}$; $s = 120 \mu\text{m}$ (Yadroitsev <i>et al.</i> , 2015).	16
Fig. 2.2.16. Different scan patterns for consistent layers: a) one direction b) double scanning each layer c) alternating scanning d) the direction of scanning rotated of certain angle between consecutive layers (Manfredi <i>et al.</i> , 2014).	17
Fig. 2.2.17. Schematic of the island scan strategy (Qiu <i>et al.</i> , 2013)	17
Fig. 2.2.18. Schematic showing the band/strip strategy.	18
Fig. 2.2.19. Top view of EOSINT M280 Band/Strip scanning strategy.	18
Fig. 2.2.20. Difference in density at different laser power for al 316L Stainless Steel (Meier & Haberland, 2008).	19
Fig. 2.2.21. Algorithm for optimal DMLS process parameters (Yadroitsev <i>et al.</i> , 2015).	20
Fig. 2.2.22. Caged lower jaw section developed patient specifically at CRPM from Ti6Al4V via DMLS.	21
Fig. 2.2.23. X-ray photo of DMLS Ti6Al4V jawbone (CRPM, 2015).	21
Fig. 2.3.1. Residual stress categorised according to characteristic length scales (Withers & Bhadeshia, 2001).	23
Fig. 2.3.2. Residual stresses arise from misfits (eigen strains) either between different regions or between different phases within material: different types of residual macro and micro residual stress are illustrated (Withers & Bhadeshia, 2001).	24
Fig. 2.3.3. Origin of residual-stress formation (Hauk, 1977).	25
Fig. 2.3.4. Effect of residual stress on the performance of materials (Totten <i>et al.</i> , 2002).	26
Fig. 2.3.5. Comparison of stress distributions. (a) Typical stress distribution in surface of metal beam, unloaded by exhibiting residual tensile stress from normal fabricating procedures. (b) Same beam after shot peening, still without external load. Surface stress is now compressive. (c) Beam, when subjected to design loading, still shows some residual compressive stress at surface (Totten <i>et al.</i> , 2002).	28
Fig. 2.3.6. Stresses acting on an elemental unit cube (Fitzpatrick <i>et al.</i> , 2005).	29

Fig. 2.3.7. Sign convention for shear stress - (a) Positive, (b) negative (Fitzpatrick <i>et al.</i> , 2005).	29
Fig. 2.3.8. Showing the different crystal structures of metals (Britannica, 2015).	31
Fig. 2.3.9. Basal-a, prismatic-a, pyramidal-a slip systems, and first- and second-order pyramidal c+a slip systems in HCP materials (Balasubramanian & Anand, 2002).	31
Fig. 2.3.10. A sketch representation of Bragg's Law (Britannica, 2015).	32
Fig. 2.3.11. Diffraction patterns of Ti6Al4V powder and spark plasma sintered Ti6Al4V foams (Quan <i>et al.</i> , 2012).	33
Fig. 2.3.12. HDM (Lambda Technologies, 2012).	34
Fig. 2.3.13. Experimental set-up for ESPI measurements of strains relaxed by hole drilling (Barile <i>et al.</i> , 2014).	35
Fig. 2.3.14. The Contour Methods theoretical implementation (Olson <i>et al.</i> , 2015).	36
Fig. 2.3.15. Curvature of Cantilever due to Residual Stress (Buchbinder <i>et al.</i> , 2014).	36
Fig. 2.3.16. Proposed deformation (a–c); Actual indentation (d–e), (Totten, 2002).	37
Fig. 2.3.17. Weld macrostructure, shown plotted on the same distance scale as the hardness profile and transverse strain gradient across a line 1 mm below the weld toe (James <i>et al.</i> , 2007).	38
Fig. 2.4.1. Thermal Expansion Curves for several metals (Kay, 2010).	40
Fig. 2.4.2. Tensile strengths of a number of alloys as a function of temperature to indicate temperature ranges over which different alloy systems may be used (Key to Metals AG, 2015).	41
Fig. 2.4.3. Schematic showing Heating and Cooling phenomena of laser passes (Kruth <i>et al.</i> , 2003).	41
Fig. 2.4.4. Graphical representation of the stress related measurements, σ_1 and the curl-up angle α in function of selected material properties (Vrancken <i>et al.</i> , 2013).	42
Fig. 2.4.5. Re-Scanning of SLM samples (Shiomi <i>et al.</i> , 2003).	43
Fig 2.4.6. Scanning strategies (Zaeh & Branner, 2010).	43
Fig. 2.4.7. Residual stress in cantilevers (Zaeh & Branner, 2010).	44
Fig. 2.4.8. Island Scan strategy with real image to the right (Qiu <i>et al.</i> 2013).	44
Fig. 2.4.9. Short scan tracks (Kruth <i>et al.</i> , 2012).	45
Fig. 2.4.10. Part Orientation of DMLS components on substrate (Vrancken <i>et al.</i> , 2013).	45
Fig. 2.4.11. Residual stress in samples manufactured by DMLS with different orientation (Vrancken <i>et al.</i> , 2013).	45
Fig. 2.4.12. H-Geometry samples produced by DMLS (Sanz & Navas, 2013).	46
Fig. 2.4.13. a) Residual stress measured at different points on an Iconel 718 part surface produced by DMLS, b) Residual stress measured at different points on a Maraging Steel part surface produced by DMLS (Sanz & Navas, 2013).	47
Fig. 2.4.14. Stresses shown to increase with the height of DMLS samples (Merzelis <i>et al.</i> 2006).	48
Fig. 2.4.15. Residual stress shown to be highest in the top layers (Casavola <i>et al.</i> , 2009).	48
Fig. 2.4.16. Relationship between residual stress and temperature of base plate (Shiomi <i>et al.</i> , 2003).	49
Fig. 2.4.17. Residual stress in Ti6Al4V DMLS samples <i>versus</i> preheating temperature (Vrancken <i>et al.</i> , 2015)	50
Fig. 2.4.18. (a) Microstructure of DMLS Ti6Al4V component without preheating (b) and with 400°C preheating (Vrancken <i>et al.</i> , 2015).	50
Fig. 2.4.19. Relationship between residual stress in top layer of model and heating temperature in stress relieving treatment (Shiomi <i>et al.</i> , 2003).	51
Fig. 2.4.20. Relationship between time and amount of residual stress relief at various stress-relief anneal temperatures for Ti6Al4V alpha-beta alloy (Donachie, 2000).	52
Fig. 2.4.21. Crack Growth Performance (Leuders <i>et al.</i> , 2012).	53
Fig. 2.4.22. Microstructure of Ti6Al4V DMLS samples: as-built (a), heat treated at 800°C (b), after HIP (c), after HIP at 1050°C (d) (β -phase in green) (Leuders <i>et al.</i> , 2012).	53
Fig. 2.4.23. The delamination of Ti6AL4V DMLS part from the support structures during manufacturing.	54
Fig. 2.4.24. Powder bed disturbance.	55
Fig. 2.4.25. Recoater blade contact with DMLS object, scrape marks seen as 'polished' area.	55
Fig. 2.4. 26. Crack propagation throughout DMLS object produced from Ti6Al4V.	56
Fig. 2.4.27. Longitudinal orientated rectangular blocks as-built (still attached to substrate).	56
Fig. 3.1.1. Flow Diagram showing the processes followed during this study.	58

Fig. 3.1.2. A titanium connecting rod for an internal combustion engine (AMT, 2015).	59
Fig. 3.1.3. Thermal expansion coefficient of Ti6Al4V <i>versus</i> temperature. (Dynamet Holdings Inc., 2015).	60
Fig. 3.1.4. Comparison of typical ultimate tensile strengths of selected titanium alloys as a function of temperature (Donachie, 2000).	60
Fig. 3.1.5. Temperature-dependent density (a), heat capacity (b) and thermal conductivity (c) of Ti6Al4V alloy (Mills, 2002; Boivineau <i>et al.</i> , 2006).	61
Fig. 3.1.6. The type of crystal structure formation for different cooling rates of Ti6Al4V (Dabrowski, 2011).	62
Fig. 3.1.7. Wrought Ti6Al4V (Murr <i>et al.</i> , 2009).	63
Fig. 3.2.1. Particle size distribution of employed Ti6Al4V powder. Powder particles were spherical (a), some of them had small satellites (b).	64
Fig. 3.2.2. SEM photos of employed Ti6Al4V ELI powder (SE mode) with different magnification: 100x (a) and 400x (b).	65
Fig. 3.3.1. Rectangular specimen (16) design interface.	65
Fig. 3.3.2. DMLS specimens design.	66
Fig. 3.5.1. ProtoXRD employed by NMMU.	68
Fig. 3.5.2. Substrate with parts and identification for different points of measurements (red dots) samples.	69
Fig. 3.6.1. Cantilever's geometry (for specimen №24).	69
Figure. 3.6.2. Cantilevers for curvature method (8 specimens).	70
Fig. 3.6.3. DMLS Ti6Al4V (ELI) cantilevers on the base plate.	70
Fig. 3.7.1. Struers CitoPress-1 (a) and polishing machine Tegramin-25 (b).	72
Fig. 3.7.2. Method used for polishing titanium alloy (Struers, 2015).	72
Fig. 3.7.3. (a) Optical microscope (CUT) and (b) SEM (utilised at UFS).	73
Fig. 3.8.1. Kreon Ace 7-Axis Scanner (a) and scanning of the samples (b).	74
Fig. 3.9.1. Mitutoyo SJ-210 on top of substrate with samples.	75
Fig. 3.10.1. FM-700 microhardness tester.	76
Fig. 3.12.1. Oven inert box.	78
Fig. 4.1.1. Temperature gradient for cross-section of the track along scanning direction at $t=0.004$ s (a) and temperature profile for point at the top surface $x=4.8$ mm during laser scanning of the Ti6Al4V sample with the length of 1 cm, the laser power density of 19.1 kW/mm ² and the scanning speed of 1.2 m/s.	81
Fig. 4.1.2. Microstructure of the as-built Ti6Al4V (ELI) sample at different cross-sections: xy (a), yz (b) and xz (c) planes.	83
Fig. 4.1.3. SEM image of the martensitic microstructure of as-built Ti6Al4V (ELI) sample.	84
Fig. 4.1.4. Temperature profiles (point $x=0.5$ mm, depth $z=0$ and 80 μ m) during back-and-forth laser scanning of the Ti6Al4V sample with length of 1 cm, laser power density of 19.1 kW/mm ² and scanning speed of 1.2 m/s.	84
Fig. 4.1.5. Martensitic microstructure of as-built Ti6Al4V (Cain <i>et al.</i> , 2015).	85
Fig. 4.1.6 Microstructure of the as-built and stress relieved Ti6Al4V (ELI) sample in different planes: xy (a), zx (b), zy (c).	87
Fig. 4.1.7. Microstructure of stress relieved Ti6Al4V sample (Cain <i>et al.</i> , 2015).	87
Fig. 4.2.1 Principle residual stresses for each Ti6Al4V (ELI) sample produced by DMLS.	89
Fig. 4.2.2. Principal stresses near the surface in 10 x 10 mm square Ti6Al4V samples with 0–40 layers in height. Powder layer thickness is 30 μ m.	90
Fig. 4.2.3. Residual stresses are coaxial with the scanning direction of the top layer of the DMLS samples.	90
Fig. 4.2.4. XRD data for residual stress in cantilever near the surface.	91
Fig. 4.2.5. Second principal stress near DMLS surface <i>versus</i> Rz .	92
Fig. 4.2.6. Residual stresses on the top surface (white) and in depth of 15-80 μ m (grey colour).	94
Fig. 4.2.7. As-built DMLS cubes produced with/without support structures	94
Fig. 4.2.8. Residual stress measured via XRD of cubes and layer samples produced via DMLS.	95
Fig. 4.2.9. a) The three points of measurement, delamination from the substrate circled; b) Measured Residual stress for the three points.	95

Fig. 4.2.10. Comsol simulation of residual stresses at the top surface in the parts $3 \times 1.5 \times 0.3$ ($x \times y \times z$ mm ³) without / with imperfections. Initial stress $\sigma_{xx}=600$ MPa, $\sigma_{yy}=900$ MPa, $\sigma_{xy}=\sigma_{xz}=25$ MPa (Yadroitsava & Yadroitsev, 2015).	96
Fig. 4.2.11. Residual stress near the surface in 3D DMLS objects.	97
Fig. 4.2.12. XRD data for residual stress in cantilever near the surface.	97
Fig. 4.3.1. Numerical simulation of the cantilevers with/without different upper blocks (a) and displacements of the cantilevers in z direction (b).	99
Fig. 4.3.2. Samples after separation with EDM, the deflection clearly visible.	100
Fig. 4.3.3. Measured deflection of the samples <i>versus</i> thickness of the bar on the arm of the cantilever.	100
Fig. 4.3.4. Von Mises resulting stress of the cantilevers with increasing volume.	101
Fig. 4.3.5. Special mounting for the massive samples at the substrate.	101
Fig. 4.3.6. Von Mises stress and deflection in z direction (μm) of the square samples <i>versus</i> the number of layers.	103
Fig. 4.3.7. Von Mises stress and deflection in z direction of the rectangular samples <i>versus</i> the number of layers.	105
Fig. 4.3.8. Von Mises stress for six-layer sample (a) and deflection in z direction of the complex samples <i>versus</i> the number of layers (b).	106
Fig. 4.3.9. Distortion of the thin long part of the sample during manufacturing.	107
Fig. 4.4.1. Indentations in the xy (a) and zx cross-sections (b). Building direction is z axis.	107
Fig. 4.5.1. Oxide layer formed during stress relieving heat treatment of Ti6Al4V sample without Inert Box.	109
Fig. 4.5.3 Medical implant showing slight discoloration after stress relieving at 650°C for 3 hours.	109
Fig. 4.5.4. Cantilevers after stress relieving (left arm didn't curl up after stress-relieving heat treatment).	110
Fig. 4.5.5. Indentations in zx cross-section of stress-relieved sample. Building direction is z axis	110

List of Tables

Table 2.3.1. Origin and cause of Residual stress during manufacturing (Totten et. al., 2002)	25
Table 2.3.2. Methods of Measurement (Withers & Bhadeshia, 2001)	38
Table 2.4.1. Heat Treatment of wrought Ti6Al4V (Dynamet-Holdings, 2000).	52
Table 2.4.2. Deflection due to residual stress	56
Table 3.1.1. Physical and mechanical properties of wrought Ti6Al4V alloy (Aero, 2015)	63
Table 3.2.1. Chemical composition of Ti6Al4V powder (in weight %)	64
Table 3.5.1. Parameters used for the X-ray analysis	68
Table 4.2.1. Principle Stresses via XRD	88
Table 4.3.1. Deflections of the cantilevers	100
Table 4.5.1. Tensile properties of as-built DMLS samples	108
Table 4.5.2. Tensile properties of stress-relieved DMLS horizontally built samples	111

Glossary

3D – Three Dimensional
AM – Additive Manufacturing
ASTM – American Society for Testing Materials
BCC – Body Centred Cubic
CAD – Computer Aided Design
COMSOL – Software platform for simulating physics-based problems
CRPM – Centre of Rapid Prototyping and Manufacturing
CSIR - Council for Scientific and Industrial Research
CTE – Coefficient of Thermal Expansion
CUT – Central University of Technology
DMLS – Direct Metal Laser Sintering
EBM – Electron Beam Melting
EDM – Electrical Discharge Machine
ELI – Extra Low Interstitial
EOS – Electro Optical Systems
ESPI – Electronic Speckle Pattern Interferometry
EU – European Union
FCC – Face Centred Cubic
HAZ – Heat Affected Zone
HCP – Hexagonal Close Packed
HDM – Hole Drilling Method
HIP – Hot Isostatic Pressing
HV – Vickers Hardness
IPS – Invariant Plane Strain
RP – Rapid Prototyping
RS – Residual Stress
SEM – Scanning Electron Microscope
SLM – Selective Laser Melting
UTS – Ultimate Tensile Strength
UFS – University of the Free State
XRD – X-ray Diffraction

Nomenclature

A	Absorption coefficient
c_p	Specific heat capacity
d	Inter-atomic spacing
h	Layer thickness
I	Intensity
k	Thermal conductivity
l	Average diagonal length of an indentation
P	Laser power
Q	Heat generated per unit volume
R	Surface reflectivity of material
S	Surface area
s	Hatch distance
T	Temperature
t	Time
V	Laser scanning speed
θ	Diffraction angle
λ	Wavelength
ρ	Density
σ	Principal stress
ϕ	Face angle of the pyramidal diamond indenter

Publications and Presentations to Date

- I. van Zyl, I. Yadroitsava, I. Yadroitsev. Residual Stress in Ti6Al4V objects produced by Direct Metal Laser Sintering, *RAPDASA 16th International Conference*, 3-5 November 2015, Pretoria – Gauteng, South Africa (*submitted to The South African Journal of Industrial Engineering*).
- I. Yadroitsev, I. van Zyl, M.G. Moletsane, I. Yadroitsava. Direct Metal Laser Sintering of Ti6Al4V (ELI) Powder, *International Conference on Competitive Manufacturing*, 27-29 January 2016, Stellenbosch - Western Cape, South Africa.
- I. van Zyl, I. Yadroitsava, I. Yadroitsev (2015). Residual stresses in direct metal laser sintered parts, *INTERIM*, 14 (1), pp. 11-23.
- I. van Zyl, I. Yadroitsava, I. Yadroitsev. Residual stress in objects manufactured by direct metal laser sintering, *Light Metals Technology Conference 27-29 July 2015*, Port Elizabeth, South Africa (*poster*).

Chapter 1: Introduction

1.1. Background

Direct Metal Laser Sintering (DMLS) produces objects using a layer-by-layer method in which powder is deposited in a thin layer; a laser beam then scans over the powder surface fusing powder particles and also the previous layer. A new powder layer is delivered over the sintered material, the laser beam then scans the new layer thereby producing a 3D-object. Due to the nature of manufacturing, as-built DMLS parts have anisotropy of mechanical and structural properties. High-concentration of energy input leads to high thermal gradients which induce residual stress. High residual stress causes some anomalies: part geometry deviation, formation of cracks and also detachment from the supports and the building platform. Deformations, cracks, delamination of the parts from the substrate and the supports are likely to occur during manufacturing. The residual stress depends on material properties; geometry of the samples and support structures; process parameters as energy input, powder layer thickness, scanning strategy, hatch distances, building strategy, preheating during manufacturing, etc. To comply with medical standards (ASTM F136-13) and become accepted in practice, metal implants created by DMLS must be shown to have a microstructure and mechanical properties comparing with that of wrought material which have been successfully implemented in the medical industry. The analysis of the values and directions of the stresses is a vital issue for providing reliable functional properties of DMLS objects.

1.2. The Aim of the Project

The aim of this study is to quantify the residual stress in Ti6Al4V (ELI) components, produced by DMLS using standard Electro Optical Systems (EOS) process parameters, its' origin and also the effectiveness of current post-processing treatments to relieve detrimental residual stress.

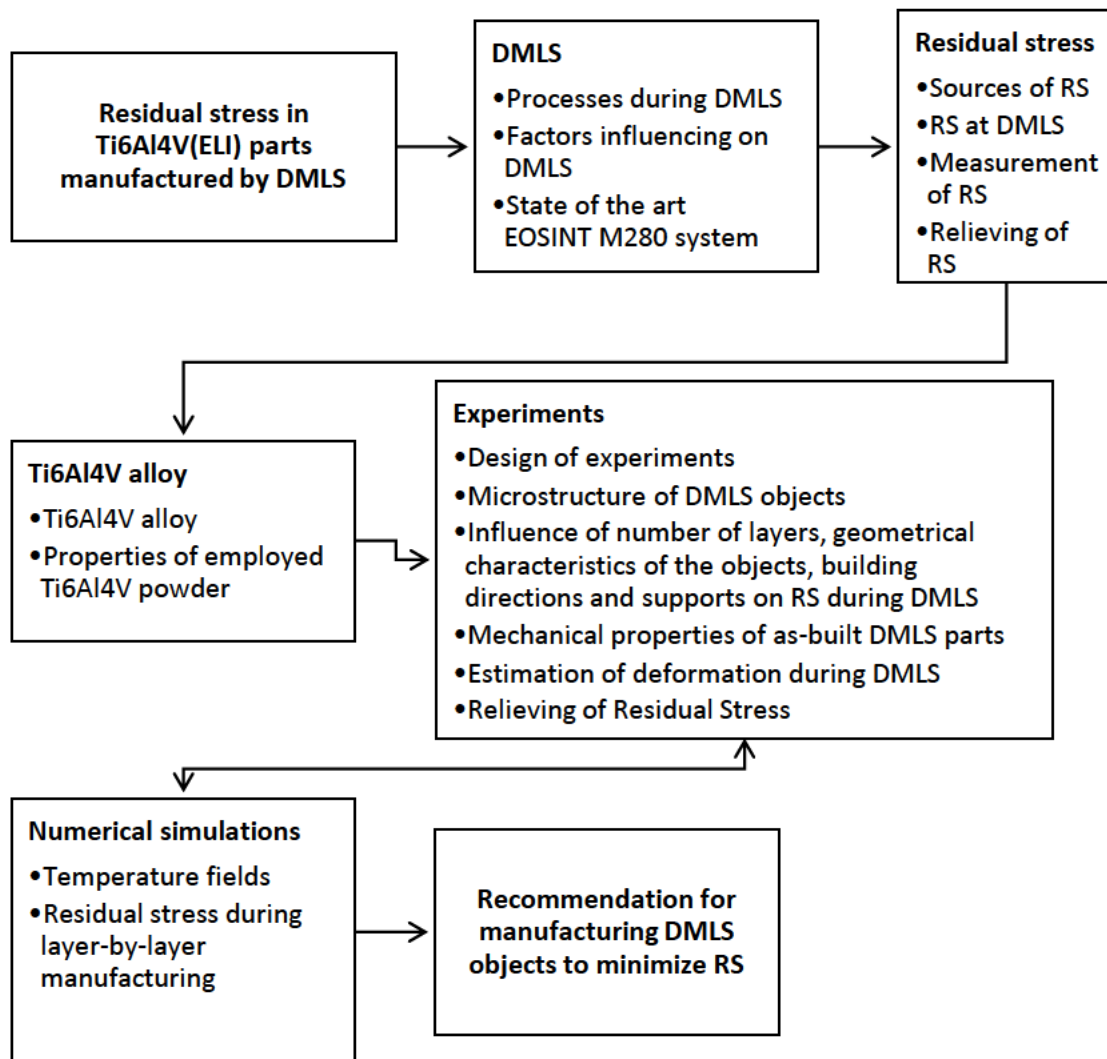
1.3. Thesis Statement

The residual stress in Ti6Al4V (ELI) components, produced by DMLS using standard EOS process parameters, can be fully relieved through heat treatment, resulting in compliance with the internationally accepted standards and mechanical properties for medical implants.

1.3. The Scope of the Project

This research study is concerned to create an understanding of residual stress in Ti6Al4V (ELI) parts manufactured by DMLS, it can be applied not only for the Ti6Al4V powder, but also for other metallic materials used in DMLS.

1.4. Research Methodology



1.5 Objectives

- Studying the DMLS process and powder characterisation
- Analysis of the sources of residual stress during DMLS
- Simulation of residual stress and temperature distribution
- Studying the equipment for residual stress investigations
- Determine the microstructure and the residual stress in as-built Ti6Al4V (ELI) experimental parts built by the EOSINT M280 DMLS with standard process parameters
- Stress relieving heat treatment for Ti6Al4V (ELI) alloy
- Determination of the residual stress in stress relieved DMLS parts
- Recommendation of optimal stress relieving process for DMLS implants from Ti6Al4V(ELI)

1.6. Expected Contribution

This dissertation attempts to add to the body of knowledge on residual stress in DMLS/SLM with an in-depth look into the origin and management of residual stress. The detrimental residual stress limits the effectiveness in the application and qualification of niche market products and materials. So in this work different approaches of measurement and interpretation are utilized to bring forth a more holistic understanding on the matter of residual stress.

Chapter 2: Literature Review

2.1. Introduction

The term ‘*manufacturing*’ as a concept is quite broad, but in essence it is developing products or solutions to meet specific consumer needs. Since the 1900's manufacturing has embodied a premium place within strong economies as seen in the industrial revolution. Effectively meeting needs has become of paramount importance in any successful business entity that operates by means of production. It is important for any manufacturing entity to know and exploit the capabilities of new technology and development within its field to remain relevant and competitive in the 21st century.

Additive manufacturing (AM) is a relatively new technology from its development in the 1980's (excluding early steps in the 1900's), up to the present day AM has developed at a rapid rate. AM is the *"process of joining materials to make objects from 3D model data, usually layer upon layer, as opposed to subtractive manufacturing methodologies"* (ASTM F2792-12A). AM as a technology was spawned out of the necessity to manufacture parts directly from CAD (Computer Aided Design; see Fig. 2.1.1), originally (and possibly at present) the major manufacturing methods used was subtractive in most industries (Fig. 2.1.2), where wrought material would be taken and machined, to form the desired geometry of a component (Kim *et al.*, 2014; Lou & Grosvenor, 2012).

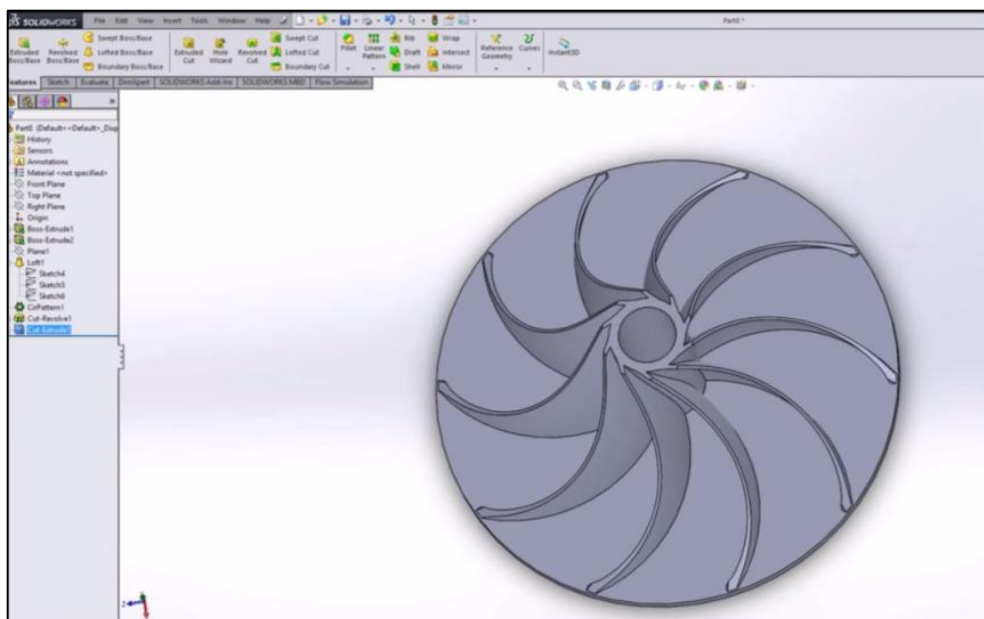


Fig. 2.1.1. Screenshot of CAD software that is used in AM technology (Solidworks Interface).



Fig. 2.1.2. A compressor wheel for a turbocharger being machined from a piece of billet material as an example of subtractive manufacturing.

In the AM industry and its related processes it is possible to practice, CAD-to-part manufacturing, this has greatly influenced small scale prototyping and is starting to influence low volume production. CAD-to-part (all involved processes) manufacturing minimises time needed for a prototype to be built, but also cuts costs because there is minimal wastage of material (Scudamore *et al.*, 2014; Lou & Grosvenor, 2012). Unique custom craniofacial implant designed by CAD for DMLS process shows the CAD-to-part reality of the AM industry, as seen in Fig. 2.1.3.



Fig. 2.1.3. Craniofacial implant model using CAD for patient specific application (Jardini *et al.*, 2014).

There are multiple advantages with AM technology over traditional manufacturing. Geometric possibilities unobtainable by machining or post processing of wrought material, is possible with AM technology due to the layer by layer deposition. As mentioned waste is limited in AM as only the amount of material needed for the component is used, also material that was uninvolved in the process, in most instances, can be re-used (Fig. 2.1.4). AM is considered a ‘green’ technology, as the manufacturing process to obtain a final product consumes less energy than that of traditional subtractive production (Kim *et al.*, 2014).



Fig. 2.1.4. DMLS object manufactured layer by layer from powder material.

In today's society the implementation of 'green' technologies are of absolute importance. Environmental conservation is at the forefront of global focus, the truth of atmospheric and habitat damage is disconcerting. This is also one of the reasons that AM technology is gaining global focus and investment and was recently noted as a key emerging market (Du Preez & De Beer, 2015).

AM technologies are increasing in the development of different materials, low cost machines and new avenues for application of the technology; swift progress has resulted in a lack of fundamental design quality processes. As the AM technology moves forward most likely standardization will soon follow (Gao *et al.*, 2015).

2.2. Direct Metal Laser Sintering

American Society for Testing and Materials (ASTM) defines DMLS as “ *a powder bed fusion process used to make metal parts directly from metal powders. Powder bed fusion is described as an additive manufacturing process in which thermal energy selectively fuses regions of a powder bed* ” (ASTM F2792-12a). A DMLS machine produces parts using a layer by layer method in which loose powder is laid down in a thin layer, a controlled laser beam passes over the powder fusing the powder together (Fig. 2.2.1), a new layer of powder is then laid down over the previous layer, the laser beam then passes over the new layer sintering the layers together (Gu & Shen, 2009).

'Sintering' was used to describe the first type of the layer manufacturing processes because the materials used did not melt completely as it activated a binding agent present in the powder to create a 'green' part. The green part was then subsequently post-processed by

heating and infiltration to produce a high-density metal part. Since the invention of selective laser sintering, much progress has been made in process specific DMLS machines. DMLS, Selective Laser Melting (SLM), Laser Cusing are terms now used interchangeably in industry. Currently the biggest market holder of DMLS equipment production is EOS GmbH, 3D Systems, Concept Laser, Real Lazer, SLM Solutions, Renishaw. Some of these systems are active in the National Program for Additive Manufacturing (CPAM) in the RSA, where Stellenbosch University has a Concept Laser M2 system, the National Laser Centre at the Centre for Scientific and Industrial Research (CSIR) in collaboration with Aerosud is developing a platform known as ‘Aeroswift’ and the Central University of Technology utilizes two EOSINT M280 machines (Fig. 2.2.2).

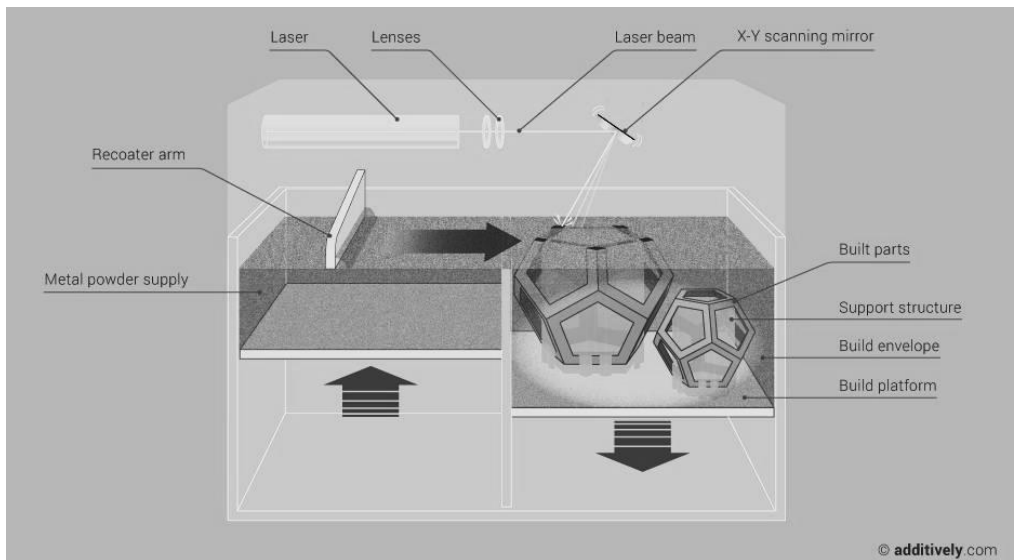


Fig. 2.2.1. Schematic of DMLS process (Additevely Ltd, 2013).



Fig. 2.2.2. EOSINT M280 machine as used by the CUT (EOS GmbH).

It is possible to produce fully dense parts with DMLS. The advantage is that a complex geometric topology can be produced which enable production of custom once-off components, for example bio-medical implants. DMLS can produce parts within hours no extra tooling is required, these parts are also high in detail and quality depending on the parameters used. DMLS holds some benefits with respect to other AM and traditional manufacturing technologies namely: low material wastage, wide possibilities in production inputs and virtually net shaped manufacturing of complex functioning parts as seen with implants in Fig. 2.2.3.



Fig. 2.2.3. Maxilla and mandible implants produced by DMLS in CRPM at Central University of Technology, 2014.

The ability to respond immediately, precisely and relatively inexpensively draws DMLS to the forefront of mainstream low volume production. Advances in this sector have the capability to bridge the gap between prototype and production scenarios. DMLS has more to offer than just complex geometries and prototyping, but offers the market a new way of producing components otherwise impossible, meeting the exact market need (Bertol *et al.*, 2010).

2.2.1. Laser Processes During DMLS

The energy source utilized in modern DMLS systems for metal powder are fiber lasers. Fiber lasers are usually lasers with optical fibers as gain media (Fig. 2.2.4). In most cases, the gain medium is a fiber doped with rare-earth ions, such as erbium (Er^{3+}), neodymium (Nd^{3+}), ytterbium (Yb^{3+}), thulium (Tm^{3+}) or praseodymium (Pr^{3+}). Pumping is performed by one or several laser diodes, where the pump light is coupled coaxially or by

spliced fibers (Lackner, 2008). Commercially available AM laser systems have up to 5 kW laser power.

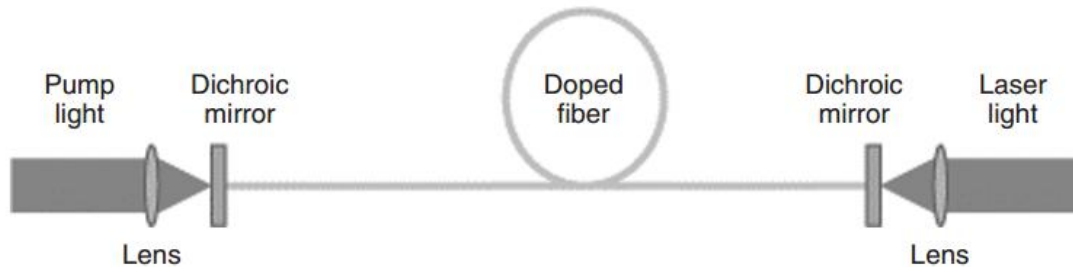


Fig. 2.2.4. Principle of fibre laser (Lackner, 2008).

When the laser beam scans the surface of a material, a portion of the beam will be reflected from the interface due to the discontinuity in the real index of refraction and some will be absorbed by the material and some transmitted into the work piece without interaction. The reflectivity of a given material will depend on the frequency (wavelength) of the light source through the dispersion relation of its index of refraction (Fig. 2.2.5). Also important to note is that only a small portion will be transmitted in metals due to their high opacities (Roberts, 2012).

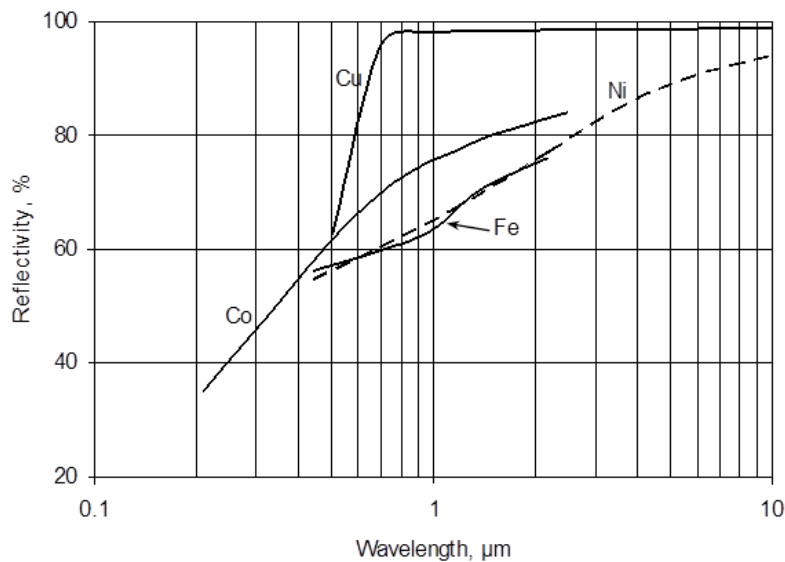


Fig. 2.2.5. Normal-incidence reflectivity of metals as function of wavelength (Gray, 1972).

Once inside the material, absorption causes the intensity of the radiation to decay with depth at a rate determined by the material's absorption coefficient A (optical penetration or absorption depth is $1/A$, Fig. 2.2.6). In general, A is a function of wavelength and

temperature, but for constant A , intensity I decays exponentially with depth z according to the Beer–Lambert law:

$$I(z) = I_0 \exp(-Az) \quad (\text{Equation 2.1})$$

Numerous factors influence the absorption capabilities of a material. Surface roughness or packing structure, play a role but the most influential according to Roberts (2012) is the wave length of the laser beam. For most metals this is one of the main reasons a Fibre laser with a shorter wave length about 1074 nm is utilised whereas a conventional CO₂ laser with a wavelength of approximately ten micron is not employed in modern metal additive systems.

In metals, optical absorption is dominated by the free electrons through such mechanisms as inverse Bremsstrahlung. Energy is subsequently transferred to the crystal lattice by photon collisions. The kinetic energy of the atoms are raised leading to elevated temperatures of the material (Brown & Arnold, 2010).

Powder particles are melted when the melting temperature of the material is reached $T_{melting}$. Molten particles create a liquid pool; temporary existence of this liquid state is defined by the laser scanning speed. The temporal and spatial evolutions of the temperature field inside a material are governed by the heat equation. The heat equation is derived from the conservation of energy and Fourier’s law of heat conduction, which states that the local heat flux is proportional to the negative of the gradient of the temperature. In a coordinate system that is fixed with the laser beam, the heat equation can be written as

$$\rho c_p \frac{\partial T}{\partial t} - \nabla[k\nabla T] = Q \quad (\text{Equation 2.2})$$

Where ρ is density, c_p is heat capacity, k is thermal conductivity, Q is heat generated per unit volume.

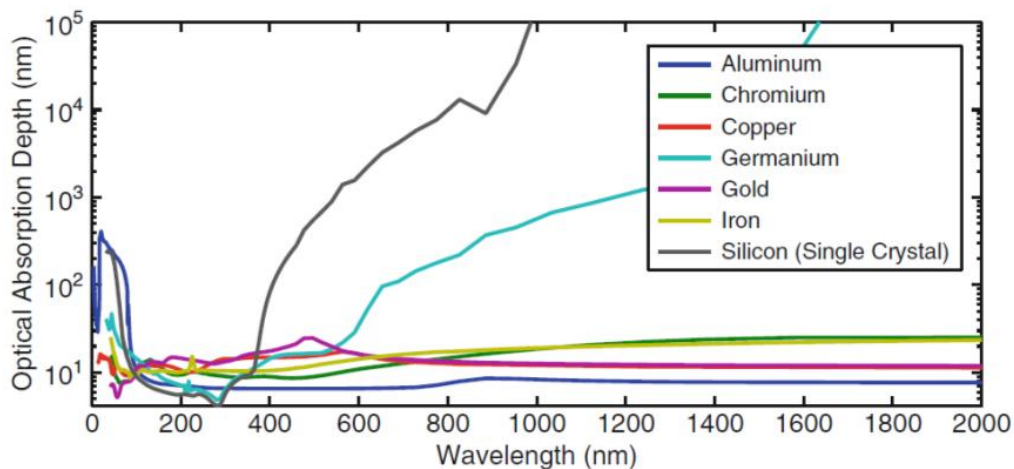


Fig. 2.2.6. Optical absorption depths for several materials over a range of wavelengths (Lide, 2001).

The solidification of the molten pool results in the formation of DMLS tracks. These tracks adjacent to each other form a layer of processed material. Multiple layers of combined tracks then form a 3D object or part.

2.2.2. Parameters Influencing DMLS

Factors influencing on the DMLS process can be divided into i) machine-based, ii) material-based and iii) process-input parameters (Fig. 2.2.7). Parameters such as, scan line spacing (hatch distance), laser beam power, scan speed, energy density, layer thickness etc. play an important role on the properties of the 3D objects produce by the DMLS.

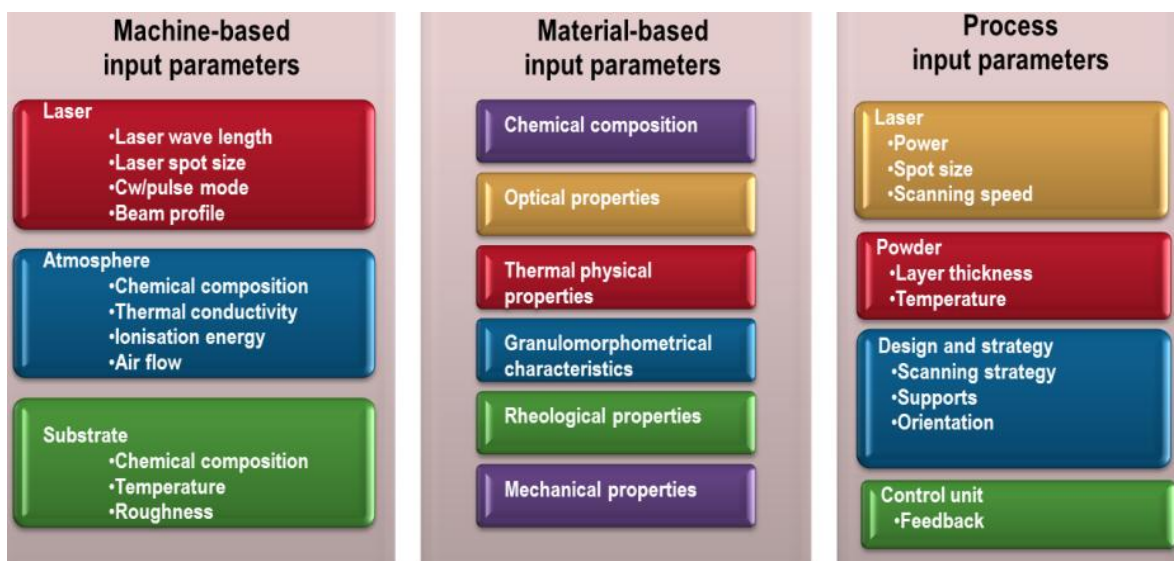


Fig. 2.2.7. Factors influencing on DMLS process (Klocke *et al.*, 2003; Yadroitsev, 2009).

2.2.3. Single Track Formation

In the track-by-track DMLS process, the laser beam melts material along a path predetermined by the software interface, this path is created in the powder particle bed (deposited layer), thereby forming a molten track (or 'vector', Fig. 2.2.8). This track can break up into a row of independent spheres (drops). The fragmentation of the tracks is a well-known drawback of DMLS referred to as the 'balling' effect. If surface diffusion controls the break-up process, a high surface tension will enhance the kinetics of the breaking up of the liquid cylinder (Yadroitsev, 2009).

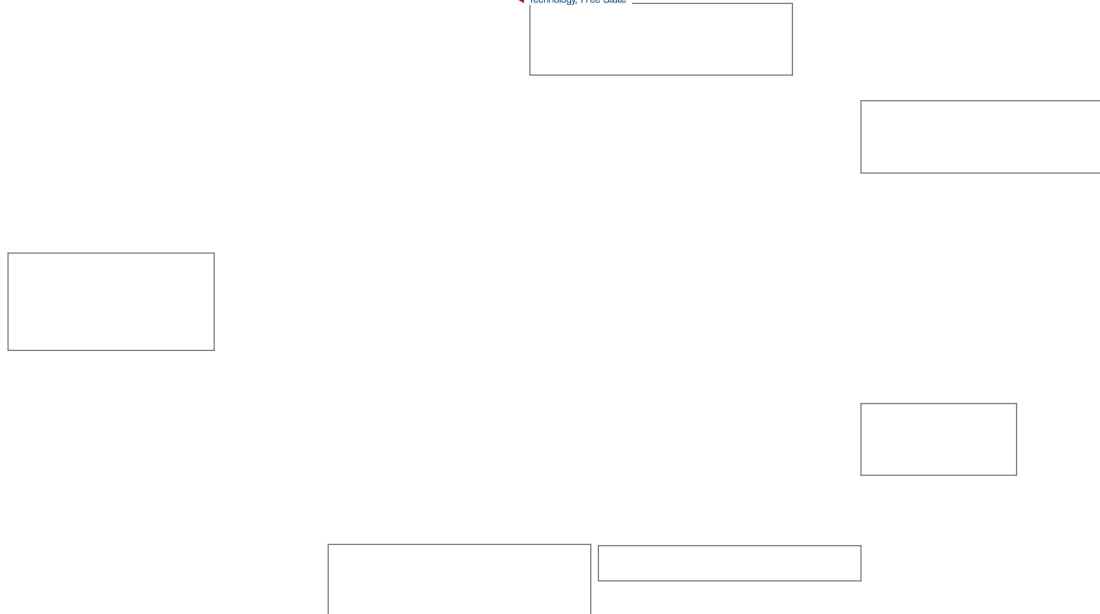


Fig. 2.2.8. Single track formation (Yadroitsev, 2009).

The ‘balling’ effect appears both at the lower and the upper bounds of the scan speed interval (Fig. 2.2.9). For higher scan speeds track failure is explained by a capillary instability of the melt pool at high length-to-width ratios when it fragments with reducing surface energy. For example, for 904L steel powder the contact zone between the remelted powder and the substrate tends to vanish at $V > 0.20$ m/s for a laser power of 50 W (Yadroitsev *et al.*, 2010) (Fig. 2.2.9). For a laser power of 25 W the substrate remelting depth is absent for all ranges of scanning speed investigated. Therefore the upper stability limit of track formation can be related to the loss of the contact between the molten powder and the substrate.

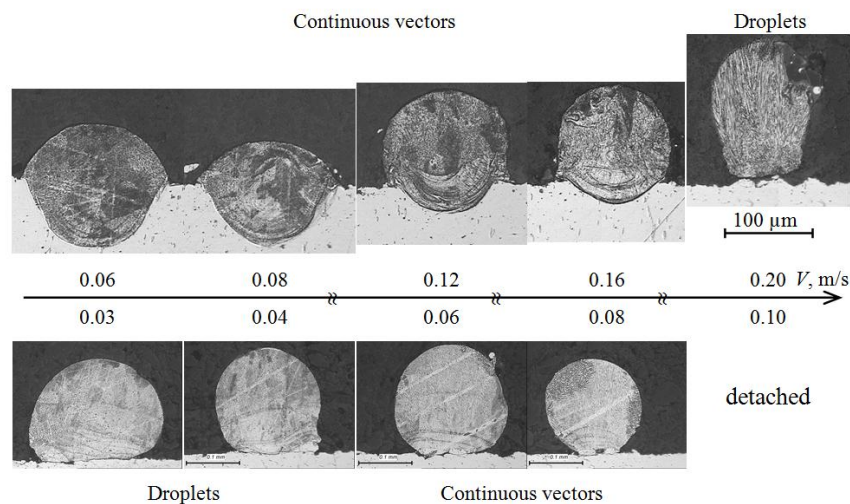


Fig. 2.2.9. Cross-sections of laser sintered tracks from SS grade 904L ($-16 \mu\text{m}$) powder. Thickness of the deposited powder layer is $50 \mu\text{m}$, effective power input per unit speed $P/V = \text{const.}$ (Yadroitsev, 2009).

Fig. 2.2.8 shows that not only the powder in the irradiation zone is involved but also powder from the surrounding areas. The denudation zone can be twice the width of the single

track formed (Yadroitsev *et al.*, 2010). Finally, geometrical characteristics of the single track (Fig. 2.2.10) define scanning and building strategies of 3D DMLS objects.

Metal sul

Fig. 2.2.10. Cross section of a single track with metal powder on a steel substrate (Yadroitsev *et al.*, 2010).

Stable tracks are the basis for producing non-porous objects with reliable properties, thus optimal process-parameters have to be used to produce continuous tracks with stable geometry. A DMLS object consists of a set of individual single layers and tracks (Fig. 2.2.11). The primary units for DMLS are single tracks; their combination creates a single layer, and from the sequence of layers, a 3D object is sintered.

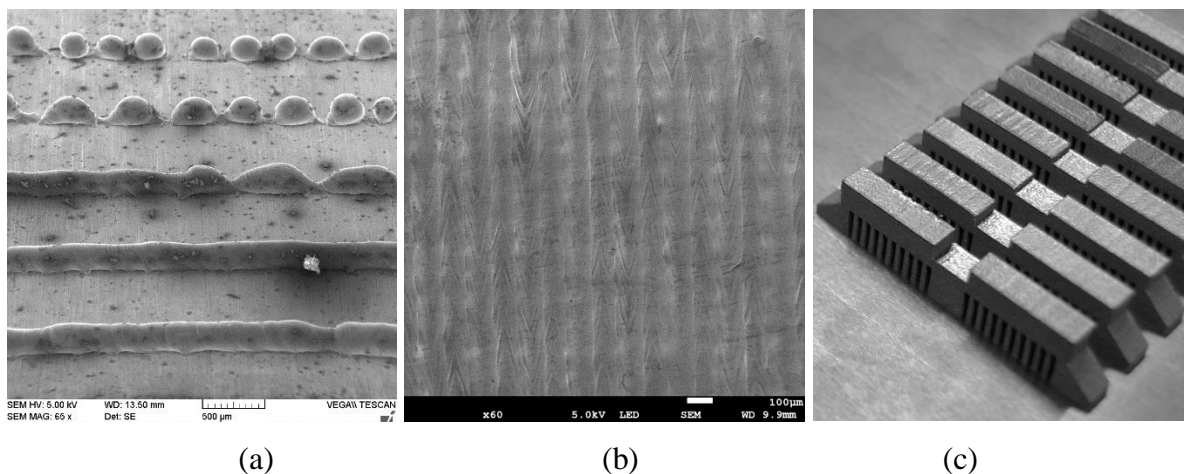


Fig 2.2.11. Single tracks at the substrate (a); single layer (b) and 3D DMLS objects (c).

To produce fully dense objects from the employed powder material, optimal process parameters and a specific strategy of manufacturing should be used. There were a number of attempts to formulate key principles and strategies to fabricate high-quality porous-free objects. Several publications have been focused on the selection of optimal parameters to fabricate single tracks from metal powders. The process parameters have been statistically analyzed for 316L stainless steel (Yadroitsev, 2009), 17-PH steel, (Matilainen *et. al*, 2014),

904L stainless steel, CuNi, CoCr, Inconel 625, H13 tool steel, Ti6Al4V alloy, (Yadroitsev *et al.*, 2009; Mohanty *et al.*, 2014), and it has been demonstrated that laser power, scanning speed and powder layer thickness are the most important process parameters in DMLS.

These studies confirmed the statement that the same energy input (P/V) at different laser power leads to the formation of different patterns of the single tracks. For the formation of stable continuous single tracks from metal powder which have a metallurgical bond with the substrate, the hierarchy of the process parameters ranges in order of importance: laser power density, powder layer thickness, scanning speed and powder particle size (Yadroitsev *et al.*, 2012).

The depth of the penetration into the substrate/previous layer is an important characteristic of track formation and structure. Remelted depth of the single track determines the metallurgical bond with the substrate or previous layer. The metallurgical bonding between the solidified layers is of course a critical issue as this generates a solid platform for the part to be successfully built up. Complete remelting of the powder in the scanning zone and its adhesion to the substrate/previous layer are crucial in obtaining non-porous DMLS parts (Gusarov *et al.*, 2007). Scanning and building strategies determine the mechanical properties of the DMLS parts (Yadroitsev, 2009).

The process parameters employed by DMLS directly influence the single track formation of the material. The single track formation is the first step in forming the final part. When the optimum process parameters are employed, the single tracks are continuous and its metallurgical bond with the substrate (whether physical substrate or previously melted layer) is consistent.

2.2.4. Single Layer Formation

Single layer is a superposition of the synthesized single tracks. Surface morphology of single layers depends on geometrical characteristics of single tracks, scanning strategy and hatch distance, which shifts between tracks in the plane of the laser beam scanning. Non-uniform thickness of the next deposited powder layer could be critical because defective porous structure will be produced. Morphology of single layers after scanning is complex. If the hatch distance is more than a single track width, powder is melted in a sequence of individual tracks (Fig. 2.2.12). Non-optimal hatch distance can result in formation of gaps between tracks in a single layer, which causes chains of pores in the final DMLS object (Yadroitsev *et al.*, 2015).

The influence of the hatch spacing on layer morphology is demonstrated in Fig. 2.2.12. The variation of the hatch spacing from 60, 120 and 240 μm shows that when hatch spacing increases more of the powder is not sintered. At 240 μm hatch distance shows that a lot of powder is not sintered (Yadroitsev, 2009). Thus choosing of hatch distance must be optimal to avoid pore formation in 3D objects. Optimal parameters will consequently lead to homogenous layers with constant thickness and bonding between tracks. From the aforementioned it is clear that DMLS is a parameter sensitive process. Another important thing is powder layer thickness. DMLS thin walls had specific surface morphology and it is sensitive to powder layer thickness (Fig. 2.2.13).

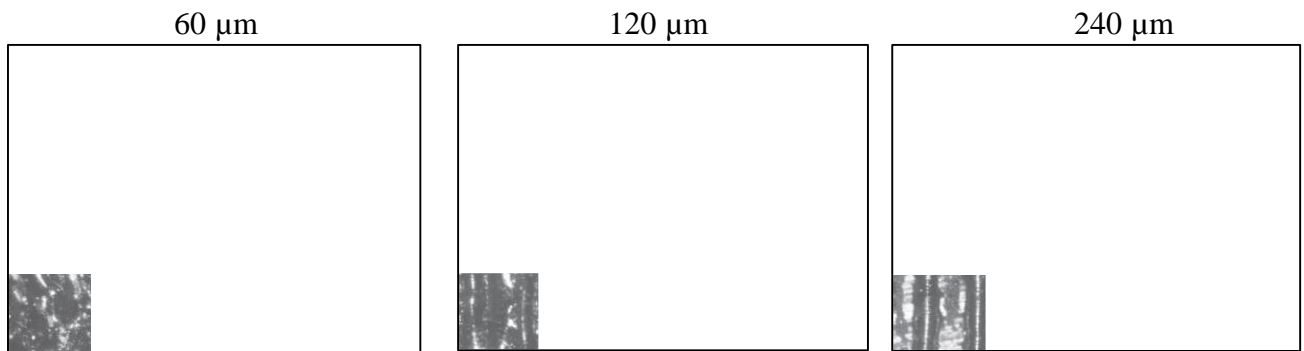


Fig. 2.2.12. Surfaces of the first layer from SS grade 904L powder obtained at different hatch distances. Powder layer is 50 μm thickness, laser power is 50 W, and scanning speed is 0.14 m/s (Yadroitsev, 2009).

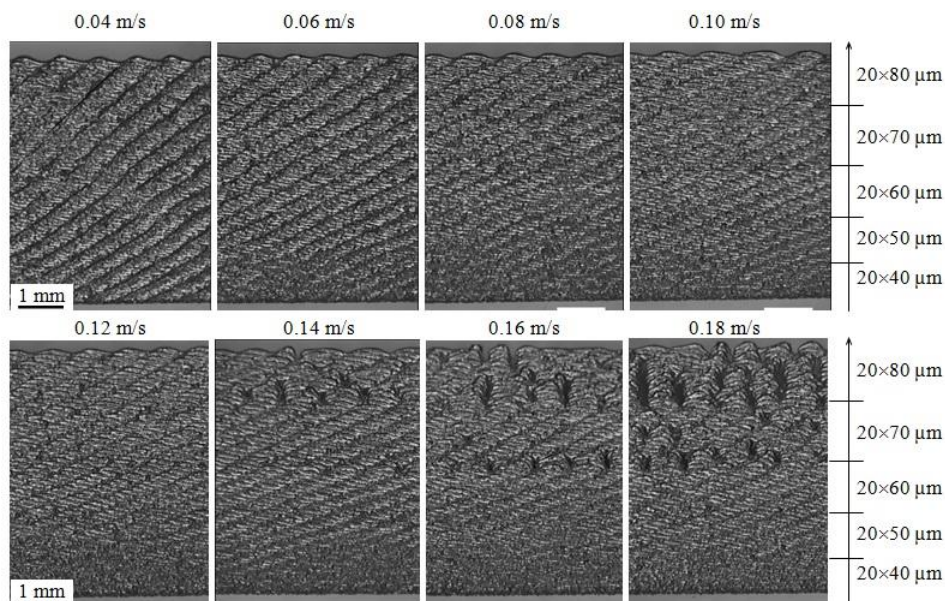


Fig. 2.2.13. Laser sintered thin walls from SS grade 316L powder. Thickness of powder layers varied from 40 to 80 μm with a step of 10 μm , 20 layers for each thickness, $V=0.04\text{--}0.18$ m/s, $P=50$ W (Yadroitsev, 2009).

Hatch patterns, or scanning strategy (Fig. 2.2.14), are the patterns formed by the tracks of each layer. Hatch distance is the distance between adjacent scan line centers.

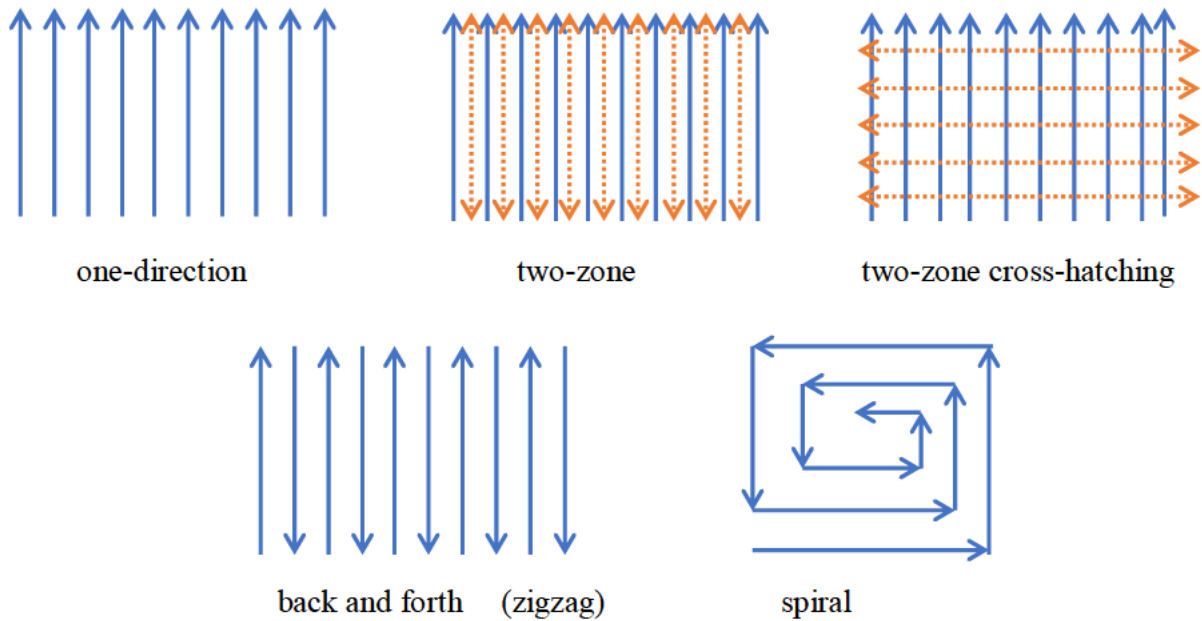


Fig. 2.2.14. Different scanning strategies (patterns) of a single layer.

The hatch distance is of critical importance to ensure a good metallurgical bond between tracks (Fig. 2.2.15). At a two-zone strategy, each layer is processed twice with the laser: first, the laser beam melts the powder layer with a certain hatch distance and then subsequently the laser beam passes in between sintered tracks and re-melts each two neighboring tracks. Rescanning, or a two-zone strategy, also significantly improves the surface quality of single layers; it leads to the disappearance of droplets and reduction of the roughness of the manufactured layer (Yadroitsev, 2009).



Fig. 2.2.15. Top view of single layer produced by one-zone (a) and two-zone strategy (b) of laser scanning.

$P = 50 \text{ W}$; $h = 50 \text{ }\mu\text{m}$; $V = 0.12 \text{ m/s}$; $s = 120 \text{ }\mu\text{m}$ (Yadroitsev *et al.*, 2015).

Patterns can be the same throughout multiple layers, either in x or y directions, the scanning direction can also be rotated from layer to layer (Fig. 2.2.16). As previously the hatch distance is one of the defining parameters to ensure fully dense parts, if the hatch distance is too large, porosity will increase and weaken the final mechanical and structural properties of the part, whereas a hatch distance which is too small will increase production time and cost.

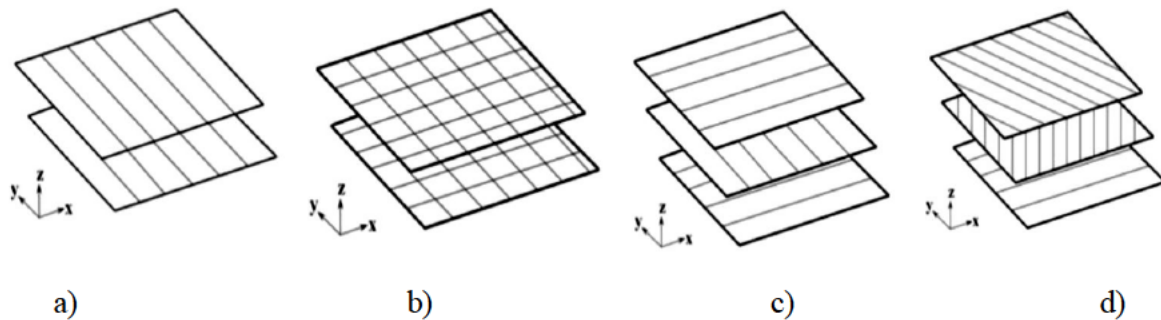


Fig. 2.2.16. Different scan patterns for consistent layers: a) one direction b) double scanning each layer c) alternating scanning d) the direction of scanning rotated of certain angle between consecutive layers (Manfredi *et al.*, 2014).

There exist also other scanning strategies, and mostly the strategies vary from different AM manufacturers. For example, Concept Laser uses an “*island principle*” scanning strategy (Fig. 2.2.17) these islands differ in size from 1 mm×1 mm up to 10 mm×10 mm; these individual squares are not necessarily scanned coincident with each other but rather stochastically (Concept Laser, 2015). These squares then form an entire pattern across the produced layer.

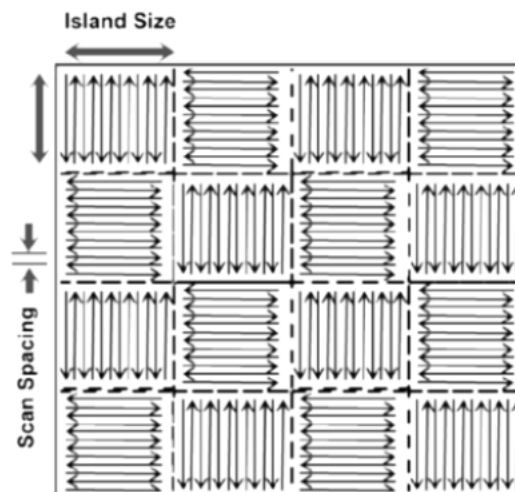


Fig. 2.2.17. Schematic of the island scan strategy (Qiu *et al.*, 2013)

Another strategy known as the band/strip strategy is utilized by EOS (Fig. 2.2.18), this is a back and forth scanning strategy. The bands are about 5 mm in width and extending across the entire layer, contouring is done before the bands are produced, afterwards post contouring is done. Contouring is where the laser scans the perimeter of the object, forming a distinct shape in the powder bed layer.

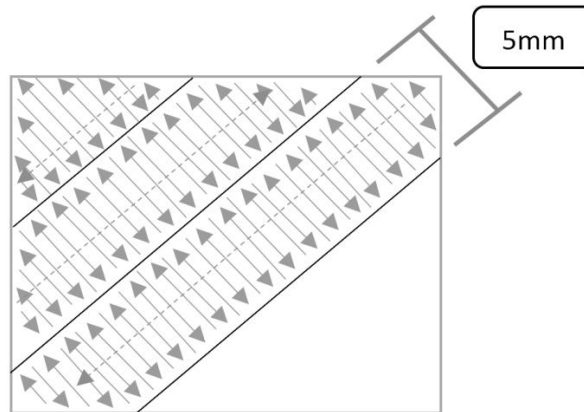


Fig. 2.2.18. Schematic showing the band/strip strategy.

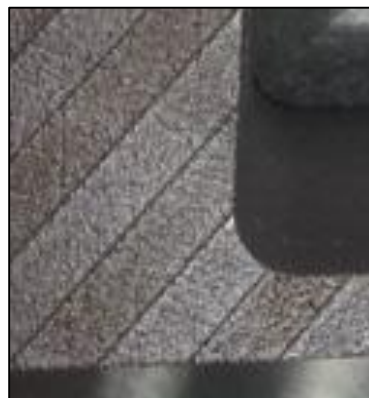


Fig. 2.2.19. Top view of EOSINT M280 Band/Strip scanning strategy.

One-layer scanning strategies, scan patterns for consistent layers, contouring and building direction define the properties of DMLS 3D objects.

2.2.5. 3D DMLS Object Density

Laser power has a direct influence on the characteristics of how the molten pool forms when the powder changes to a liquid state. Meier & Haberland (2008) postulated that as laser power increased from 30 to 90 W with all other parameters remaining constant it had an increasing influence on part density. A decrease in power leads to greater porosity within created parts as shown in Fig. 2.2.20. It has been suggested that an increase in laser power

shows better interlayer penetration and higher power input created a more homogenous melt pool, allowing sufficient heat energy for the material to fuse.

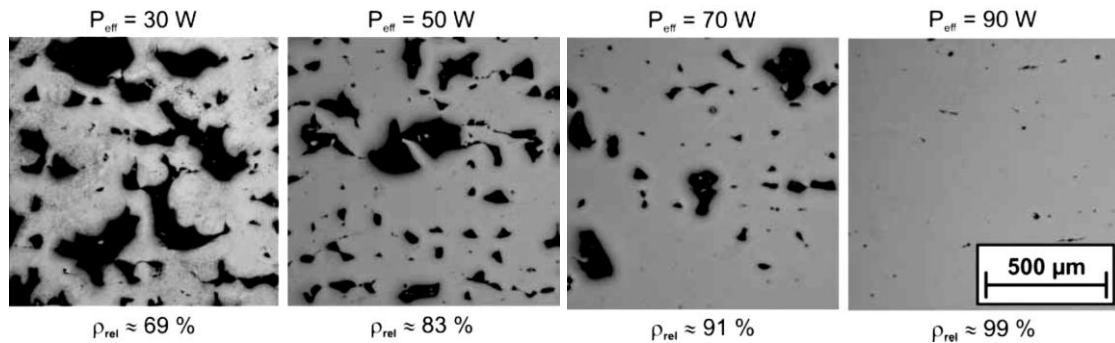


Fig. 2.2.20. Difference in density at different laser power for al 316L Stainless Steel (Meier & Haberland, 2008).

However, excessively high laser power density causes keyholes at low scanning speeds or instability of long shallow molten pools at high scanning speeds (Yadroitsev et al, 2010; Thjis *et al.*, 2013). A number of publications were dedicated to the analysis of laser scanning strategies and related defects in 3D objects (Yasa *et al.*, 2011; Sun *et al.*, 2013; Wang *et al.*, 2013; Casalino *et al.*, 2015). It has been shown that different scanning strategies resulted in different defects and caused anisotropy of mechanical properties of DMLS samples.

When manufacturing complex shaped objects with overhanging elements, the geometrical characteristics of its tracks depend on local geometry of the DMLS object (Wang *et al.*, 2013; Llin *et al.*, 2014). Specific scanning strategies and process parameters can be used for different sections of such complicated objects. Final porosity has also been discussed and correlated to process parameters in Ti6Al4V (Sun *et al.*, 2013), 18Ni Maraging 300 steel (Casalino *et al.*, 2015) and AlSi10Mg (Thjis *et al.*, 2013) alloys. It was suggested that porosity is related to the energy input into powder layer and scanning strategy.

“To produce continuous and stable single tracks, optimum laser power, laser spot size and scanning speed for different powder layer thicknesses must be used. Initial powder layer thickness could be chosen in respect to the particle size of the employed powder. The geometric characteristics of the tracks affect the choice of subsequent scanning strategies and hatch distances. Choosing a scanning strategy defines the layer’s morphology which in turn affects the subsequent layer thickness, regularity and continuity. The high quality of the synthesized single layer should guarantee that the thickness of the next deposited powder layer does not vary greatly preventing further irregularity and balling effect. Thus, the feedback is established between energy input parameters and selected layer thickness for powders with a specific particle size distribution ” (Yadroitsev *et al.*, 2015).

The aforementioned strongly indicates that process parameters of DMLS is critical for the production of successful 3D objects with suitable properties for different materials and application, a schematic of the selection process is shown in Fig. 2.2.21 and illustrates the necessary areas of focus when evaluating or developing a set of parameters for successful manufacturing of 3D objects by DMLS for different materials.

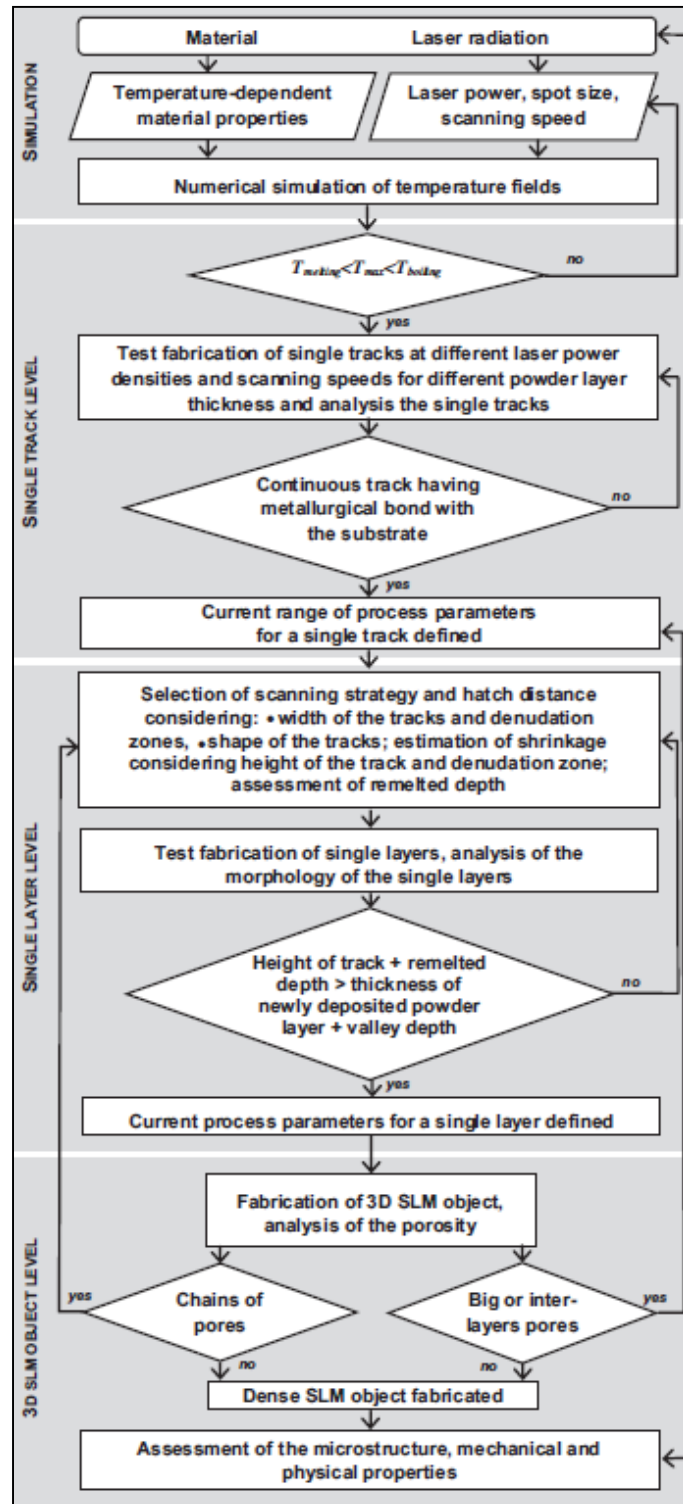


Fig. 2.2.21. Algorithm for optimal DMLS process parameters (Yadroitsev *et al.*, 2015).

2.2.6. 3D Functional Components

Developing and implementing DMLS might be complex but the advantageous of the direct-to-part path, places new avenues of innovations in the hands of designers, engineers as well as medical personnel. Fig. 2.2.22 shows a custom lower jaw section created with pores and a ‘cage’ concept allowing for osseointegration of harvested bone. This implant is patient specific, facial features of the patient will be symmetrical and the social acceptability and quality of life for this patient will be regained (as the lower section had to be removed due to a tumour).

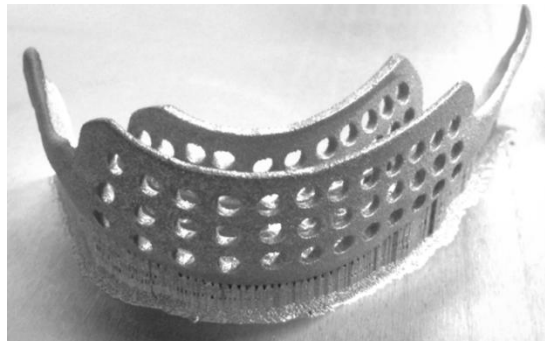


Fig. 2.2.22. Caged lower jaw section developed patient specifically at CRPM from Ti6Al4V via DMLS.

These solutions are now available because of DMLS and AM, arguably this technology is directly and indirectly impacting lives, whether by medical application or by more efficient ‘greener’ part generation. Fig. 2.2.23 shows the successful implantation of a maxilla-facial component. This patient suffered from cancer in the jaw bone, the affected area was removed, and replaced via a Ti6Al4V patient specific implant manufactured by DMLS.



Fig. 2.2.23. X-ray photo of DMLS Ti6Al4V jawbone (CRPM, 2015).

2.2.7. Summary

An overview of DMLS technology is given in this section; the importance of the laser beam-powder-substrate interaction, as well as prominent process parameters are outlined for the DMLS process, with the critical components of track and layer formation mentioned and discussed in-depth. The aforementioned shows how much the parameters of the process can impact production as well as material properties. The capabilities of DMLS are also overviewed, and finally a practical medical solution is demonstrated as a prominent market component of DMLS and its capabilities.

2.3. Residual Stress

Residual (locked-in) stresses in a material or component are those stresses that exist in the object without and usually prior to the application of any service or other external loads. Manufacturing processes are the most common causes of residual stress. Virtually all manufacturing and fabricating processes – casting, welding, machining, moulding, heat treatment, etc. – introduce residual stresses into the manufactured object. In practice no component is entirely free of residual stress introduced during processing (Withers & Bhadeshia, 2001).

Another common cause of residual stress is in-service repair or modification. Also stress may be induced later in the life of the part by installation or assembly procedures, by occasional overloads, by ground settlement effects on underground structures, or by dead loads which may ultimately become an integral part of the structure. The effects of residual stress may be either beneficial or detrimental, depending upon the magnitude, sign and distribution of the stress with respect to the load induced stresses (Vishay Measurements, 1993).

In other words then, residual stresses are those stresses locked into a body when it has obtained equilibrium, these stresses are in a balance, with no external influences applied. Unlike stress caused by external loading, which can be calculated accurately using appropriate formulae, residual stresses are less predictable (Residual, 2015) .

2.3.1. Types of Residual Stress

Residual stress is categorized differently depending on its nature. Macro-stress such as caused by non-uniform plastic deformation of any part etc. is seen as a type I stress, because these stresses vary continuously across a vast area or region. Type II stresses differ

from type I stresses, as they extend over the grain scale, it is also known as intergranular stresses. Type III is in contrast to type II in that it acts over an atomic scale (Withers & Bhadeshia, 2001). Residual stress can then be categorized in relation over the length in which they equilibrate. Macro-stresses (type I) equilibrate over large distances or dimensions (size of the part or structure). Intergranular stresses (type II) equilibrate over an amount relating to the grain dimensions (usually 3-10 times that of the grain size). Type III stresses equilibrate over a much smaller area or length than a single grain size (Fig. 2.3.1).

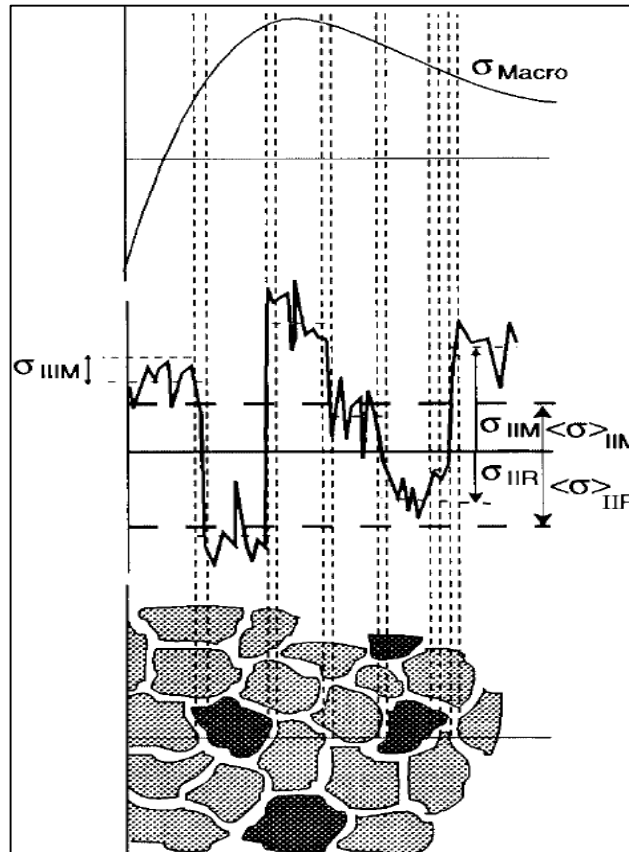


Fig. 2.3.1. Residual stress categorised according to characteristic length scales (Withers & Bhadeshia, 2001).

2.3.2. Origin of Residual Stress and its Effect on the Performance of Materials

Depending on the type of residual stress, the root cause may vary vastly (Fig. 2.3.2). Knowing the origin of residual stress helps the designer and or manufacturer to prevent or accommodate the effects of this occurrence within the specific process. This will play a significant role in preventing failure during processing of components.

Macro-stresses in general may be introduced due to the following processes or occurrences (usually employed during manufacturing); non-uniform plastic flow due to outside influences (shot-peening, hammer-peening etc.); non-uniform plastic deformation due to heating or cooling (heat treatment in general); plastic deformation due to structural

changing (milling, lathe-work, bending); different surface treatments (plating, enamelling, coatings, hardening); differing thermal expansion coefficients and mechanical mismatching of varying components of composites (multiphase materials, ceramic coatings) (Totten *et al.*, 2002).

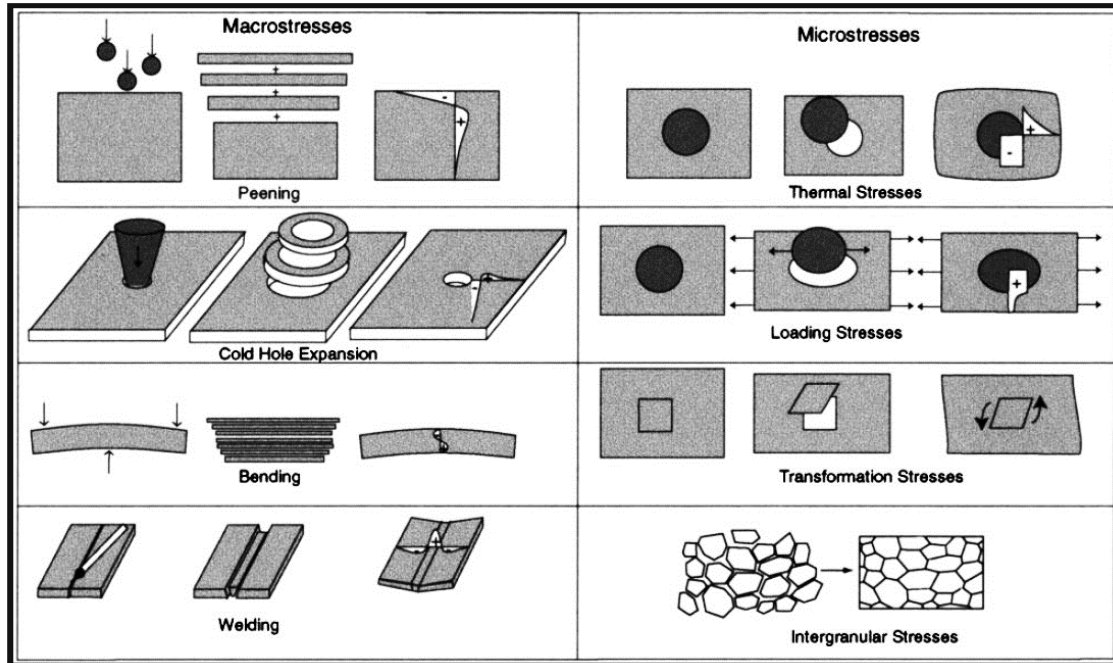


Fig. 2.3.2. Residual stresses arise from misfits (eigen strains) either between different regions or between different phases within material: different types of residual macro and micro residual stress are illustrated (Withers & Bhadeshia, 2001).

Micro-stresses (Type II) though low almost always exist in polycrystalline materials because of different elastic and thermal properties of differently orientated neighbouring grains. Notable micro-stresses are also observed when phase transformation has taken place in a multiphase material. When the lattice parameters of two phases are slightly different, the lattice parameters that do not match create a forced coherence within the matrix of the multiphase material with coherency strains placed at the interfaces. The type III category typically includes stresses due to coherency at interfaces and dislocation stress fields (Withers & Bhadeshia, 2001).

There are a number of factors that could cause residual stress of which the manufacturing process (Fig. 2.3.3 and Table 2.3.1) is the most prominent, for example, casting, welding, machining or DMLS (Residual, 2015). The aforementioned factors fall under three main categories, mechanical, thermal and structural, where mechanical stresses are induced during plastic deformation, thermal stresses is caused by thermal gradients

experienced by the material (non-uniform heating or cooling) and phase change represents a crystal structure change (Styger *et al.*, 2014; Residual, 2015; Proto, 2015).

Residual stresses usually develop during most processes which intend to change either the geometric shape (Withers & Bhadeshia, 2001) or the properties of the material. Residual stress within a material could be advantageous in some instances, for example tempered glass (compressive surface stress) but in many instances in the metal industry as mentioned before it may be undesirable or even detrimental.

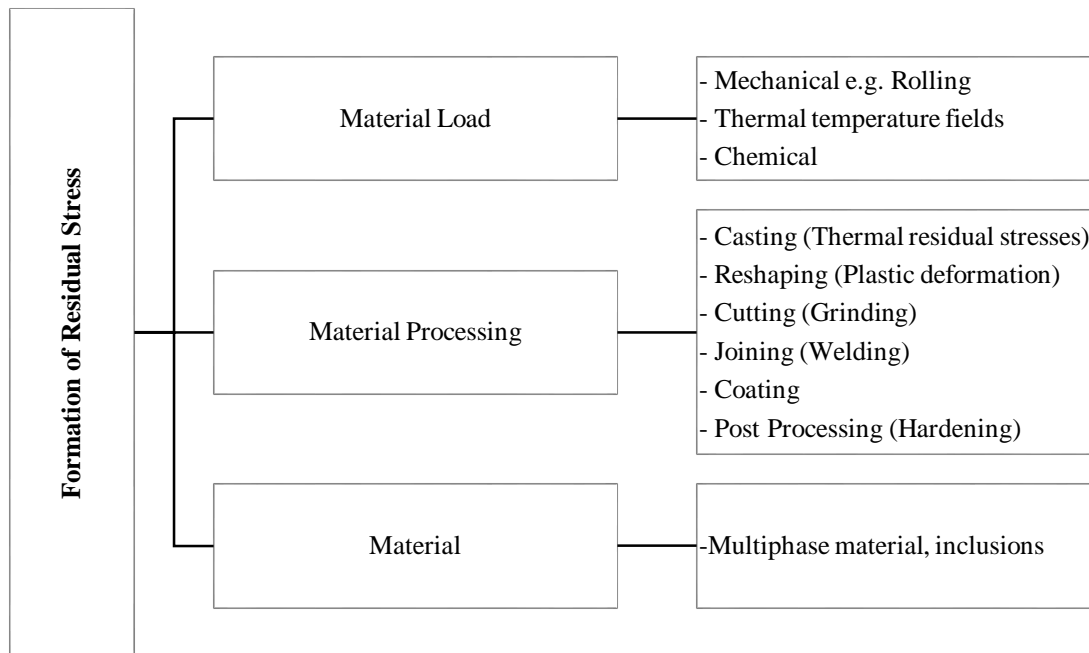


Fig. 2.3.3. Origin of residual-stress formation (Hauk, 1977).

Table 2.3.1. Origin and cause of Residual stress during manufacturing (Totten *et al.*, 2002)

Process	Mechanical	Thermal	Structural
Casting	No	Temperature gradient during cooling	Phase transformation
Shot peening, hammer peening, roller burnishing, laser shock treatment, bending, rolling, chasing, forging, straightening, extrusion	Heterogeneous plastic deformation between the core and surface of the part	No	Depends on the material
Grinding, turning, milling, drilling, boring	Plastic deformation due to the removal of chips	Temperature gradient due to heating during machining	Phase transformation during machining if the temperature is sufficiently high
Quenching without a phase transformation	No	Temperature gradient	No
Surface quenching with a phase change (induction, EB, laser, plasma, classical methods)	No	Temperature gradient	Change of volume due to a phase change
Case hardening, nitriding	No	Thermal incompatibility	New chemical component with volume modification

Process	Mechanical	Thermal	Structural
Welding	Shrinkage	Temperature gradient	Microstructural change (HAZ)
Brazing	Mechanical incompatibility	Thermal incompatibility	New phase at interface
Electroplating	Mechanical incompatibility	Mechanical incompatibility	Composition of plating depending on bath used
Thermal spraying (plasma, laser, HVOF)	Mechanical incompatibility, micro-cracking	Thermal incompatibility, temperature gradient	Change of phase in plating
PVD, CVD	Mechanical incompatibility	Mechanical incompatibility	Change of phase
Composite	Mechanical incompatibility	Mechanical incompatibility	No

In Fig. 2.3.4 properties of materials that are influenced by residual stress are shown. The influence on yield and tensile strength by residual stress is obvious, if a tensile residual stress exists in the component if a tensile force is then applied the yielding of the component will take place way below its proposed (unstressed) yield strength demonstrated by Eq. 2.3

$$\sigma_L + \sigma_R = \sigma_C \quad (\text{Equation 2.3})$$

σ_L – loading stress (tensile), σ_R – residual stress (tensile), σ_C – critical stress actually experience by component.

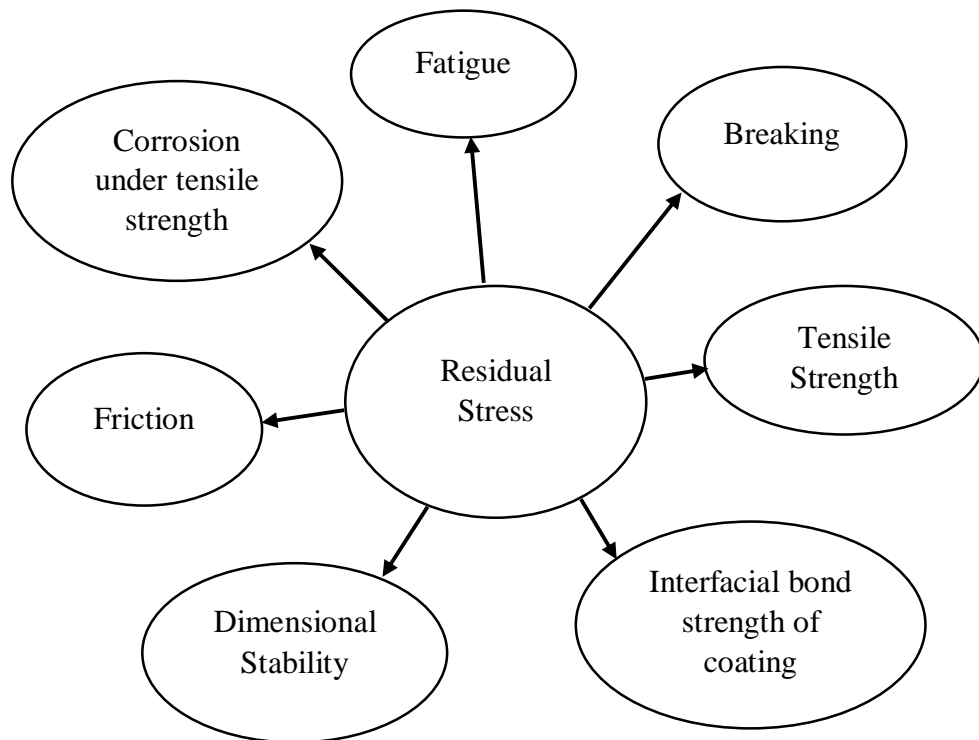


Fig. 2.3.4. Effect of residual stress on the performance of materials (Totten *et al.*, 2002).

This logic could also be applied to fatigue strength, depending on the compressive or tensile nature of the residual stress the component life can be increased, or drastically decreased especially when there is not an awareness of the residual stress present. This is especially important with high cyclic loads such as in aircraft component application (Totten *et al.*, 2002). Tensile residual stresses are generally harmful or undesirable, especially for parts that are under cyclic loading.

The geometric changes in parts due to residual stress is also clear especially in the welding industries even in the laser-cutting industries, the rapid thermal changes induce residual stress and the parts geometries change or warp so that it is unfit for application (Meada *et al.* 2014). As indicated James *et al.* (2011), for welding the magnitude of tensile residual stress depends on weld process (solid state or fusion) and the ratio of thermal strain during cooling to the yield strain in the material. For example, “ *in titanium and aluminium welds residual stress magnitudes may be less than 1/2 of the yield strength, while in friction stir welding peak tensile residual stresses may be less than 1/4 of the yield strength. Stresses parallel with the weld run generally have higher magnitudes than transverse or short transverse stresses* ”. This clearly illustrates that different processes have different impacts on the material properties. Corrosion is also another adverse consequence of residual stress as well as friction but will not be elaborated on in this work.

The residual stress within a component is either tensile or compressive, usually when there exists a compressive residual stress this prevents crack growth near the surface, i.e. tempered glass (Colegrove *et al.*, 2013). The advantages of the residual stress caused by shot peening in a workpiece are shown in Fig. 2.3.5. Tensile stresses are then in the same instance more detrimental, although the stress and its effect on the parts performance relies on the application of the specific component.

From the effects previously mentioned it is clear that for any medical or aerospace application there must be a thorough knowledge on the proposed components residual stress levels to determine safe application and longevity.

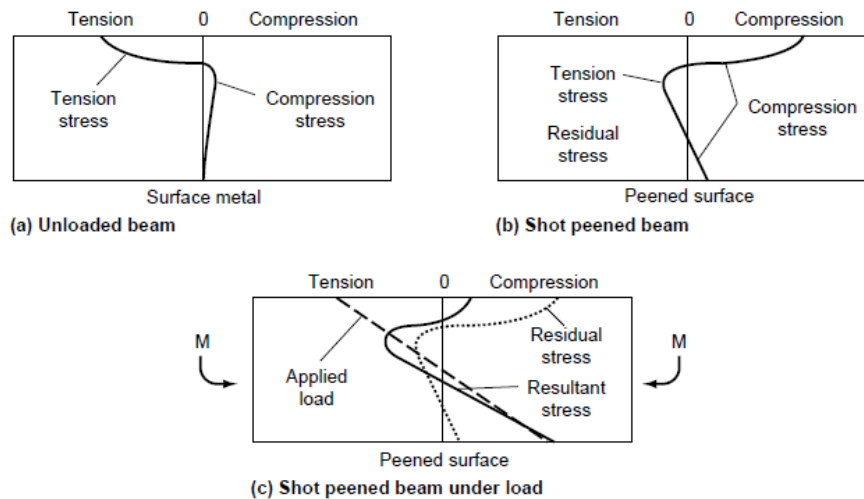


Fig. 2.3.5. Comparison of stress distributions. (a) Typical stress distribution in surface of metal beam, unloaded by exhibiting residual tensile stress from normal fabricating procedures. (b) Same beam after shot peening, still without external load. Surface stress is now compressive. (c) Beam, when subjected to design loading, still shows some residual compressive stress at surface (Totten *et al.*, 2002).

2.3.3. Definitions of the Stresses

Normal or *direct* stress is defined as the stress acting normal to a surface or plane; the plane on which these stresses are acting is commonly categorised as XY , YZ , ZX in common 3 dimensional coordinate system. For example as shown in Fig. 2.3.6, stresses acting normal to the faces of a basic cube are identified by their specific subscripts, it also shows in which direction the stress acts, so σ_x is the direct stress acting in the x direction. Since σ_x is a normal stress it must act on the plane perpendicular to the x direction. Tensile stresses are denoted as positive and compressive stresses as negative, according to convention (Fitzpatrick *et al.*, 2005).

Shear stress acts perpendicular to the normal stress. Two subscripts are used to define the shear stress, the first denotes the plane in which the shear stress is acting and the second denotes the direction of the shear stress. For example, τ_{zx} is the shear stress on the plane perpendicular to the z -axis in the direction of the x -axis. The sign convention follows Timoshenko's notation Fig. 2.3.7. A shear stress is positive if it acts in the positive direction on the positive face of a unit cube, and negative in the direction of the opposed face. Shear stresses are either negative or positive (Fig. 2.3.7) the nature of the normal stress does not influence the sign convention (Fitzpatrick *et al.*, 2005).

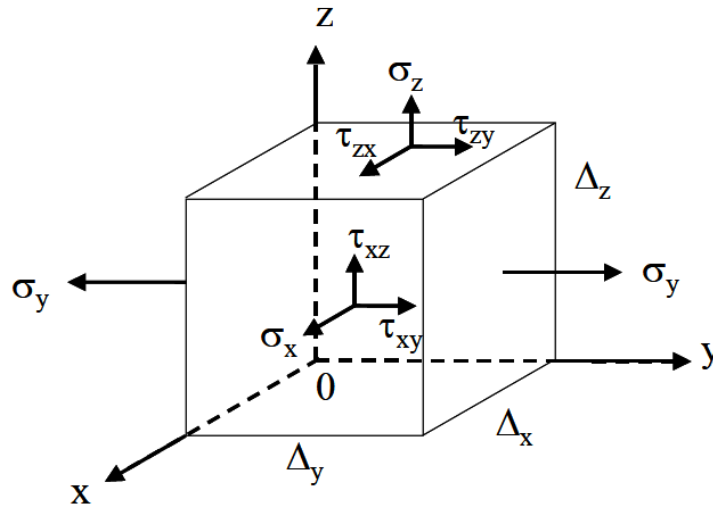


Fig. 2.3.6. Stresses acting on an elemental unit cube (Fitzpatrick *et al.*, 2005).

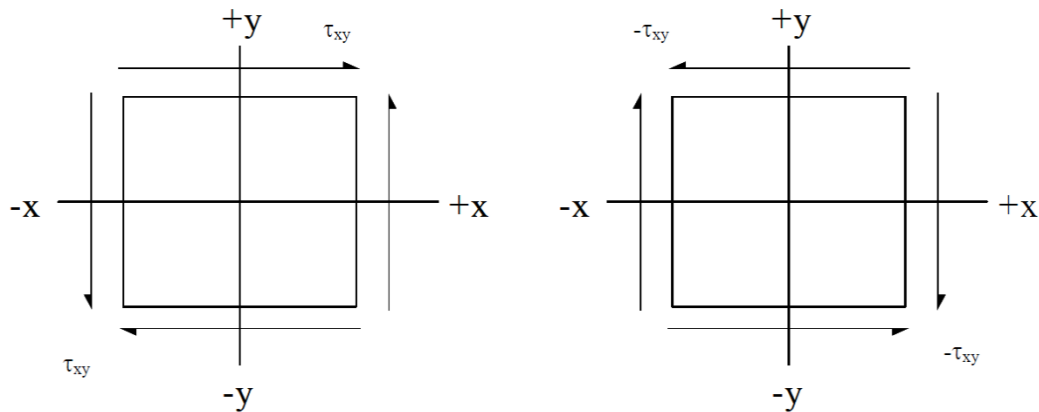


Fig. 2.3.7. Sign convention for shear stress - (a) Positive, (b) negative (Fitzpatrick *et al.*, 2005).

For any object under the influence of stress, there exists a coordinate system that has its axis perpendicular to the respective planes wherein no shear stress is present; these planes are known as principal planes. The stresses acting normal to the aforementioned planes are known as principal stresses. With regard to a two-dimensional plane stress, there exists two principal stresses denoted as σ_1 and σ_2 exist normal to each other. The direction in which these stresses act are known as the principal axes. The principal stress system supplies an effective manner of describing the stress state at a point (Fitzpatrick *et al.*, 2005).

2.3.4. Residual Stress Measurements

Knowing the magnitude of stress present within a component of any material is critical due to the failure it may impose on the components performance. Unlike stress caused by external loading which can be calculated accurately using appropriate formulae, residual stresses are less predictable (Residual, 2015). To have an understanding of the magnitude of

residual stress present will help predict and prevent failure and or performance of components. Residual stress is three dimensional, therefore adequate measurement is a priority but in the same instance also inherently complicated. Measurement of residual stress can be either done by destructive or non-destructive methods. There are numerous methods of measuring depending on the type of residual stress being measured herewith follows a few of the most common methods with a brief description.

There are numerous methods of measuring of the residual stress:

- Non-destructive (such as ultrasonic method, magnetoelastic method, X-ray diffraction method, neutron diffraction method);
- Semi-destructive (hole-drilling technique, deep-hole method, ring-core method) and
- Destructive (sectioning technique, contour method).

Ultrasonics, in the same way that light may be diffracted through a stressed transparent object, so an ultrasonic sound wave also experience interference when traveling through a stressed component (Hauk, 1977). The change in the speed of the wave is observed in the material, the change of speed indicates the average stress along the path of the wave. There are different variants of this basic method in practice today (Withers & Bhadeshia, 2001).

Magnetic Methods, with magnetostrictive materials the residual stress will cause changes in the magnetic field orientation wherever it is present in the component, this method takes advantage of this phenomena, These reorientations are observed as pulses somewhat random in amplitude, duration, and temporal separation and therefore are roughly described as noise (Hauk, 2001; Whithers & Bhadeshia, 2001).

X-Ray Diffraction (XRD). Metals are composed of atoms arranged in a specific three dimensional position known as a crystal structure, the type of crystal structure is dependent on the type of elements involved, common crystal structures are FCC, (Face Centered Cubic) BCC, (Body Centered Cubic) and HCP (Hexagonal Close Packed) Fig. 2.3.8. The mentioned crystal structures form colonies or grains that are randomly orientated but held together by intermolecular attraction, forming a bulk material. The slip system of HCP materials is displayed in Fig. 2.3.9. The slip of an HCP crystal structure is the direction or orientation system in which strains would develop at high temperatures.

Common metallic crystal structures

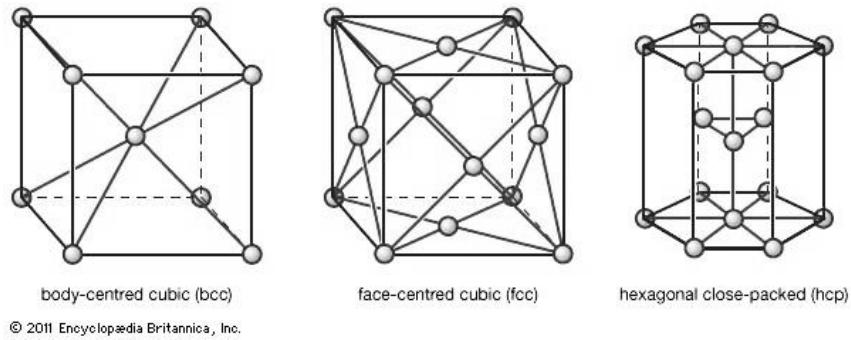


Fig. 2.3.8. Showing the different crystal structures of metals (Britannica, 2015).

The X-ray Diffraction (XRD) method takes advantage of the natural occurrence that when a metal or alloy is subjected to stress (Load or Residual) the elastic strains cause the atomic planes within the crystal lattice structure to change their spacing d . XRD measures the inter-atomic spacing which is a result of the material being subjected to strain, then using Bragg's law the stress can be determined (Fitzpatrick *et al.*, 2005).

Bragg's law was derived by W.H. Bragg and W.L. Bragg in 1912/1913 analysing some experiments produced by von Laue (a German physicist) where he placed a copper-sulphate crystal in the path of an X-ray beam. Diffracted beams were captured as spots on a photographic plate. W.H. Bragg and his son deduced an expression to explain the constructive manner in which the diffraction occurred (Fitzpatrick *et al.*, 2005).

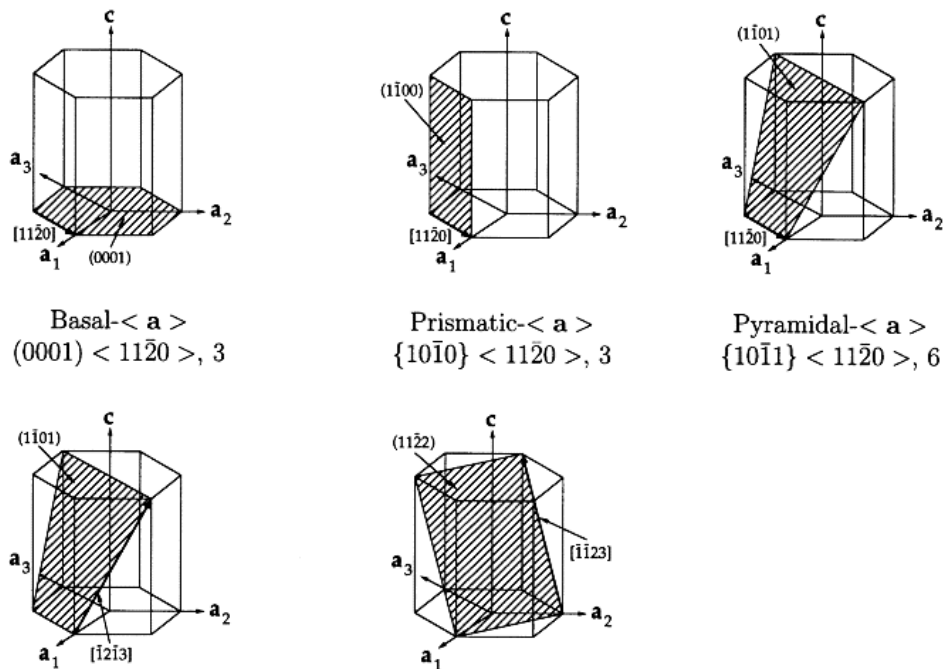


Fig. 2.3.9. Basal-a, prismatic-a, pyramidal-a slip systems, and first- and second-order pyramidal c+a slip systems in HCP materials (Balasubramanian & Anand, 2002).

The crystal structure of a metallic material is composed of planes of atoms arranged at a specific spacing (d) when X-ray beams are diffracted by these atomic planes it causes either constructive or destructive interference, when constructive interference takes place there will be a greater intensity recorded (using photographic plate). This constructive interference takes place when the waves of X-rays are in phase (Pervey, 2015).

The angle at which the waves are diffracted in a constructive manner is known as 2θ (Fig. 2.3.10) if there is a variation in the atomic plane spacing (d) there will be a change in 2θ the change in the spacing of atomic planes (d) will vary if residual stress is present within the component. Comparing the spacing (d) of a stressed material with that of the identical unstressed material, there may be a few Å of difference in the d -spacing, from this the strain can be calculated, then using Hooke's law the stress can be deduced (Whithers & Bhadeshia, 2001).

" The X-ray beam is directed onto the sample surface at the location of interest. The diffracted beam is detected by a position-sensitive proportional counter. The angular position (2θ) of the diffracted beam is used to calculate the distance (d -spacing) between parallel planes of atoms using Bragg's law. A series of measurements made at different X-ray beam approach angles (ψ) are used to fully characterize the d -spacing. The slope of the least squares fit on a graph of the d -spacing versus $\sin^2\psi$ is used to calculate the stress. " (Britannica, 2015).

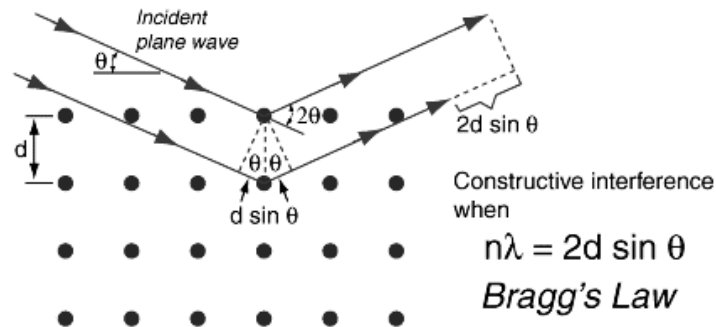


Fig. 2.3.10. A sketch representation of Bragg's Law (Britannica, 2015).

Changes in strain and thus the d -spacing translate into changes in the diffraction angle θ measured by the X-ray detectors. The diffraction pattern (Fig. 2.3.11) is in the shape of a cone for polycrystalline materials.

The shape of the diffraction peaks can also be related to the dislocation density and coherent domain size. The most common sources of errors and misapplications in stress measurements by X-rays are related to stress constant selection, focusing geometry, diffracted

peak location, cold-working crystallography, texture, grain size, microstructure, and surface roughness (Ruud et Farmer, 1978).

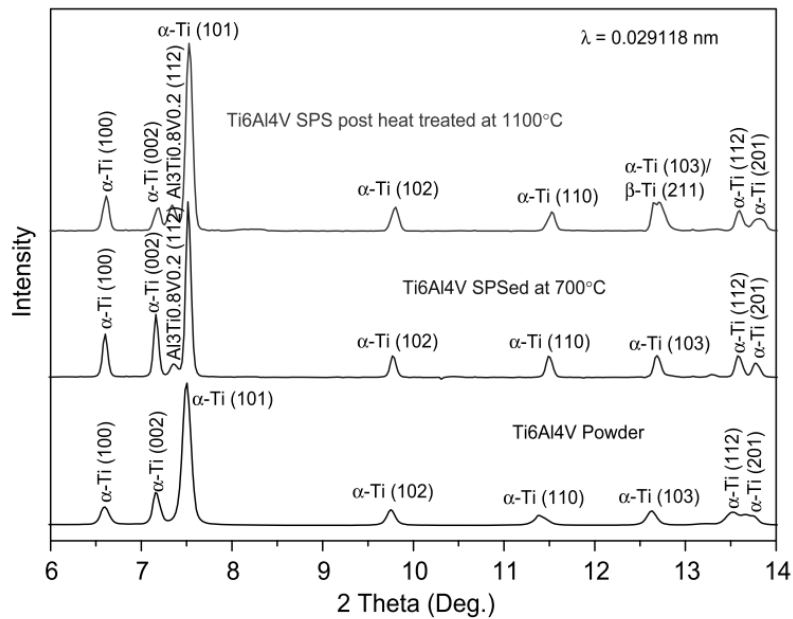


Fig. 2.3.11. Diffraction patterns of Ti6Al4V powder and spark plasma sintered Ti6Al4V foams (Quan *et. al.*, 2012).

XRD is effective in measuring type I and type II residual stresses within materials. This method is widely applied in industry because a large variety of samples large or small with complex geometry can be measured, also as a non-destructive method it is preferred for various reasons (in the case of layer removal it can be seen as semi destructive). XRD is to the author's knowledge the most commonly used non-destructive method to accurately measure residual stress in multiphase materials.

Neutron Diffraction, is capable of measuring the elastic strains induced by residual stresses throughout the volume of relatively thick steel components with a spatial resolution as small as 1 mm^3 . For residual stress measurements in most alloys, especially steels and cast irons, the unstressed spacing (d_0) between crystallographic planes at the exact point of strain measurement is not known and not easily measured. This means that d_0 and θ (*diffraction angle*) cannot be precisely established, and this leads to various degrees of error in the accuracy and precision of ND residual-stress measurements (Totten *et al.*, 2002).

The Hole Drilling Method (HDM) is among the destructive methods of residual stress measurement, which is most widely utilised and it has been applied with great success even for thin components. HDM consists of drilling a very small hole into the specimen (Fig. 2.3.12). Residual stresses relax in the hole while stresses in the surrounding area change causing strains also to change. Strain gauge rosettes are used for measuring these strains.

Three methods are available for estimating non-uniform residual stress fields from relaxed strain data for the incremental HDM: 1) Power Series, 2) the Integral and 3) the ASTM E837-08 Methods (ASTM E837; Casavola *et al.*, 2010-2011). However, the utilization of the strain gauge method has some practical disadvantages. Firstly, it requires the hole to be drilled exactly in the center of the rosette in order to avoid sizeable errors. Secondly, it only measures the average strain in the range of the length of the strain gauge and thus is inaccurate in terms of the planar stress gradient (Cheng *et al.*, 2008).

As indicated by Vishay Measurements Group (1993), the accuracy of the method depends on surface preparation, correct strain gauge rosette selection, installation of strain gauges, accurate alignment of the hole and correct selection of incremental hole depths. Since the stress gradient must be assumed to be constant across the hole or ring diameter, areas of high stress gradients should be avoided. At stresses which are higher than one third of the yield strength of the material, local plastic yielding during metal removal occurs.

Large errors in residual stress measurements can be caused by strain hardening of the steel in the vicinity of the hole which may occur during metal removal. Totten (2002) recommended that the thickness of the specimen must be at least four times the hole or core diameter. During the metal removal in different places of the part, the holes must be spaced apart at least eight times their diameter. Heating during drilling can affect results adversely while drilling at high speeds cause plastic deformation in Ti6Al4V. The residual stress measured could be partially influenced by this deformation as there also exists a thermal gradient during drilling (Barile *et al.*, 2014).

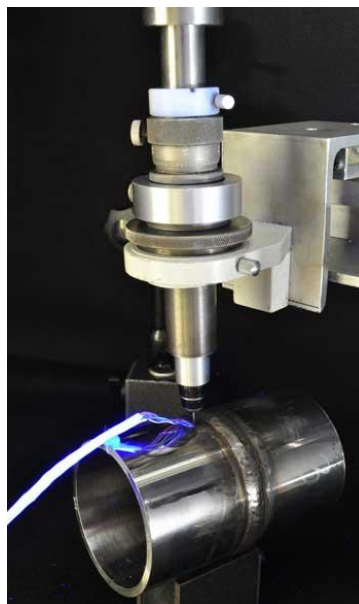


Fig. 2.3.12. HDM (Lambda Technologies, 2012).

Electronic Speckle Pattern Interferometry (ESPI) is an optical technique which enables interferometric measurements of surface displacements on almost any surface and material. The non-contact and full-field measurement allows the calculation of the three dimensional distribution of the displacement and strain/stress of the object under test as a response to a mechanical or thermal loading (Stresstechgroup, 2012). *Hole drilling and Electronic Speckle Pattern Interferometry* measures changes in the part surface resulting from hole drilling and determines the previously existing residual stresses, and surface distortion measures by ESPI in real-time, Fig. 2.3.13 portrays a basic experimental setup for ESPI (Barile *et al.*, 2011).

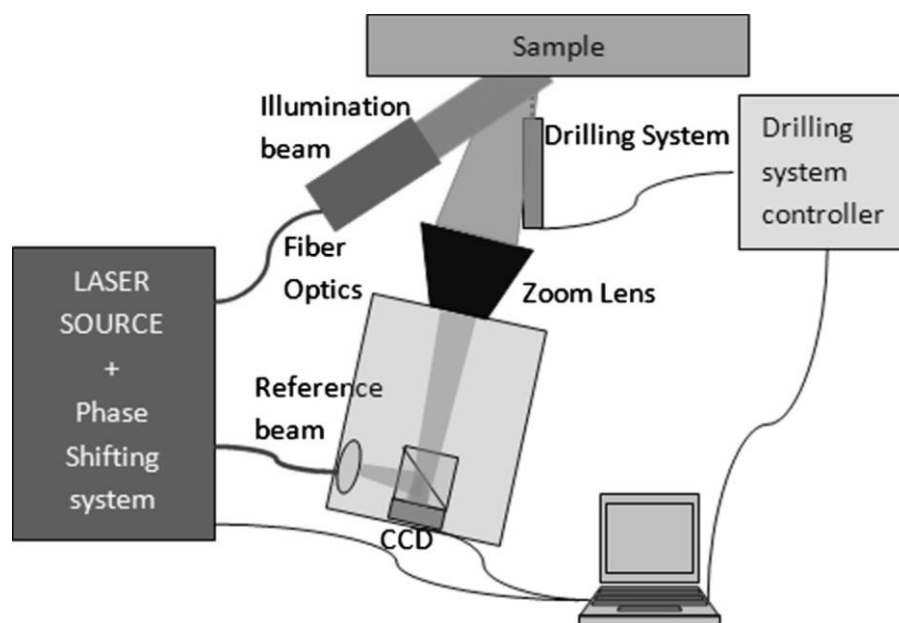


Fig. 2.3.13. Experimental set-up for ESPI measurements of strains relaxed by hole drilling (Barile *et al.*, 2014).

Contour Method is a solid mechanics superposition technique. This method helps predicting the residual stress in specimens via cutting a sample in two pieces. The deformation after cutting allows the relaxation of residual stresses. This deformation resulting from stress distribution (Fig. 2.3.14) can be modelled via appropriate numerical formulae and practical assumptions and be finitely analysed thus an accurate description of the two dimensional residual stresses normal to the cut plane can be determined. This method is typically performed on metallic parts utilizing the cutting of a wire Electric Discharge Machine (EDM). This method is not recommended for parts smaller than 5 x 5 mm² due to accuracy concerns, but this method is advantageous for complex, spatially varying residual stress fields and complex geometry parts (Olson *et al.*, 2015).

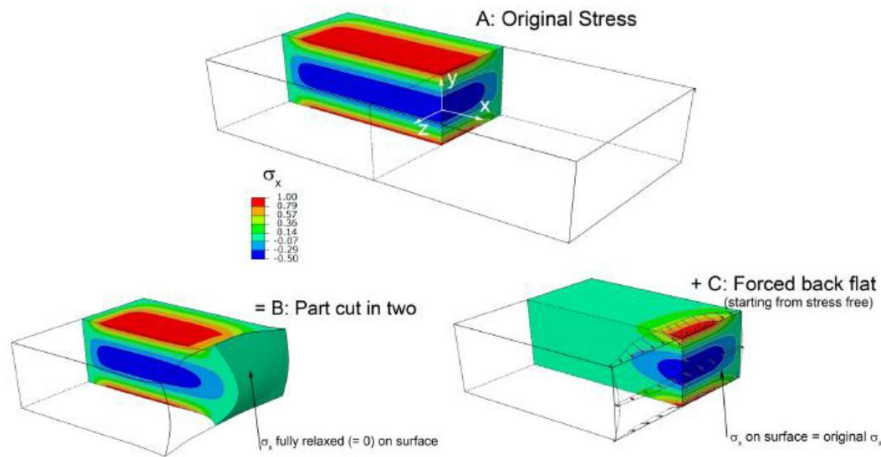


Fig. 2.3.14. The Contour Methods theoretical implementation (Olson *et al.*, 2015).

Curvature, this method is used by the natural curvature (Fig. 2.3.15) of a material experiencing residual stress, using the mechanical properties of the material one can mathematically determine the residual stress by the angle of the curvature (the angle determined by strain gauges or profilometry). This is only partially effective for Type 1 stresses. Buchbinder *et al.* (2014) used cantilevers for investigation of Al alloy distortion during DMLS. After cutting right and left of the part, the bending angle of the detached arms can be measured. Different residual stresses and magnitudes will lead to changes in the bending angle.

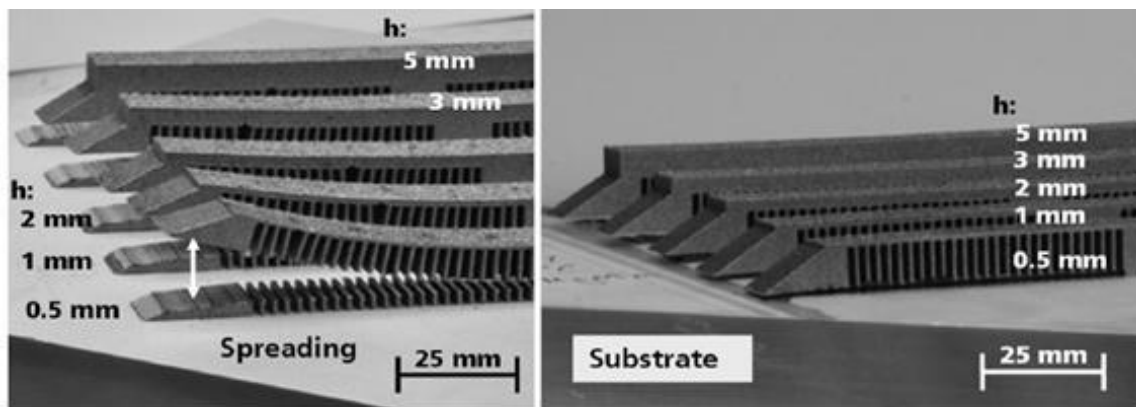


Fig. 2.3.15. Curvature of Cantilever due to Residual Stress (Buchbinder *et al.*, 2014).

Hardness testing is a method of determining specific material properties via a controlled testing method. The Vickers testing method is based on the basic principle of a materials ability to avoid plastic deformation. This involves a diamond indentation piece which is forced onto the material surface. The shape usually has a half angle of 60/63 degrees.

The force is predetermined to suit the test piece. An indentation then appears upon the surface of the material (Fig. 2.3.16) This indentation is then measured diagonally, the area of the indentation is thus determined, and so a force/area equation can be used to determine the hardness number HV/DVH because the area is not normal to the force it is not pressure that is calculated but a hardness number which can also be expressed in Pascal. When testing the hardness of a material which suffers from residual stress, the indentation may deform to a certain extent (or the residual stress may influence the hardness number). The magnitude of the deformity may be compared with that of a non-stressed part, the change in area (Fig. 2.3.16 (a-c)) of the indentation could be converted to strain which then can be converted to a stress value (Hooke's Law), which could then be compared with the XRD results (Totten, 2002).

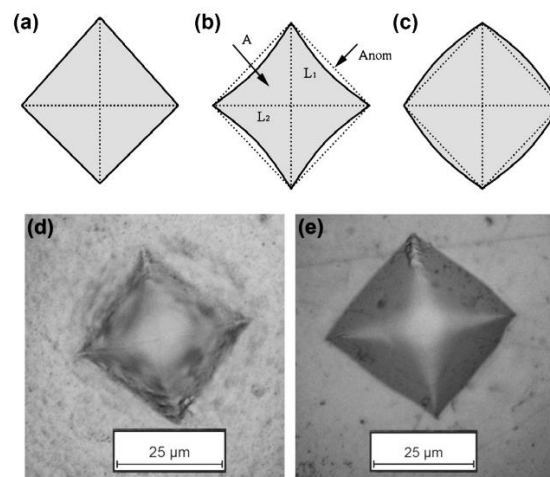


Fig. 2.3.16. Proposed deformation (a–c); Actual indentation (d–e), (Totten, 2002).

James *et al.* (2009, 2011) proposed to use correlation synchrotron or neutron diffraction data and hardness values for “*the life prediction of welds based on an understanding of how weld process conditions affect the mechanical and metallurgical factors controlling fatigue resistance in metals*” (Fig. 2.3.17).

Withers & Bhadesia (2001) states clearly that the appropriate technique must be chosen when investigating residual stress Table 2.3.2. Failure may not be due to the incorrect measurement of stress, but because the wrong stress component was measured. Therefore it is important to ascertain which stress component or type is important for the specific application at hand. In this study X-Ray diffraction was chosen as it is possible to not only consider all components of stress but also yields fairly accurate results.

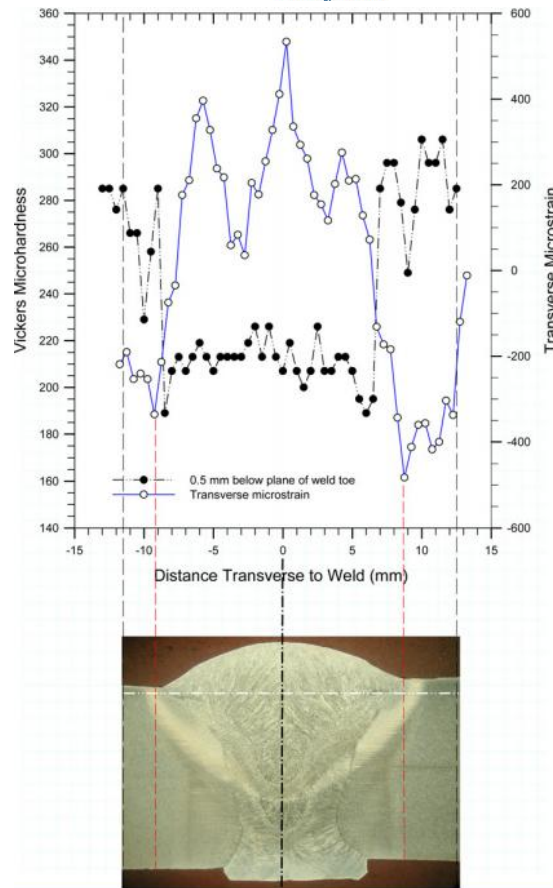


Fig. 2.3.17. Weld macrostructure, shown plotted on the same distance scale as the hardness profile and transverse strain gradient across a line 1 mm below the weld toe (James *et al.*, 2007).

Table 2.3.2. Methods of Measurement (Withers & Bhadeshia, 2001)

Method	Depth Penetration	Accuracy	Comments
Hole Drilling Method	~1.2 x hole diameter	±50 MPa limited by reduced sensitivity with increased depth	Measures in-plane Type I stresses, semi destructive
Curvature Method	0.1-0.5 of Thickness	Limited by minimum measurable curvature	Unless used incrementally, stress field not uniquely determined Type I
X-ray Diffraction	Tens of micrometers (material dependent)	±20 MPa limited by non-linearities	Non-destructive, sensitive to surface roughness, Type I, II, III
Neutrons	Material dependent up to 200 mm for Al	± 50 x 10 ⁻⁶ strain, limited by counting statistics	Access difficulties; low data acquisition rate; Type I, II
Ultrasonic	>100 mm	10%	Microstructure sensitive Type I, II, III
Magnetic	10 mm	10%	Microstructure sensitive, for magnetic materials only, Type I, II, III

2.3.5. Summary

In this section the definition, origin and nature of residual stress for processes is explained as well as the detrimental effects of residual stress. There is an overview of the different types of residual stress. Also the different techniques for measurement of residual stress with their respective advantageous and disadvantageous are discussed.

2.4. Residual Stress in DMLS objects

2.4.1. Origin and Cause of Residual Stress in As-built DMLS Specimens

The macro-residual stress present in parts produced by AM is known as thermal residual stress, solidification during rapid thermal change induce and lock-in these stresses within a component (Vrancken *et al.*, 2014; Yadroitsev & Yadroitsava, 2015). The residual stress observed with DMLS deteriorates the parts performance dramatically and induces distortion (Klingbeil *et al.*, 2002).

According to Vrancken (2013), “*in general, of the major metal additive manufacturing techniques, DMLS suffers most from residual stresses. Furthermore, residual stress modelling efforts for DMLS face difficulties due to the small scale at which the phenomena are taking place, which drastically increases computational time*”.

DMLS as most AM technologies involve rapid thermal changes during production. As the laser beam fuses the powder together it keeps moving, allowing atmospheric cooling of the newly fused layer. This thermal gradient induces residual stress within the as-built part from the DMLS process (Denlinger *et al.*, 2015). This is not the only influence on the DMLS part, the physical phenomena of the material changing from one phase to another affects (as it melts and combines) the residual stress (Type II), especially in alpha-beta alloys where the phase change from alpha to beta adversely effects the amount of stress induced between the lattice structures (Elmer *et al.*, 2005). The crystal structure change that is undergone by a multiphase material in the case of Ti6Al4V as such produces a martensitic crystal structure (mentioned later in this study) this indicates a displacive transformation (Totten *et al.*, 2002) the shape change is an *invariant-plane strain* (IPS) indicating shear strain on a intergranular level.

Residual stress induce dependent on varying factors, still needs to be confirmed in the DMLS process. For example; solidification theory states that materials with little thermal diffusivity are more likely to result in greater thermal residual stress. Materials with low diffusivity retain greater heat due to a higher specific heat capacity these materials are also

unable to dismiss the heat due to low thermal conductivity. These specific properties lead to greater thermal gradients within components produced by DMLS and consequently large residual stress.

The degree of expansion of a material divided by the temperature change during expansion is known as the materials coefficient of thermal expansion (CTE). The CTE, as a property of a material, changes with the temperature, this almost seems counter intuitive (Fig. 2.4.1). This change of the property due to temperature is known as temperature dependant property of a material, materials have various temperature dependant properties. Yield strength of titanium declines with the increase in temperature shown in Fig. 2.4.2, this indicates that there might be a possibility that when the laser radiation is melting the powder particles together that the residual stress when solidification occurs might be greater than the yield strength of the titanium at that specific temperature when it solidifies, inducing distortion and delamination.

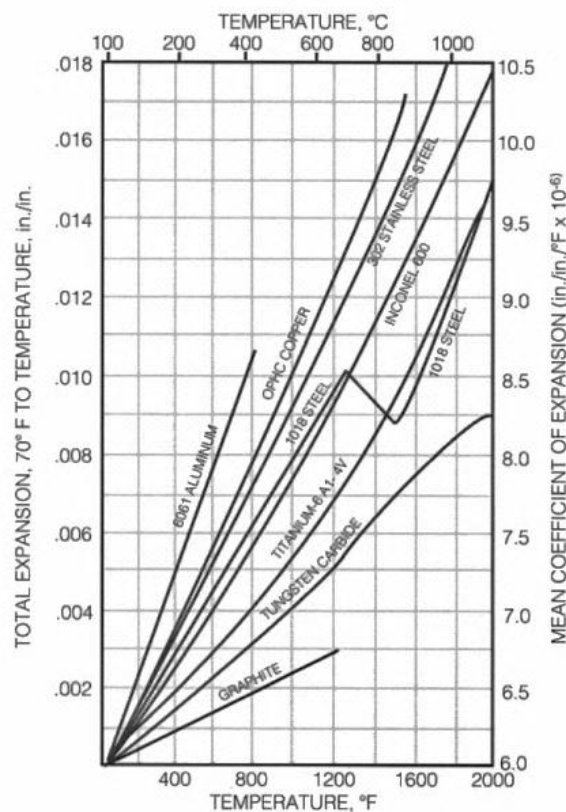


Fig. 2.4.1. Thermal Expansion Curves for several metals (Kay, 2010).

Volume change has its part in the DMLS process as well, shrinkage or the reduction in volume due to rapid cooling or solidification, though limited in the DMLS process, none the less leads to strain in the part, as already solidified layers constrain the physical shrinkage

of the top layer, leading to residual stress within the component (Fig. 2.4.3) (Vrancken *et al.*, 2013).

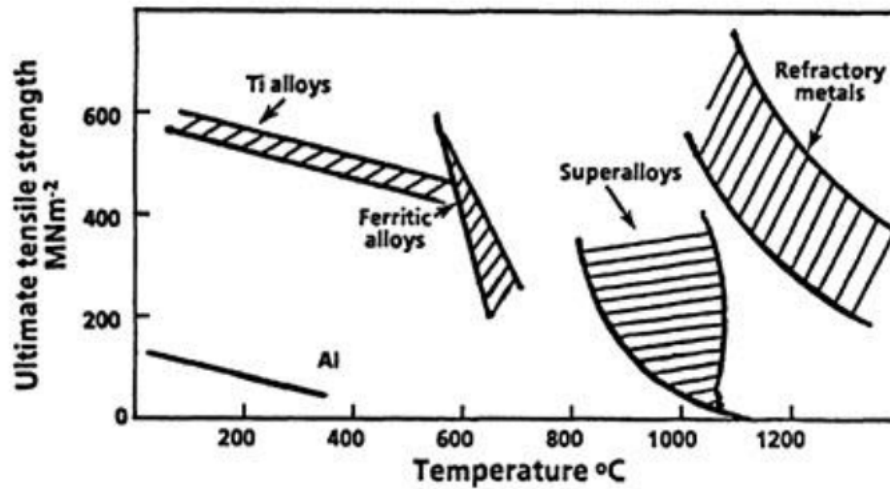


Fig. 2.4.2. Tensile strengths of a number of alloys as a function of temperature to indicate temperature ranges over which different alloy systems may be used (Key to Metals AG, 2015).

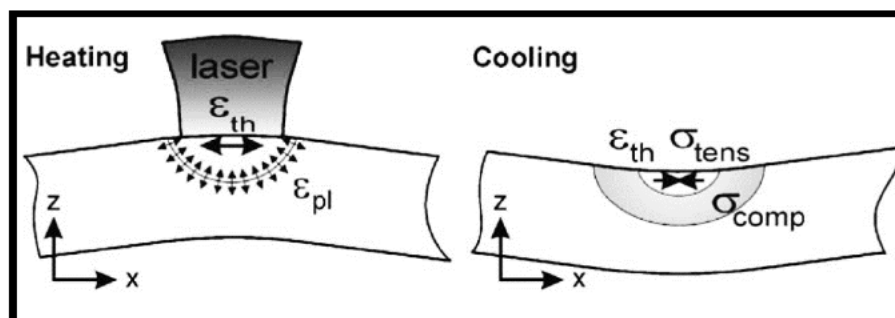


Fig. 2.4.3. Schematic showing Heating and Cooling phenomena of laser passes (Kruth *et al.*, 2003).

When the molten pool cools down and solidifies, the shrinkage occurs in all directions, although perpendicular to the scanning direction shrinkage will be small, yet in the longitudinal direction it will be much greater, this leads to longitudinal residual stresses in the scanning direction (Gusarov *et al.*, 2013). This clearly indicates that on a micro-scale metallurgical phenomena must be understood in a holistic manner to anticipate stress propagation and crack growth within materials used in DMLS. Understanding the material properties and their thermal characteristics are vital for effective DMLS application. However material characteristics also only play a partial role (Vrancken *et al.*, 2013).

Machine process parameters discussed earlier are equally if not of greater importance, the input parameters play an important role in the material bonding and build up as they influence the aforementioned factors.

Due to the anisotropic nature of the stress and the process involved with DMLS it is difficult in most cases to find a conclusive correlation between the residual stress and material parameters. Vrancken (2013) found in his particular study of 9 different materials introduced to DMLS (316L stainless steel, Ti6Al4V ELI, Ti grade 2, 18Ni300 maraging steel, W, AlSi10Mg, Ta and Hastelloy C-276), a clear did not exist relationship between the material parameters and residual stress (Fig. 2.4.4).

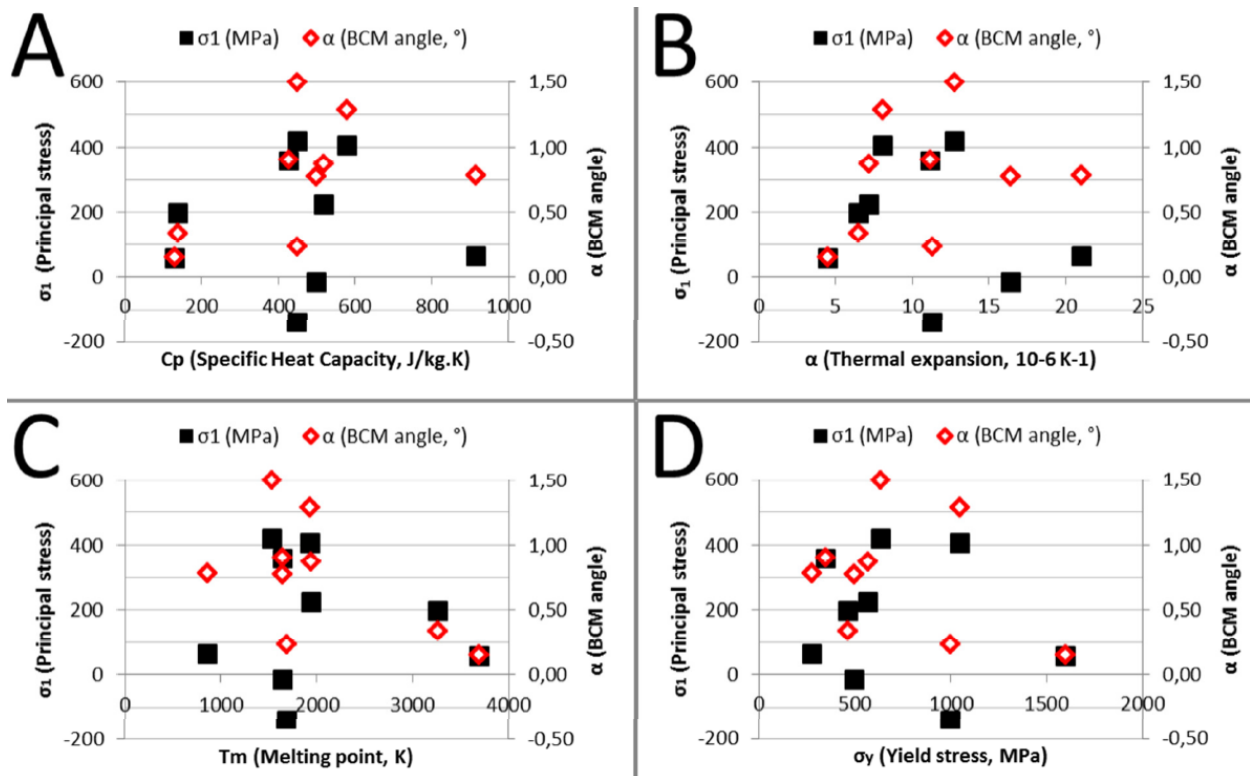


Fig. 2.4.4. Graphical representation of the stress related measurements, σ_1 and the curl-up angle α in function of selected material properties (Vrancken *et al.*, 2013).

Residual stress within DMLS as mentioned is a result of large thermal changes, it can be assumed that any parameter process-parameter will play a role within the residual stress experienced by the as-built component. Shiomi *et al.* (2003) found that up to 55% of the initial residual stress can be relieved using re-scanning strategy (Fig. 2.4.5).

Yadroitsev & Yadroitsava (2015) found that the applied one-zone strategies of SS 316L and Ti6Al4V alloy lead to symmetrical solidification in front of the tracks. The residual stresses in the SLM objects were tensile and in the direction of the scanning it was higher than in the perpendicular direction for all specimens, regardless of the height of the sample. An in-depth measurement of residual stresses in the SS 316L samples showed that the maximum stress was reached at the point where the sample joins with the substrate, and the

residual stresses varied considerably from layer to layer. High thermal gradients resulted in high residual stress in the SLM samples. Elaboration of preheating regimes and scanning strategies to decrease thermal gradient during the manufacturing of big complex-shape parts is an important task.

Pohl *et al.* (2002) studied different scanning patterns and found that the lowest warpage of direct metal laser sintered plate-shaped specimens was for the scanning patterns type ‘Stripes’ and ‘Squares’.

Zaeh and Branner (2010) by neutron diffractometry studied residual stresses in cantilevers from 18Ni Maraging 300 steel as a function of the scanning strategy (Fig. 2.4.6 – 2.4.7). The island-scanning type caused lowest residual stresses, a longitudinal scanning lead to the highest values of stresses.

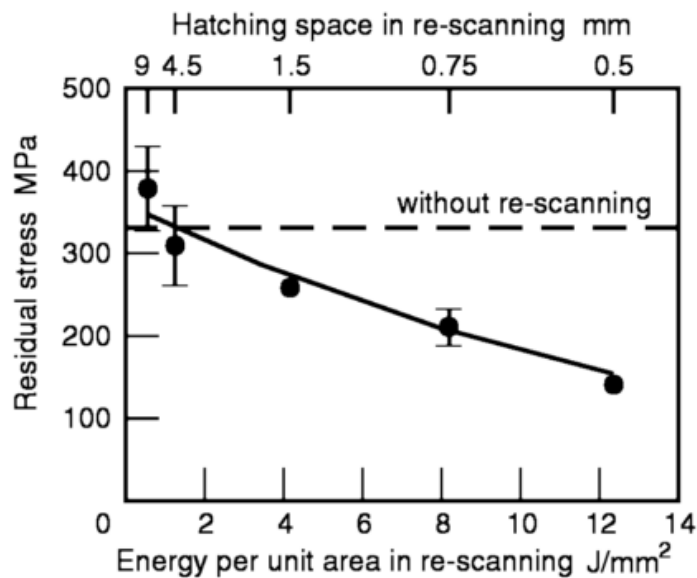


Fig. 2.4.5. Re-Scanning of SLM samples (Shiomi *et al.*, 2003).

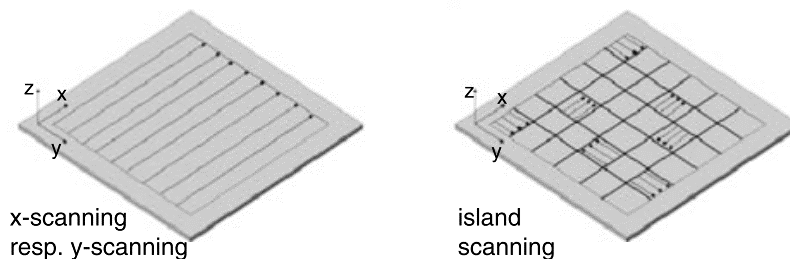


Fig 2.4.6. Scanning strategies (Zaeh & Branner, 2010).

Mercelis *et al.* (2006) found that before separating from the substrate the sample produced by random sector exposure had the stresses equally large in X and Y direction. The base plate removal yielded a large reduction of stress levels (2-3 times), this most likely due

to distortion of the parts when removed from the substrate which would have a releasing effect on the crystal lattice.

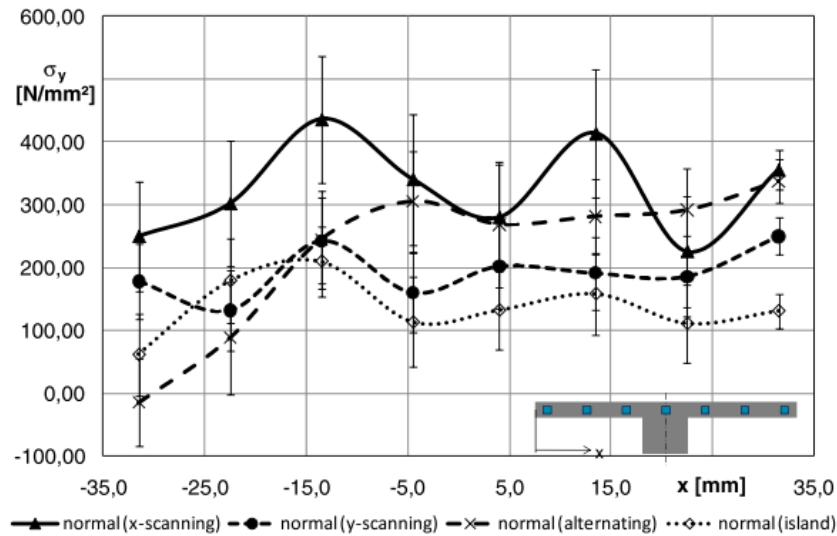


Fig. 2.4.7. Residual stress in cantilevers (Zaeh & Branner, 2010).

There is a strategy known as stochastic exposure which Concept Laser says it employs successfully which works on the bases of an island scan strategy principle. This scan strategy has the laser scanning squares of the part geometry (Fig. 2.4.8) which may vary from 1 mm x 1 mm to 10 mm x 10 mm. It is proposed that 5 mm x 5 mm squares produce the smallest residual stress though no conclusive test results are given. This strategy is also claimed to be piloted by Hoffman Innovation who claim to be able to produce large volume parts with minimal distortion, though no mention of post processing is made (Concept-Laser, 2015; Hoffman-Innovation, 2015).

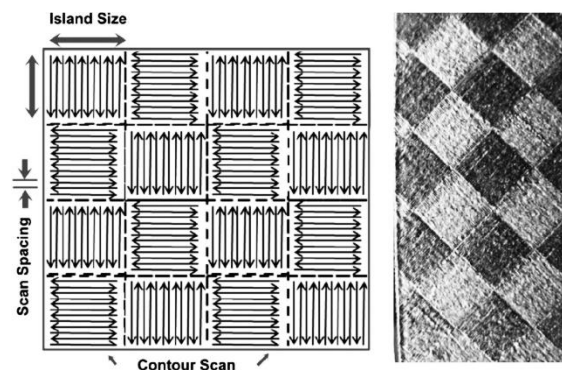


Fig. 2.4.8. Island Scan strategy with real image to the right (Qiu *et al.* 2013).

Rotating and changing the scanning pattern per layer is also an option as residual stress is not an isotropic occurrence, this approach could lower residual stress and also result in residual stress being spread more evenly throughout the part.

Kruth *et al.* (2012) applied a bridge curvature method for investigating residual stress in Ti6Al4V samples. It was shown that deformation of the bridges diminished with the length of the scan tracks. A hypothesis was suggested that the shorter scan tracks (Fig. 2.4.9) led to a smaller temperature gradient owing to the higher remnant heat of the previous scan line. It was also estimated that post-heat treatment reduced the thermal stresses more than optimizing parameters for the island scanning strategy.

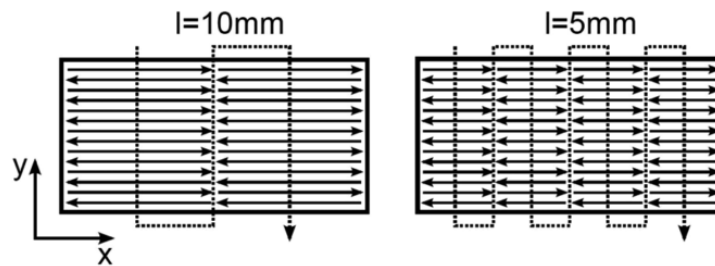


Fig. 2.4.9. Short scan tracks (Kruth *et al.*, 2012).

As was shown by Vrancken *et al.* (2013), orientation and building direction play a role in the residual stress present (Fig. 2.4.10 & 2.4.11) thus one can conclude that by changing the orientation of the part in relation to the substrate and then also the building direction of that part will influence the residual stress distribution and magnitude.

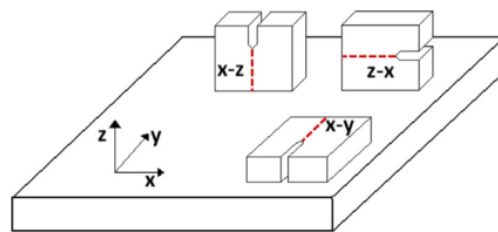


Fig. 2.4.10. Part Orientation of DMLS components on substrate (Vrancken *et al.*, 2013).

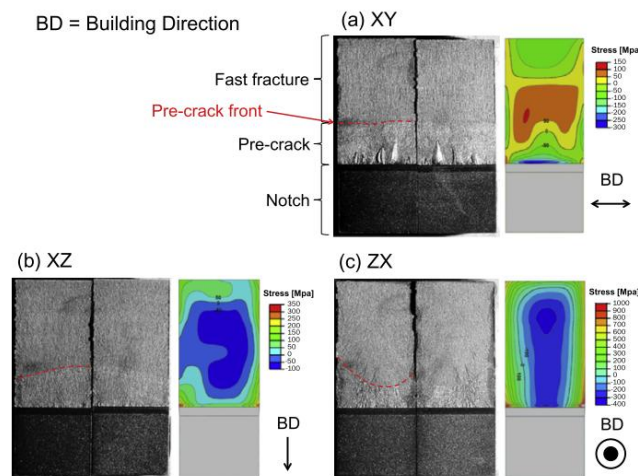


Fig. 2.4.11. Residual stress in samples manufactured by DMLS with different orientation (Vrancken *et al.*, 2013).

Sanz & Navas (2013) sintered DMLS parts with an H-type geometry from the three materials and four different points namely A, B, C and D were measured by XRD (Fig. 2.4.12). The residual stress in the lateral face of the component was significantly lower (B, C, D) than on the top surface (A). They concluded that it was due to the inter-layer heat transfer during the process relaxing the residual stress on the lateral surface. Residual stress is clearly not spread homogeneously throughout the component (Fig. 2.4.13) (the residual stress however does exist in a balanced state). Also noteworthy at point A, the residual stress differed for all materials: in Inconel 718 it was 200 MPa (tensile), in CoCr block RS was 40 MPa (tensile) and in Maraging, Steel –350 MPa (compressive). These are vastly different values, with porosity at a minimum, quality parts are assured. The difference in residual stress seems to be material dependant, depending on the material related properties such as thermal conductivity, heat capacity, thermal expansion, elastic modulus and Poisson's ratio, plasticity, thermodynamics and kinetics of transformations, mechanisms of transformations and transformation plasticity. Also it was shown that shot peening homogenized surface residual stresses (Fig. 2.4.13). Resulting compressive residual stress is high and can be beneficial to the fatigue behaviour of the DMLS parts (Sanz & Navas, 2013).

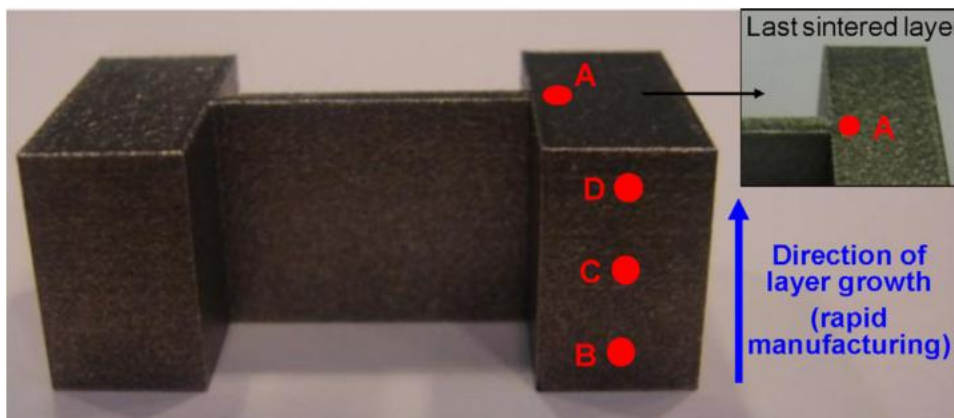
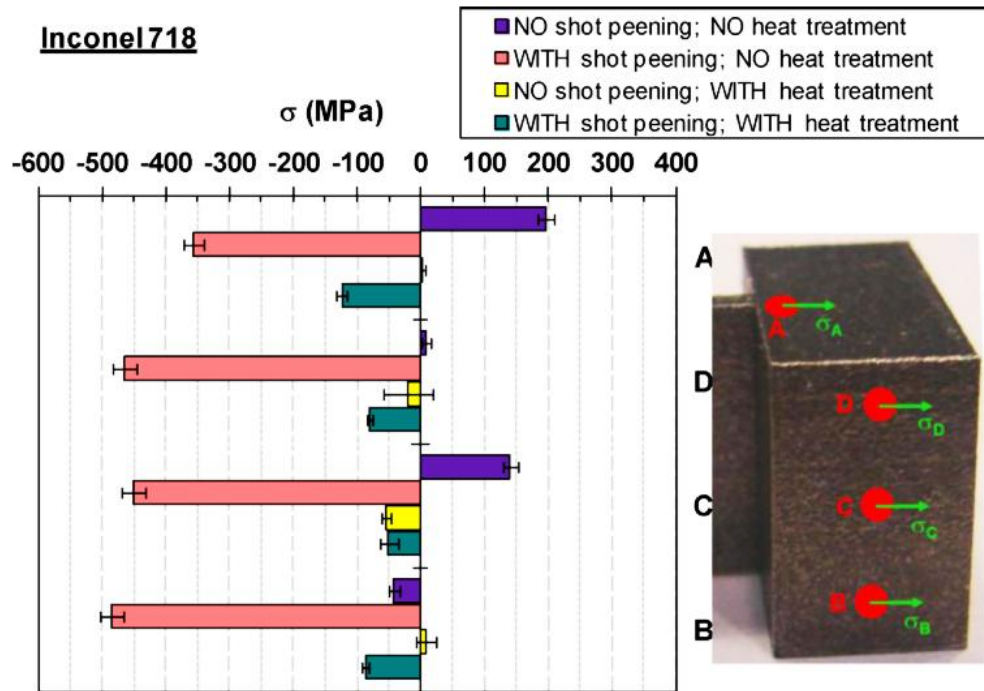


Fig. 2.4.12. H-Geometry samples produced by DMLS (Sanz & Navas, 2013).

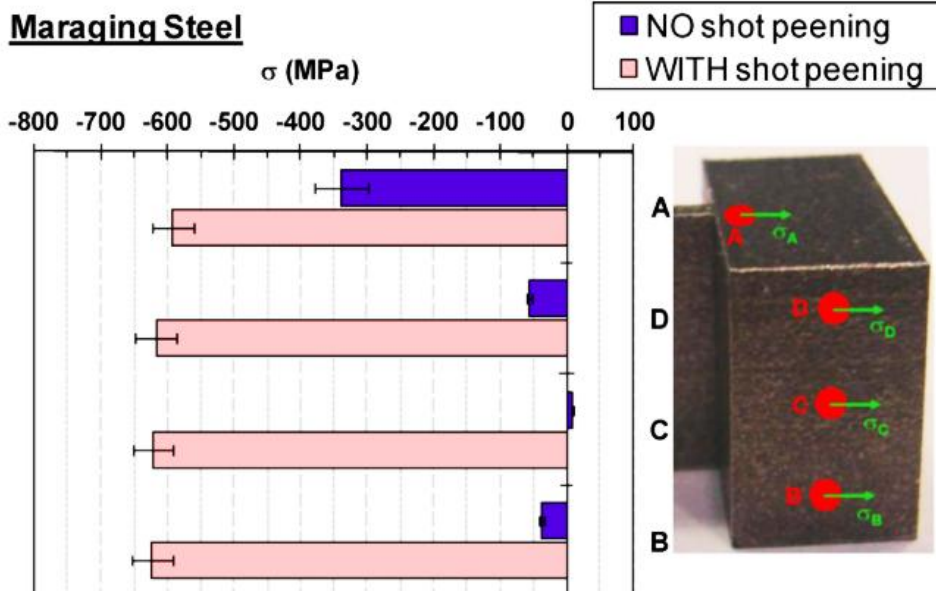
The thickness variations of complex 3D parts have a role in part distortion as thinner edges of the material lack the toughness to overcome the forces associated with residual stress. Residual stress effects are directly proportional to the distance over which it acts. As these stresses are not homogeneous, it influences distortion and for the moment also makes residual stress less predictable in complex 3D components.

Mercelis *et al.* (2006) found that residual stresses increased with height of the samples Fig. 2.4.14. The scanning strategy also played a part in the thermal stresses since they found

that with the island strategy residual stress was lower than with single direction exposure strategy.



(a)



(b)

Fig. 2.4.13. a) Residual stress measured at different points on an Inconel 718 part surface produced by DMLS, b) Residual stress measured at different points on a Maraging Steel part surface produced by DMLS (Sanz & Navas, 2013).

Casavola *et al.* (2009) found that the residual stress in AISI 300 Steel was the highest in the top layer of the components (Fig. 2.4.15), they utilized the HDM measurement method for their study, they also concluded that throughout the thickness of the sample stress was non-uniform, which indicates that stress might not increase with sample height.

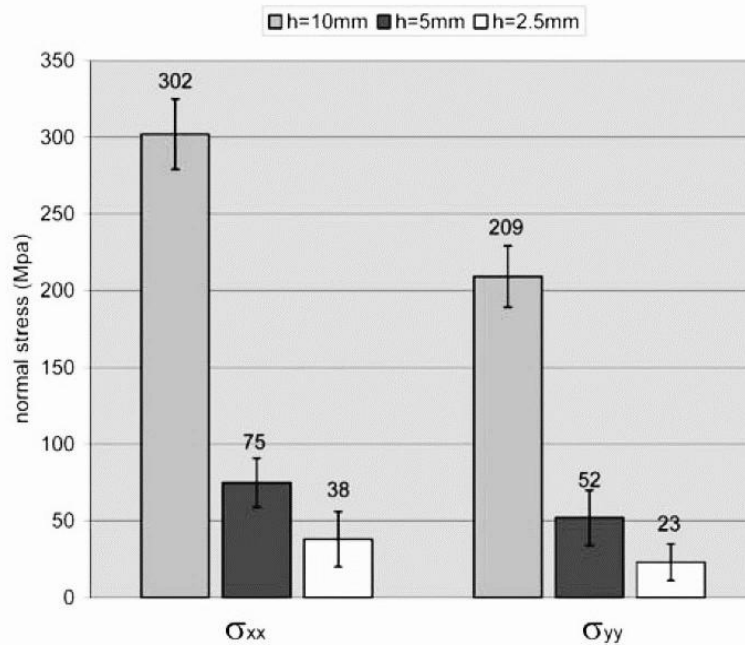


Fig. 2.4.14. Stresses shown to increase with the height of DMLS samples (Merzelis *et al.* 2006).

Shiomi *et al.* (2003) studied the effect of preheating, showing that residual stress could be lowered in this way by choosing appropriate preheating temperatures, results of preheating the substrate shown Fig. 2.4.16.

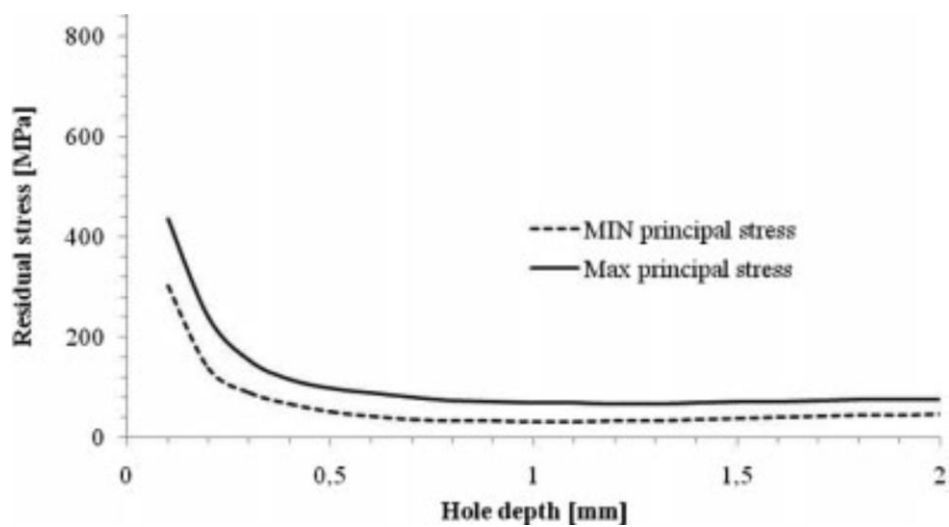


Fig. 2.4.15. Residual stress shown to be highest in the top layers (Casavola *et al.*, 2009).

Furumoto *et al.* (2010) investigated the residual stresses with strain gauges in the samples from 70% Cr-Mo steel powder, 20% Cu alloy powder and 10% Ni (in weight) powder. There were tensile stresses within the SLM samples and these values were extremely large at the top surface and at the boundary between the substrate and the consolidated structure (about 800 MPa). It was shown that residual stress at the first layer was decreased when the base plate was heated before consolidating the deposited powder; when each of the consolidated layers was repeatedly heated by the laser beam irradiation, the residual stresses also decreased.

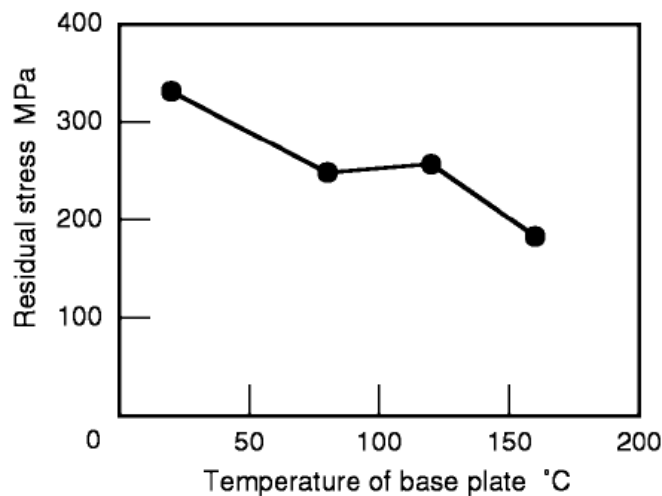


Fig. 2.4.16. Relationship between residual stress and temperature of base plate (Shiomi *et al.*, 2003).

When cooling in DMLS happens to rapidly the large thermal gradient induces residual stress. Slowing down the cooling speed by preheating the substrate resulted in a reduction of residual stress of up to 40% according to Shiomi's (2003) results, using chrome molybdenum steel (JIS SCM440) mixed with copper phosphate and nickel powders. He also theorised that the residual stress might even be halved if the substrate is preheated above or up to 250°C.

In a recent study Vrancken (2015) found that preheating of the substrate for Ti6Al4V DMLS is effective in lowering the residual stress, though utilizing an individual set of process parameters, there was some porosity present in samples which could also account for some lower residual stress levels. Preheating to different temperatures was done (Fig. 2.4.17) and residual stress declined more noticeably at 200°C and more.

The XRD results were cross referenced with the Curvature Method (discussed earlier) and the conclusion was coherent to that of XRD analysis. The obtained microstructure of Ti6Al4V alloy was more Beta prevalent equiaxed structure (Fig. 2.4.18). Oxidation of the

samples however occurred during the preheating process which decreased the ductility of the components (Vrancken *et al.*, 2015).

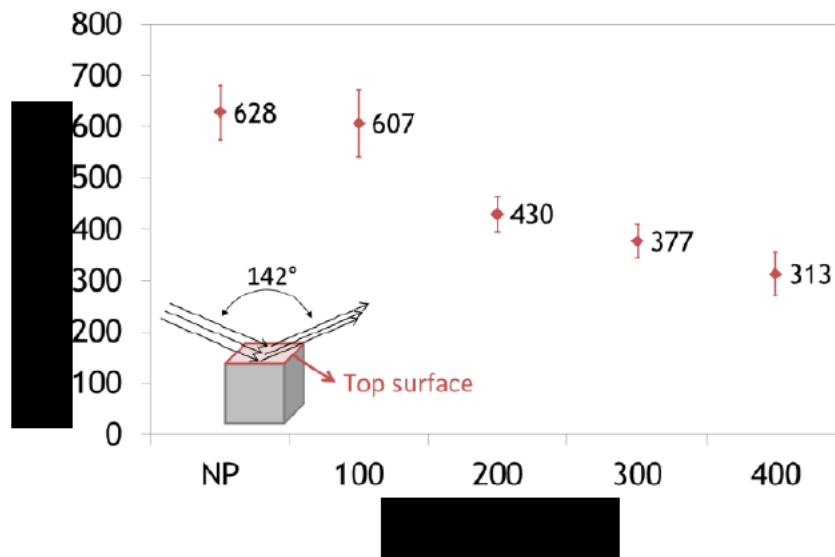


Fig. 2.4.17. Residual stress in Ti6Al4V DMLS samples *versus* preheating temperature (Vrancken *et al.*, 2015)

When working with titanium alloys, it is important to mention that at elevated temperatures the atmosphere control is more critical. Donachie (2002) explained that for welding, titanium and its various alloys will readily pick up hydrogen, nitrogen, carbon and oxygen at temperature of 500°C and above. These interstitial elements will lead to embrittlement and most likely a loss of ductility. He also suggested that for oxygen content as low as 3000 ppm for the welding atmosphere transverse cracking might occur in welds, which should be noted as the DMLS process has steep thermal gradients comparable to welding. Transverse cracking has been noted to occur in single track formation.

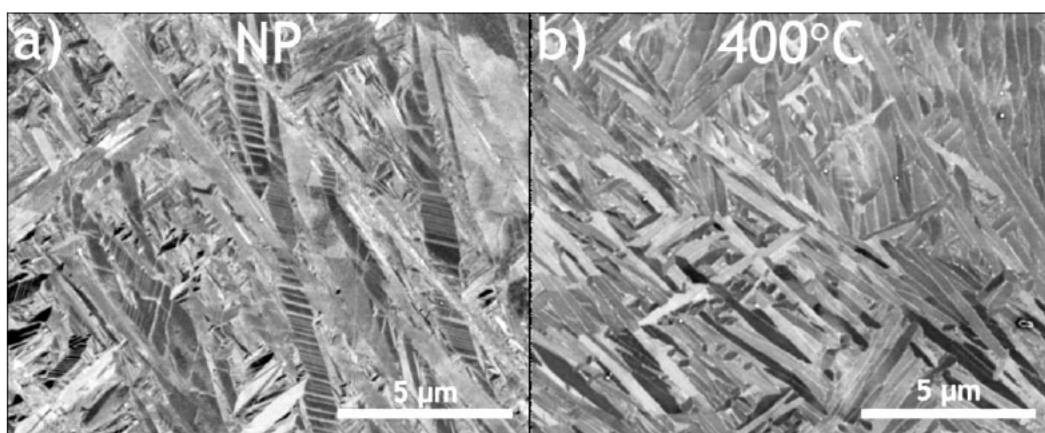


Fig. 2.4.18. (a) Microstructure of DMLS Ti6Al4V component without preheating (b) and with 400°C preheating (Vrancken *et al.*, 2015).

2.4.2. Stress-Relieving Treatment of DMLS Specimens

Heat treatment can be described as a controlled process in which heating of components and thereafter cooling of said components are used to alter the microstructure of the material to impart certain mechanical properties pertaining to application of the object (Cheng *et al.*, 2012). Heat treatment can also be used in successfully reducing residual stress within components (Donachie, 2000).

Residual stresses induced during DMLS can deform parts after dislodging from the substrate (when deformation/delamination does not occur during manufacturing). A simplistic and basic heat-treatment before the part is removed from the substrate ensures stress relief and minimal or no distortion (CAMAL, 2015; Knowles *et al.* 2012). For chrome molybdenum steel (JIS SCM440) powder mixed with copper phosphate and nickel powders heating has been shown to be effective as well removing up to 70% of residual stress (Shiomi *et al.*, 2003).

For conventionally produced Ti6Al4V alloy, stress relieving heat treatment is between 480-650°C (Table 2.4.1.). Ti6Al4V will oxidize in normal condition when heated above 427°C therefore treatment must take place in an oxygen depleted atmosphere i.e. vacuum furnace or argon furnace. Donachie (2000) states that the cooling rate for stress relieving of titanium alloys is not critical, but the uniformity of cooling is of critical importance. Furnace or air cooling is acceptable but quenching is not advised as it might lead to residual stresses due to non-uniformity of cooling. He also states that 90% or more of the residual stress in Ti6Al4V is relieved within the first hour at temperature of 595 °C (Fig. 2.4.20).

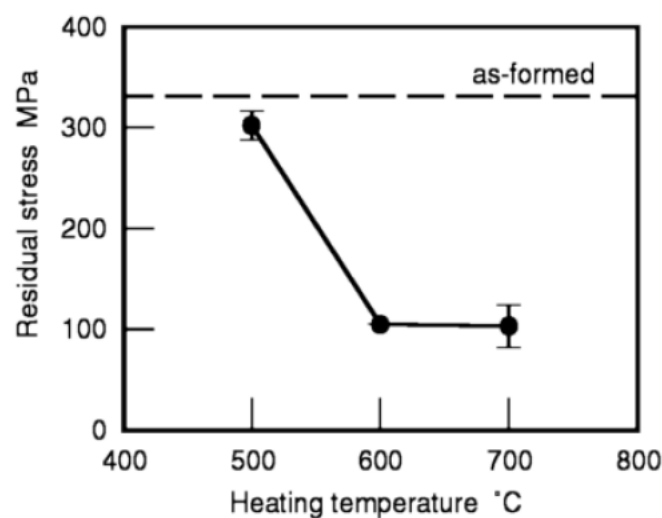


Fig. 2.4.19. Relationship between residual stress in top layer of model and heating temperature in stress relieving treatment (Shiomi *et al.*, 2003).

Table 2.4.1. Heat Treatment of wrought Ti6Al4V (Dynamet-Holdings, 2000).

Mill Anneal	705-790°C ; 1-4 hours ; air cool
Stress Relief	480-650°C ; 1-4 hours ; air cool
Beta Anneal	1035 °C ; 30 min ; air cool 730 °C ; 2 hours ; air cool
Recrystallization Anneal	925 °C ; 4+ hours ; furnace cool to 760 °C at 55 °C/h or slower cool to 480 °C At 370 °C/h or faster ; air cool

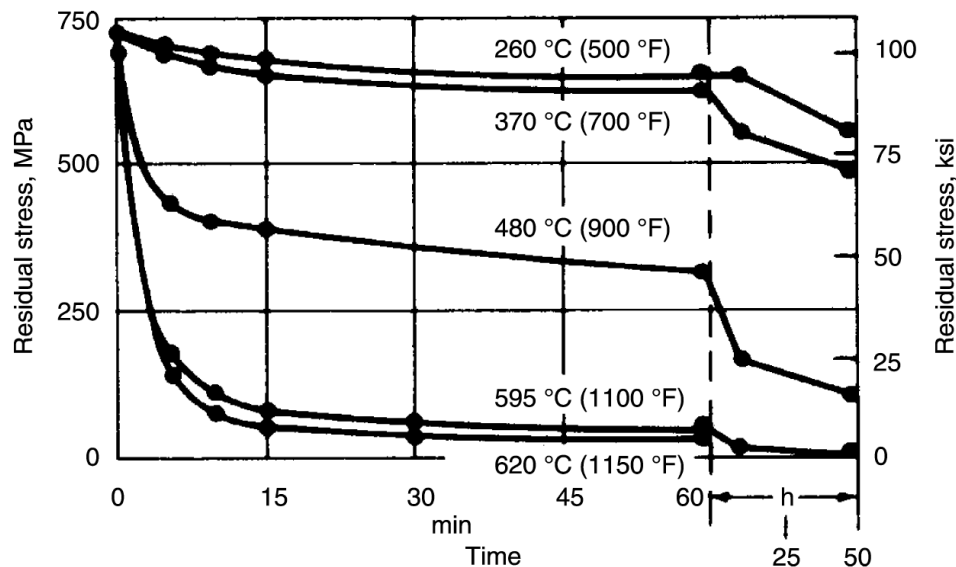


Fig. 2.4.20. Relationship between time and amount of residual stress relief at various stress-relief anneal temperatures for Ti6Al4V alpha-beta alloy (Donachie, 2000).

Leuders *et al.* (2012) found that in the as-built Ti6Al4V shows weak crack growth performance statistics (Fig. 2.4.21) but after post treatment, at 800°C, 1000°C and HIP they found that fatigue crack growth performance was improved. The treatment process most of which transformed the microstructure releasing most internal stress and thus a change in performance properties occur (Fig. 2.4.22).

Another post processing treatment used on DMLS components is Hot Isostatic Pressing (HIP) this involves heating and pressurizing said component in a furnace, this has the effect of almost eliminating all porosity and also transforming the martensitic structure (Fig. 2.4.22) leaving a β -enriched structure which lowers the UTS of the material but still within accepted standards the great advantage is in the increase of ductility, it also relieves almost all residual stress (Qiu *et al.*, 2013).

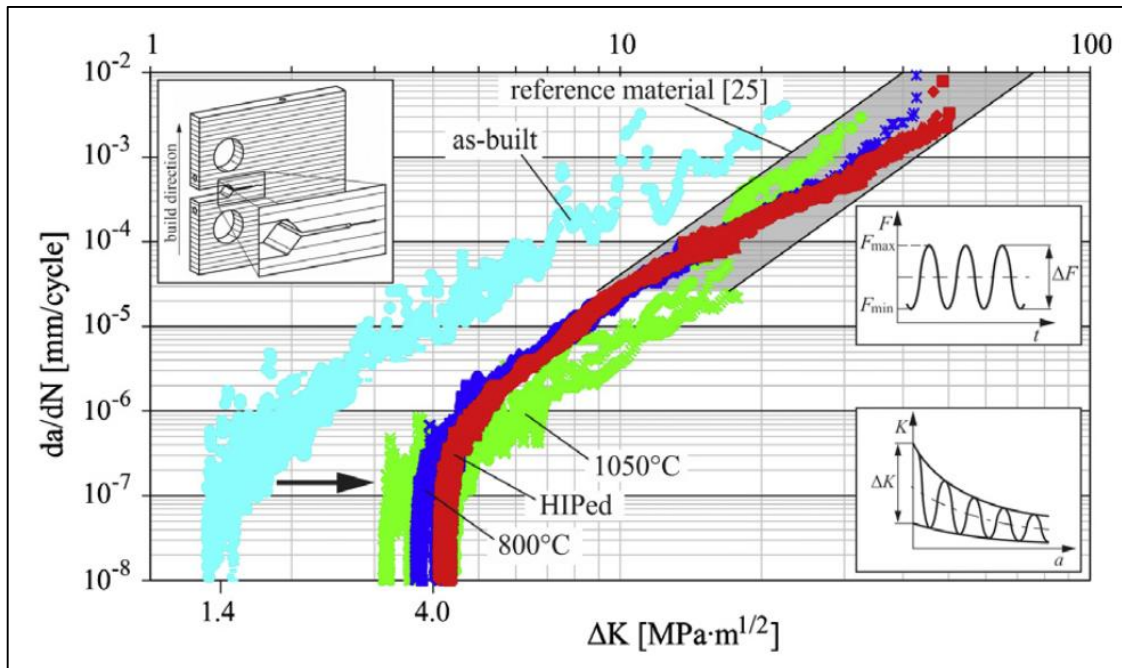


Fig. 2.4.21. Crack Growth Performance (Leuders *et al.*, 2012).

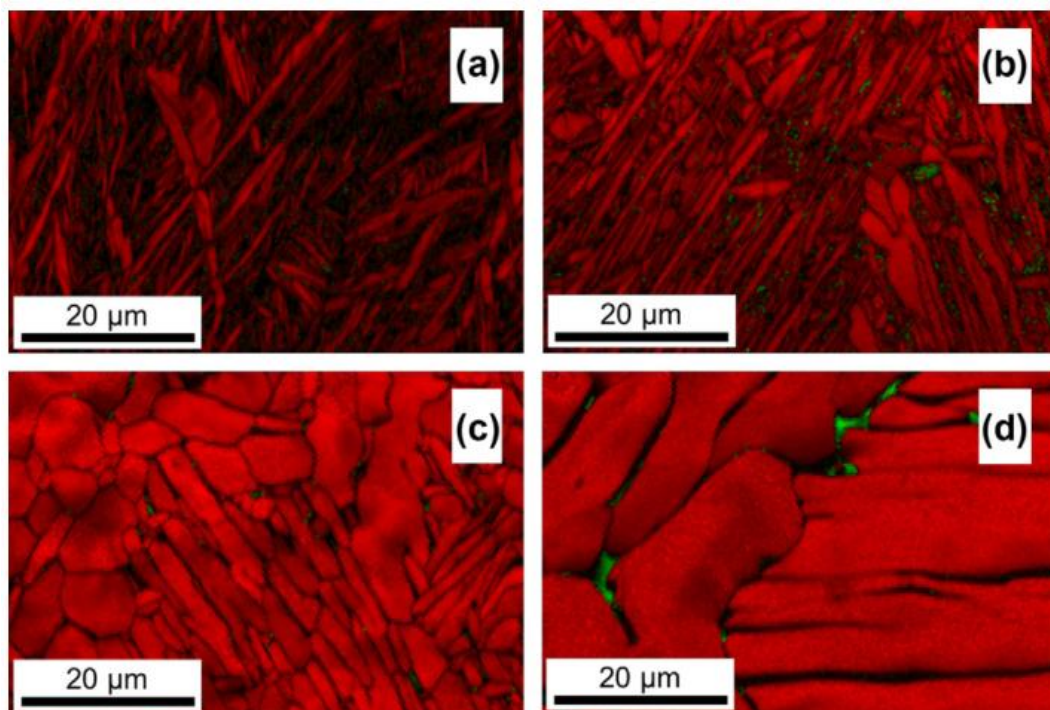


Fig. 2.4.22. Microstructure of Ti6Al4V DMLS samples: as-built (a), heat treated at 800°C (b), after HIP (c), after HIP at 1050°C (d) (β -phase in green) (Leuders *et al.*, 2012).

2.4.3. Summary

The effects of residual stress varies widely as mentioned earlier, yet within the specific DMLS process there are significant characteristics which are detrimental to the AM industry. Residual stress during the sintering process can cause a part to detach itself from the

substrate (delamination) or its respective supports inducing process-stop and of course part failure (Fig. 2.4.23).

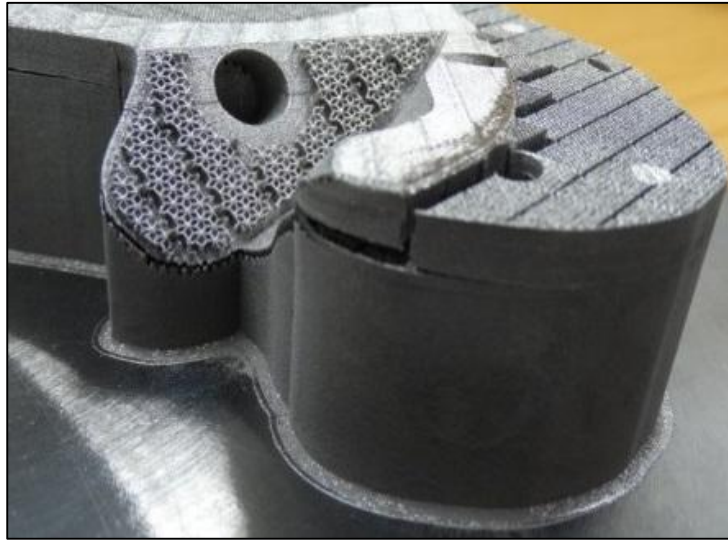


Fig. 2.4.23. The delamination of Ti6AL4V DMLS part from the support structures during manufacturing.

Delamination clearly also indicates a part which has undergone geometric changes due to residual stress, in the medical industry distortion or torsion by only a couple of micron could be detrimental to possible patient application. Even if delamination does not occur parts have been known to deform after being removed from the substrate.

Yet delamination during the process causes powder bed disturbance (Fig. 2.4.24). When a part delaminates during the process of manufacturing (mostly from support structures or substrate), its height usual changes to such an extent that there is contact between the delaminated part and the powder recoater (Fig. 2.4.25). This of course damages the machine which is not optimal, but the brief contact causes the part to flex and then relax, the part acts as a spring load which then moves or shoots powder away from the contact area, this possibly influences other parts on the substrate. The conclusion is multiple part failure and machine damage.

Crack propagation is a clear indicator that the ultimate tensile strength of the material of the component has been exceeded (Fig. 2.4.26). Usually delamination would occur prior to cracking, it seems to develop when a part is most rigidly attached to the substrate, geometries such as sharp corners must try and be avoided by the engineer, as these create a ‘spike stress’ situation, though the stress distribution in complex parts are yet to be fully investigated.

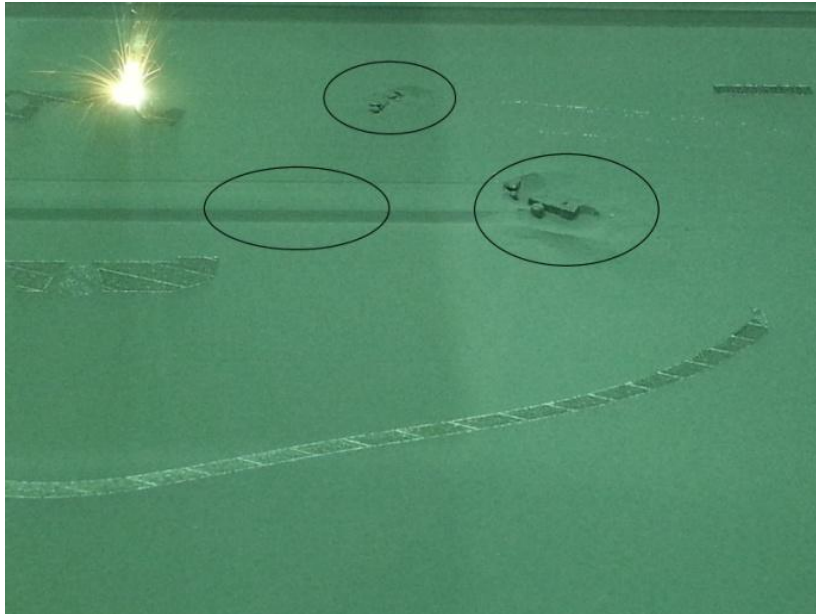


Fig. 2.4.24. Powder bed disturbance.

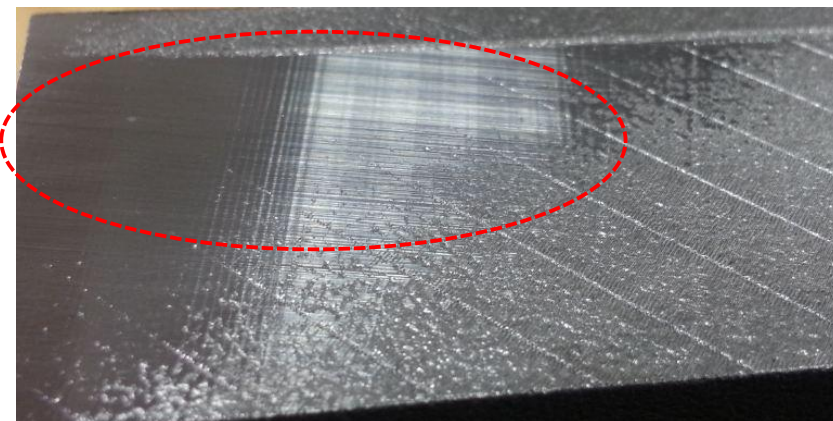


Fig. 2.4.25. Recoater blade contact with DMLS object, scrape marks seen as 'polished' area.

Though some institutions are looking into the effective modelling and prediction of residual stress via software development and analysis, simulation of single tracks is possible, but for complex components, analysis and simulation is difficult.

When it is possible to successfully produce stress prone objects (majority of the volume in either the X or Y axis Fig. 2.4.27) without triggering in process failure, these parts are still under immense stresses and deflect or warp when removed from the substrate without prior stress relieving. Table 2.4.2 shows the deflection of these components once removed from the substrate (via EDM) without prior stress relieving. The deflection incurred will render most components unfit for application, and this is a serious concern.



Fig. 2.4. 26. Crack propagation throughout DMLS object produced from Ti6Al4V.

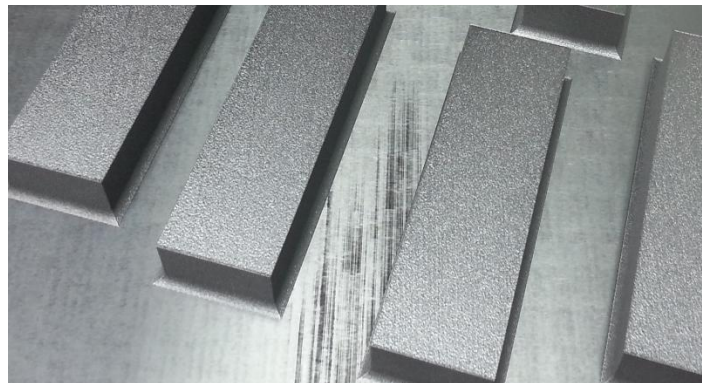


Fig. 2.4.27. Longitudinal orientated rectangular blocks as-built (still attached to substrate).

Table 2.4.2. Deflection due to residual stress

Deflection (mm)	No.1	No.2	No.3	No.4	No.5
Front (0 mm)	0	0	0	0	0
Middle (50 mm)	0.12	0.26	0.23	0.32	0.38
Back (100 mm)	-0.18	-0.15	0.16	0.2	0.4
Maximum deflection (mm)	0.14	0.26	0.27	0.34	0.42

*The deflection measured was with respect to the front of the rectangular block the results basically portray a concave shape or curve due to high residual stress.



As an overview for this section real cases of DMLS and residual stress from literature have been presented, discussed and also analysed with some clear distinctions were made by different authors. Also included were some cases at CRPM where this study was conducted. Knowing the nature and the magnitude of stress present within a component of any material is critical due to the failure it may impose on the components performance. This is a clear drawback to safe aerospace and medical application as the most stringent of material tests must be passed.

Chapter 3: Material and Methods

The aim of this study is to determine the residual stress in Ti6Al4V (ELI) components, produced by DMLS using standard EOS process parameters, as well as the post-processing treatment required to relieve the residual stress. As reported in Chapter 2, reports exist that quantifies residual stress magnitudes in SLM/DMLS components however none specifically for the M280 machine and also not with standard EOS process parameters.

To determine residual stress and its origin, within DMLS components, multiple factors need to be taken into consideration. These factors include for example, the possible influence of surface roughness on the residual stress values obtained via XRD or the quality of polishing on studying microstructures with a scanning electron microscope (SEM). In terms of this research it is important to know the intricacies that might influence essential variables, so that a logical error is not made. Fig. 3.1.1 shows a chronological order in which processes and experiments were conducted to obtain relevant results for analysis.

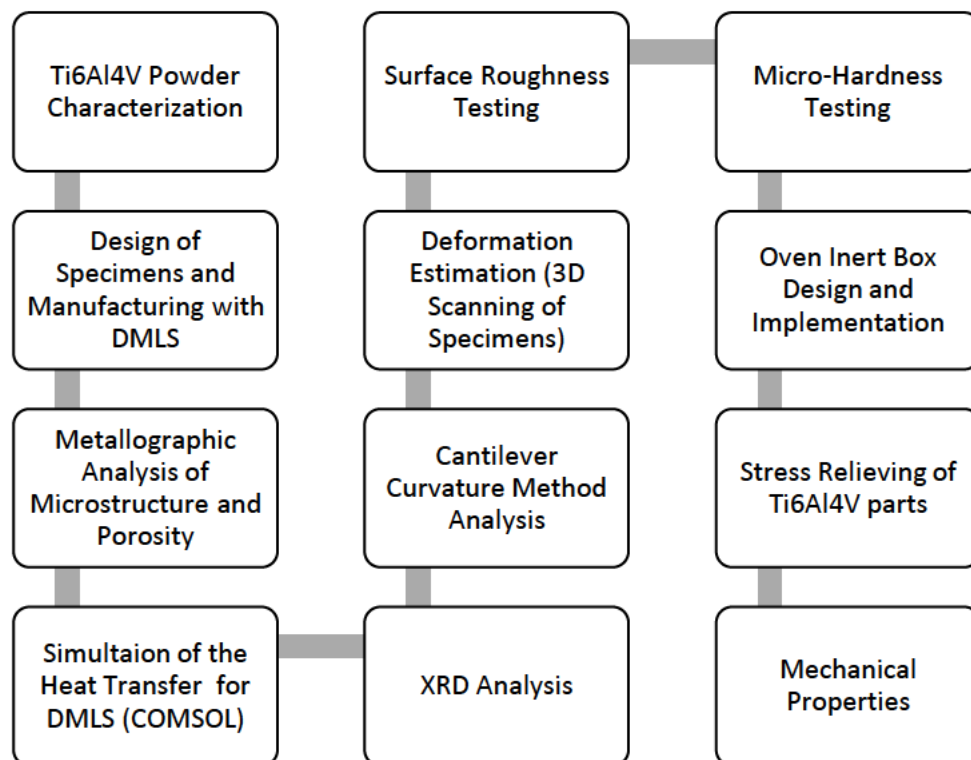


Fig. 3.1.1. Flow Diagram showing the processes followed during this study.

3.1. Ti6Al4V (ELI) alloy

Titanium materials have been most readily applied in the aerospace industry with specific applications in gas turbine engines for static and rotating components. Titanium is also used in other sections of the aircraft, namely fuselage, nacelles, landing gear, wing, and empennage, and also in the floor support structure, including areas of galleys and lavatories. As a side note, titanium application in the automotive industry started in the 1980's and has since gained favorable status, because of its weight saving capabilities in engine components such as valves and connecting rods (Fig. 3.1.2).



Fig. 3.1.2. A titanium connecting rod for an internal combustion engine (AMT, 2015).

Titanium alloys have accelerated the development of biocompatible implants over the past four decades, more specifically Ti6Al4V (ELI) (Leuders *et al.*, 2013). Ti6Al4V is a titanium alloy which consists of 6% Aluminium and 4% Vanadium by weight. ELI is short for Extra-Low Interstitial, this derivative of Ti6Al4V contains a low level of impurities. This material fulfils the chemical requirements for the standard of medical implants according to ASTM F 136/ISO 5832-3 specifications. Nowadays, the applications of Ti6Al4V alloy include hip and knee prostheses, trauma fixation devices (plates, screws, and wires), instruments, and dental implants. Cardiac valve prostheses, pacemakers, and artificial hearts are also made from titanium alloys. Due to its relatively poor wear resistance, the Ti6Al4V alloy is not suitable for bearing surface applications such as hip heads and femoral knees without a coating or surface treatment.

A few properties of Ti6Al4V are temperature dependant, that is to say that as temperature rises these properties actually changes qualitatively and quantitatively. Fig. 3.1.3 – 3.1.5 show some prominent temperature dependant properties of Ti6Al4V.

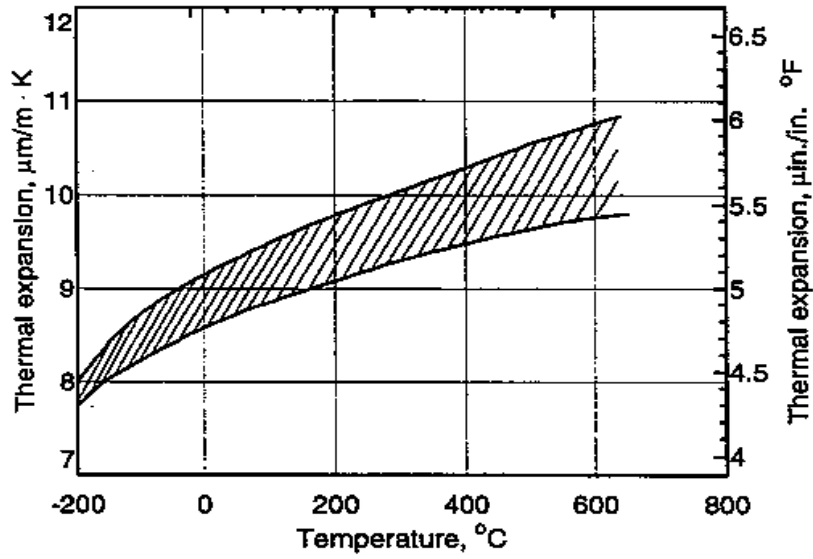


Fig. 3.1.3. Thermal expansion coefficient of Ti6Al4V *versus* temperature. (Dynamet Holdings Inc., 2015).

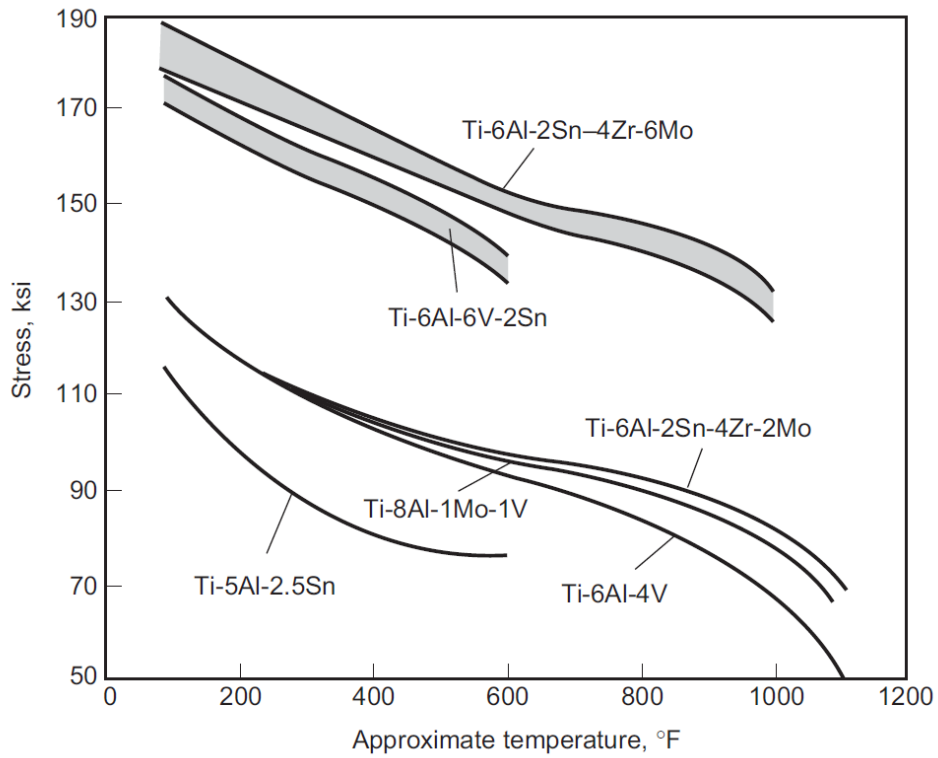
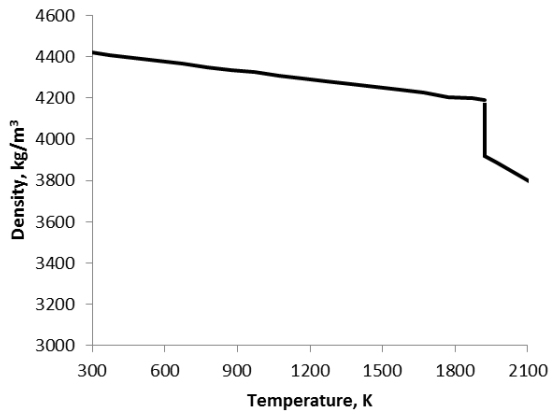
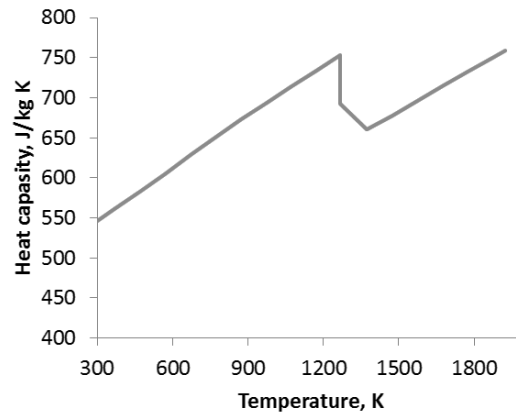


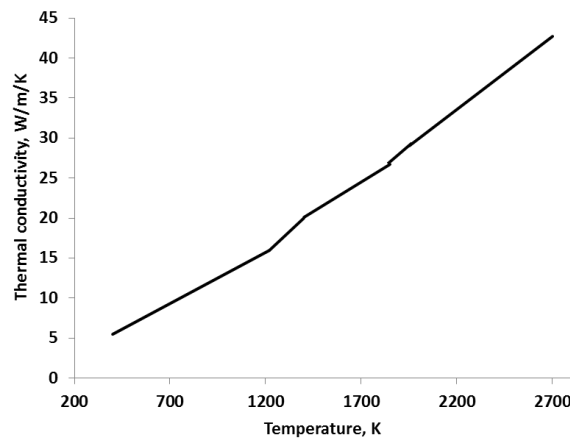
Fig. 3.1.4. Comparison of typical ultimate tensile strengths of selected titanium alloys as a function of temperature (Donachie, 2000).



(a)



(b)



(c)

Fig. 3.1.5. Temperature-dependent density (a), heat capacity (b) and thermal conductivity (c) of Ti6Al4V alloy (Mills, 2002; Boivineau *et al.*, 2006).

Titanium is an allotropic element and two types of crystalline formation can occur within the material. Hexagonal close packed (HCP) (Fig. 2.3.8) crystalline structure known as alpha (α), stable at room temperature, phase transformation takes place at a higher temperature, known as β -transus, where the crystal structure changes to a body centered cubic (BCC) (Fig. 2.3.8) a crystalline structure known as beta (β) (Styger *et al.*, 2014). The α -phase is stabilized at higher temperatures by an alpha stabilizer such as aluminium, tin or zirconium while the β -phase is stabilized at lower temperatures by a beta stabilizer such as vanadium, chromium, iron etc. (Jardini *et al.*, 2014). Ti6Al4V (ELI) is α - β alloy where the stabilizing elements are aluminium and vanadium.

The typical Ti6Al4V crystal structures obtained at various cooling rates are displayed in Fig. 3.1.6. This further explains Donachie (2000) emphasis on the cooling rate and how it affects the different textures of grain growth as well as the specific structure that forms.

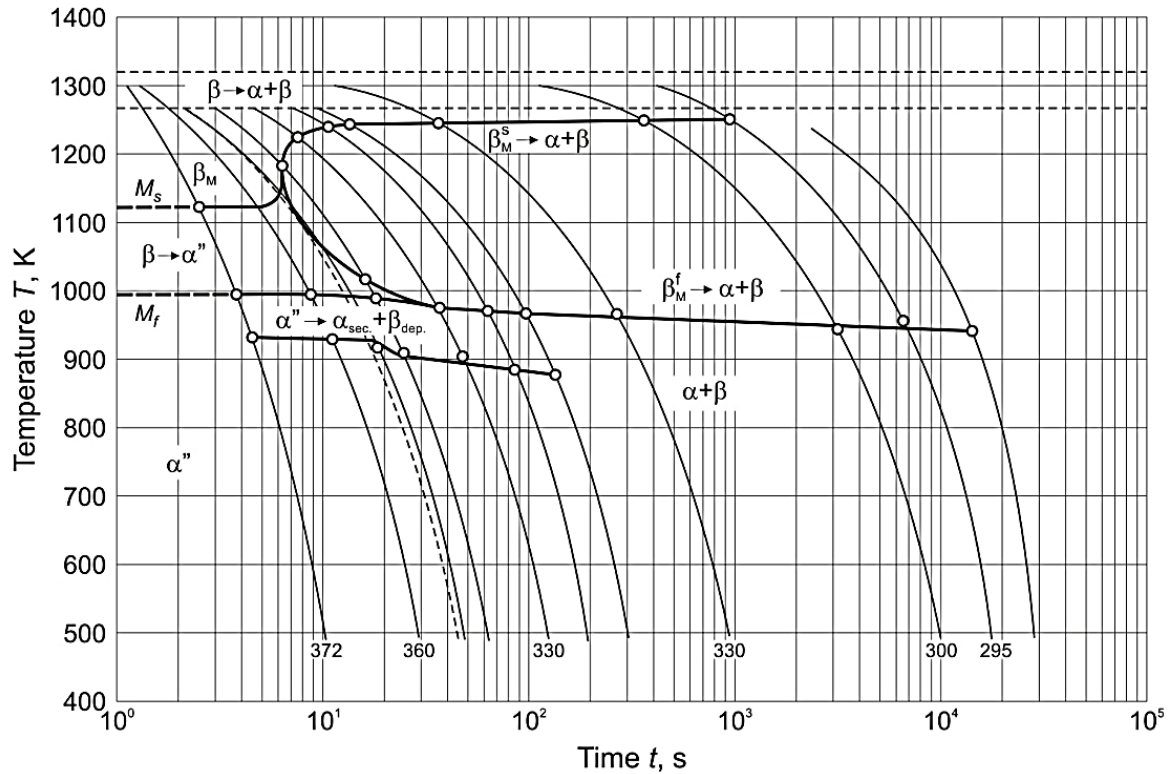


Fig. 3.1.6. The type of crystal structure formation for different cooling rates of Ti6Al4V (Dabrowski, 2011).

The word ‘wrought’ is the past participle of the 13th century English verb ‘work’. Metals are usually cast during manufacture and can be used in that condition but tend to be brittle, have a coarse microstructure and contain segregation of different constituents. The properties can be markedly improved by working - the grain structure is refined, mechanical properties improved, etc. Usually the cast structure is broken down by hot working which can be followed (but not necessarily required) by cold working. The material will have been ‘wrought’ by these operations (Engineering.com, 2016). As Donachie (2000) wrote: “Titanium alloys are particularly sensitive to the processing conditions that precede their use in service applications. Processing denotes the wrought, cast, or powder methods used to produce the alloy in the appropriate condition for the intended application, as well as the heat treatments that are applied to the alloy”. Wrought Ti6Al4V has a structure depending of course on the treatment process that has been applied to the material. In Fig. 3.1.7 it shows an equiaxed wrought material microstructure, the specific state of the material microstructure contributes toward the performance and mechanical properties of the component produced.

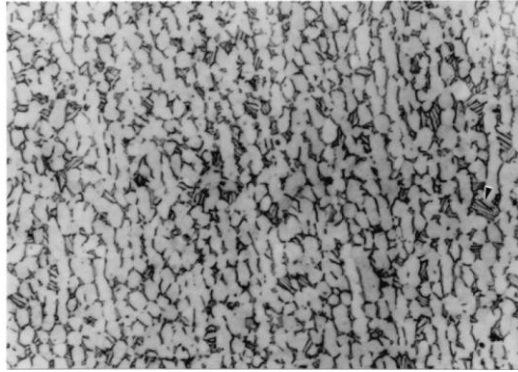


Fig. 3.1.7. Wrought Ti6Al4V (Murr *et al.*, 2009).

Wrought Ti6Al4V has been qualified for aerospace and bio medical fields for quite a number of years, and is known as the ‘workhorse’ of the titanium industry. For DMLS Ti6Al4V to be considered and qualified for these lucrative applications the DMLS processed material must display properties equal to or better than that of the wrought material. The wrought material properties for Ti6Al4V are listed in Table 3.1.1.

Table 3.1.1. Physical and mechanical properties of wrought Ti6Al4V alloy (Aero, 2015)

Specific Heat Capacity	0.5263 J/g-°C
Density	4430 kg/m ³
Thermal Conductivity	6.7 W/m-K
Melting Point (Solidus /Liquidus)	1604 - 1660 °C
Beta Transus	980 °C
Hardness, Brinell	334
Hardness, Knoop	363
Hardness, Rockwell C	36
Hardness, Vickers	349
Tensile Strength, Ultimate	950 MPa
Tensile Strength, Yield	880 MPa
Elongation at Break	14 %
Reduction of Area	36 %
Modulus of Elasticity	113.8 GPa
Compressive Yield Strength	970 MPa
Bearing Yield Strength	1480 MPa
Poisson's Ratio	0.342
Charpy Impact	17 J
Fracture Toughness	75 MPa-m ^{1/2}
Shear Modulus	44 GPa
Shear Strength	550 MPa
CTE, linear 20°C	8.6 µm/m-°C
CTE, linear 250°C	9.2 µm/m-°C
CTE, linear 500°C	9.7 µm/m-°C

3.2. Ti6Al4V (ELI) powder characterization

A chemical composition of the employed spherical argon-atomized Ti6Al4V (ELI) ($-45 \mu\text{m}$) powder from TLS Technik is shown in Table 3.2.1. The 10th, 50th and 90th percentiles of equivalent diameter (weighted by volume) of the powder were $d_{10} = 12.64 \mu\text{m}$, $d_{50} = 22.93 \mu\text{m}$ and $d_{90} = 37.03 \mu\text{m}$, respectively (Fig. 3.2.1).

Table 3.2.1. Chemical composition of Ti6Al4V powder (in weight %)

Ti	Al	V	O	N	H	Fe	C
ASTM standard Ti grade 23							
88.1 – 91	5.5-6.5	3.5-4.5	≤ 0.13	≤ 0.030	≤ 0.0125	≤ 0.25	≤ 0.080
Employed powder							
89.263	6.31	4.09	0.12	0.009	0.003	0.20	0.005

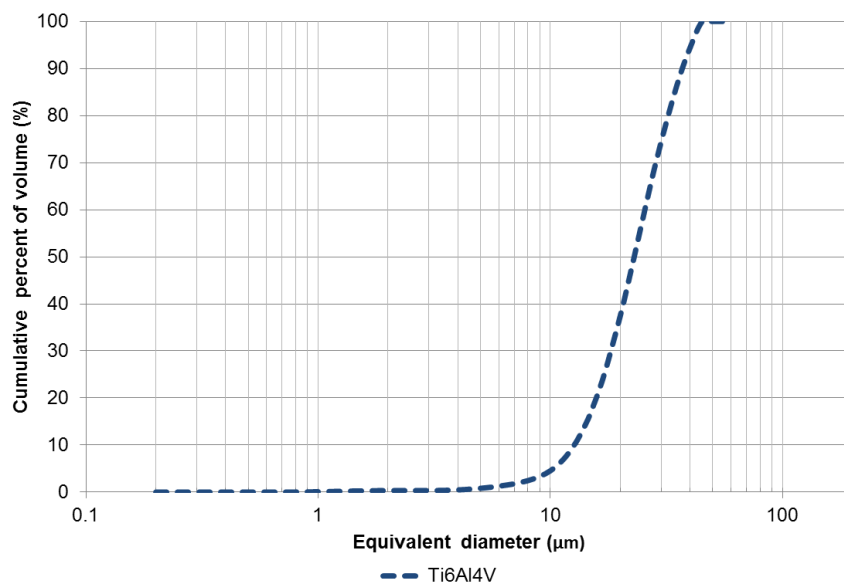
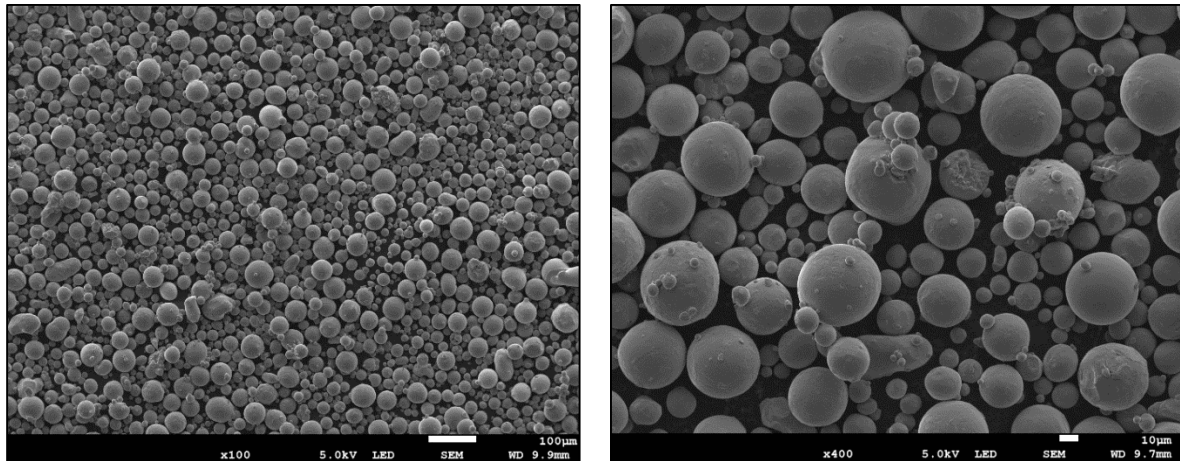


Fig. 3.2.1. Particle size distribution of employed Ti6Al4V powder. Powder particles were spherical (a), some of them had small satellites (b).

Before the experiment the powder was dried at 80°C for 2 hours. The surface of the powder particles were smooth, agglomeration of powder particles was not observed (Fig. 3.2.2).



(a)

(b)

Fig. 3.2.2. SEM photos of employed Ti6Al4V ELI powder (SE mode) with different magnification: 100x (a) and 400x (b).

3.3. Design of Specimens

Before any manufacturing could commence by AM, parts or specimens had to be designed with CAD. Primitive samples of basic shapes were designed as well as layered samples (Fig. 3.3.2). The design software incorporated in this study was Solidworks 2014 (Dassault Systemes) the 3D models (see Fig 3.3.1) were generated and then converted to STL (Stereo-lithography) file format via the Solidworks platform.

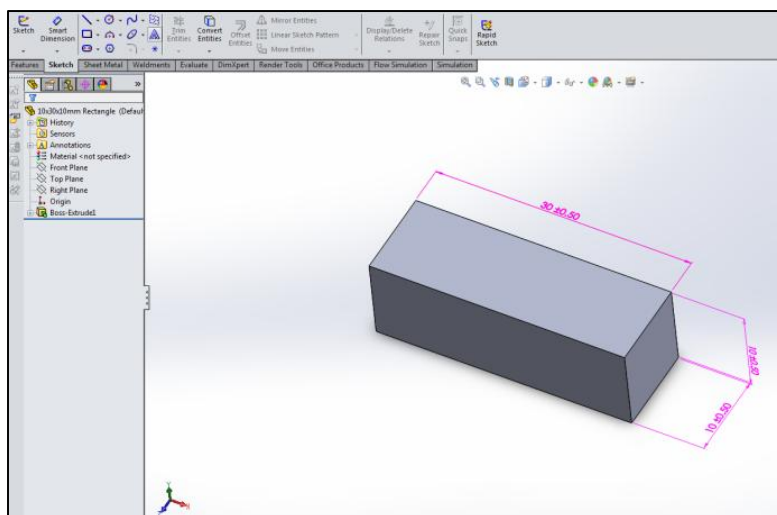
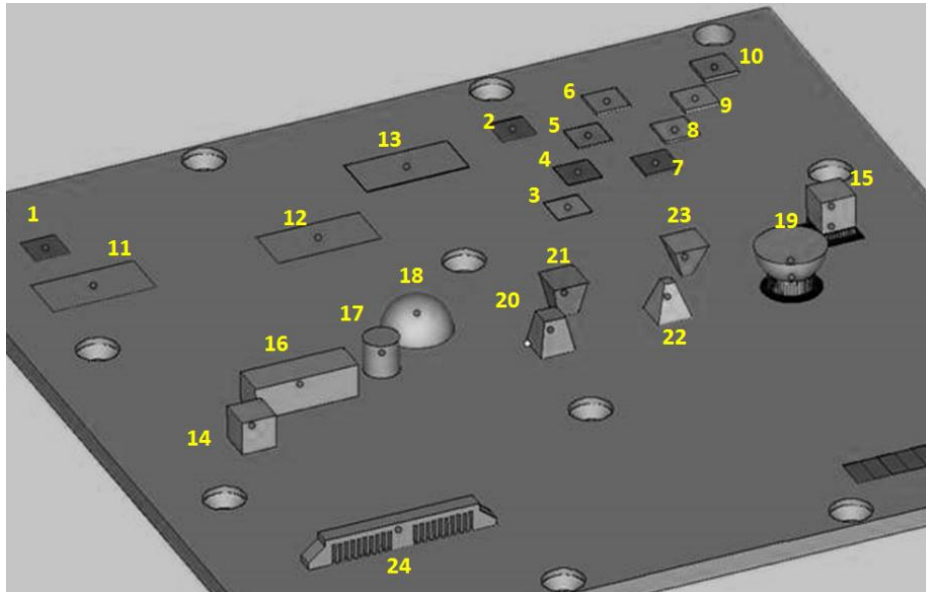


Fig. 3.3.1. Rectangular specimen (16) design interface.

The .STL files were then imported into Magics software (Materialise), which is a purpose made AM software. This software is the final step in communication to the EOSINT M280 machine, and once the parts have been placed on a virtual substrate within the software

and final additions of supports are made, processing and manufacturing can commence. Samples produced for this study is shown in Figs. 3.5.2 and 3.6.3.



Name	Nº	Description
Squares 10x10 mm ² :	1	Without powder
	2	1 layer (30 µm)
	3	5 layers
	4	10 layers
	5	15 layers
	6	20 layers
	7	25 layers
	8	30 layers
	9	35 layers
	10	40 layers
Rectangles 15x30 mm ²	11	Without powder
	12	1 layer
	13	10 layers
Cubes 10x10x10 mm ³	14	Without support
	15	With support
Parallelepiped 10x30x10 mm ³	16	
Cylinder Ø10 mm, height 10 mm	17	
Semi-sphere	18	Without support
	19	Sphere with support
Prisms	20	height 10 mm, bottom base 10 mm, top base 6 mm
	21	height 10 mm, bottom base 6 mm, top base 10 mm
	22	height 10 mm, bottom base 10 mm, top base 3 mm
	23	height 10 mm, bottom base 3 mm, top base 10 mm
Cantilever	24	

Fig. 3.3.2. DMLS specimens design.

3.4. Manufacturing of the samples by EOSINT M280 system

Ti6Al4V samples were produced by the EOSINT M280 machine (EOS GmbH.) equipped with an Ytterbium fibre laser operating at 1075 nm wavelength (IPG Photonics Corp.). The laser beam had a TEM00 Gaussian profile and 80 μm spot diameter. Powder layer thickness of 30 μm was used; the build volume rate was 1.2 mm^3/s .

A back-and-forth scanning by strips with the hatch distance of 100 μm was applied for manufacturing of specimens in accordance with standard process parameters. The substrate and powder material is similar in chemical composition. Argon was used as the protective atmosphere for the M280 machine, and because it is used solely to manufacture medical implants apart from some experimental specimens, no other powder than Ti6Al4V has been used in the metal laser sintering machine.

Preparing the M280 System for Manufacturing;

1. Clean Ti6Al4V substrate with Ethanol
2. Install substrate via all allen bolts into the M280 build chamber
3. Level the platform and substrate using the M280 interface and a feeler gauge
4. Ensure recoater blade is damage free
5. Deploy powder into hopper (Utilizing PPE at all times)
6. Compaction of powder
7. Level powder
8. Ensure recoater arm path over the substrate is collision free (clearance 0.03 mm < 0 mm)
9. Install duct in front of building chamber
10. Flood chamber with Argon until oxygen content is below 0.01%
11. The DMLS process then starts automatically via the EOS interface

The specimens that were produced were removed from the EOSINT M280 system as one part on the substrate (as-built). The substrate was then cleaned in an ultra-sonic water bath and shipped to Nelson Mandela Metropolitan University for XRD measurements.

3.5. XRD Measurements of Residual Stress

The residual stress measurements were done with an X-ray diffractometer from ProtoXRD (Fig. 3.5.1). The residual stresses were determined using the $\sin^2 \psi$ method. The lattice deformations of the Ti- α were determined using a $\text{CuK}\alpha$ radiation source. Scans were

performed around a {213} Bragg diffraction peak ($2\theta \sim 139.69^\circ$) at 9 tilting angles ψ between $-44.16^\circ + 44.16^\circ$.



Fig. 3.5.1. ProtoXRD employed by NMMU.

The residual stresses were calculated considering plane stress conditions using X-ray elastic constants shown in Table 1. The electrochemical removal technique was used to determine in-depth residual stress distribution (Struers A3 electrolyte). Principal stresses and their directions were analysed, parts were numbered and measured as shown in Fig. 3.5.2. XRD measurements were done at the Department of Mechanical Engineering of NMMU.

Table 3.5.1. Parameters used for the X-ray analysis

Test material	Collimator, mm	Wavelength, Å	Radiation	Bragg angle 2θ , °	hkl	$1/2 S_2$, MPa ⁻¹	$-S_1$, MPa ⁻¹
Ti α	3	1.5418	Cu K α	139.69	{213}	11.89×10^{-6}	2.83×10^{-6}

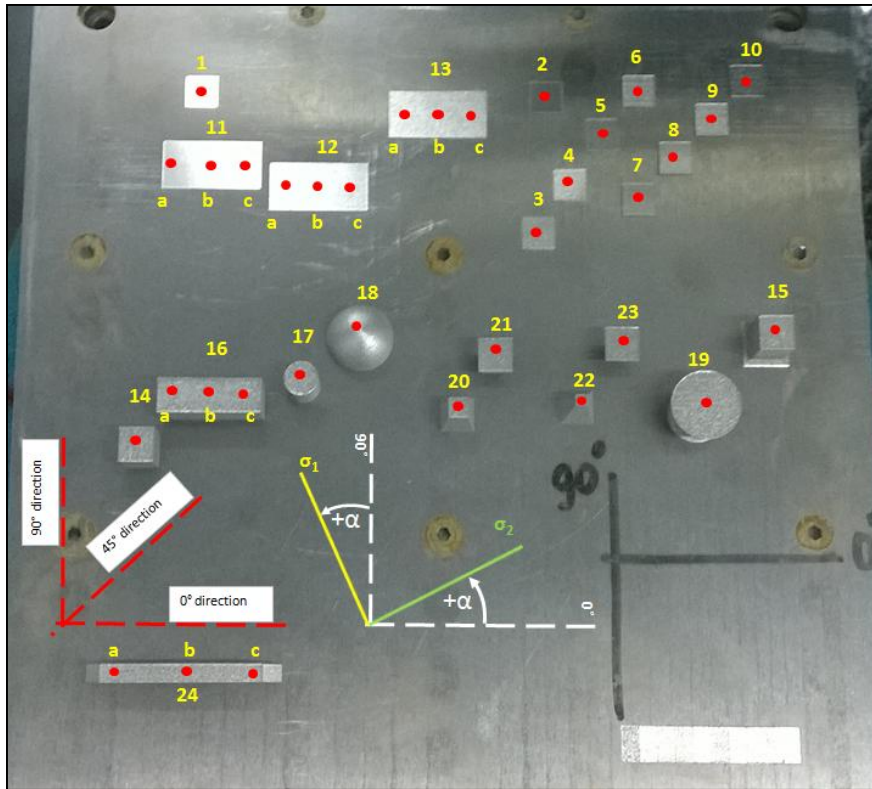


Fig. 3.5.2. Substrate with parts and identification for different points of measurements (red dots) samples.

3.6. Cantilever Curvature Method Analysis

This method involves creating a cantilever of certain geometry (Fig. 3.6.1). Cantilevers with increasing thickness was produced (Fig. 3.6.2) this would add to the height of the samples but the steps are done in such a way that it would not increase attached area of the beam, this will later be likened to a predictive model that was simulated.

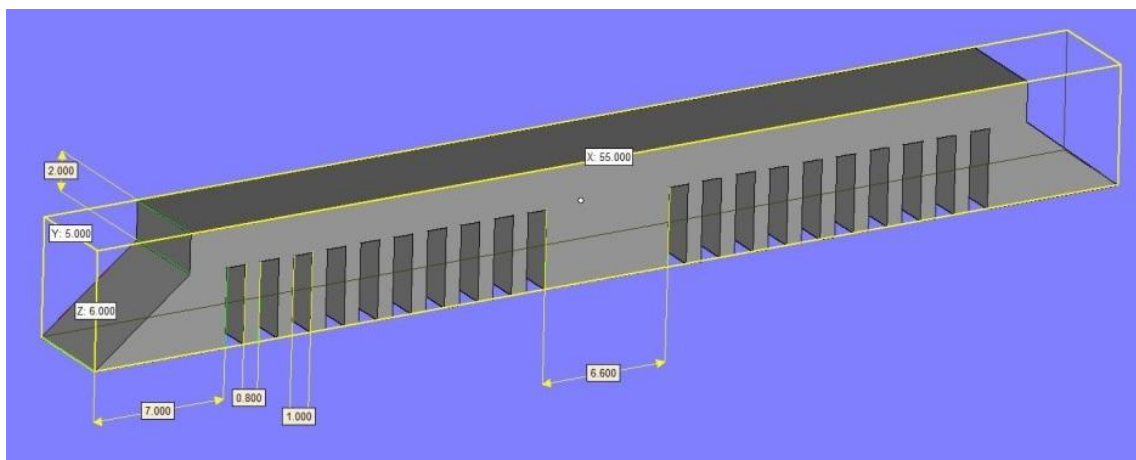
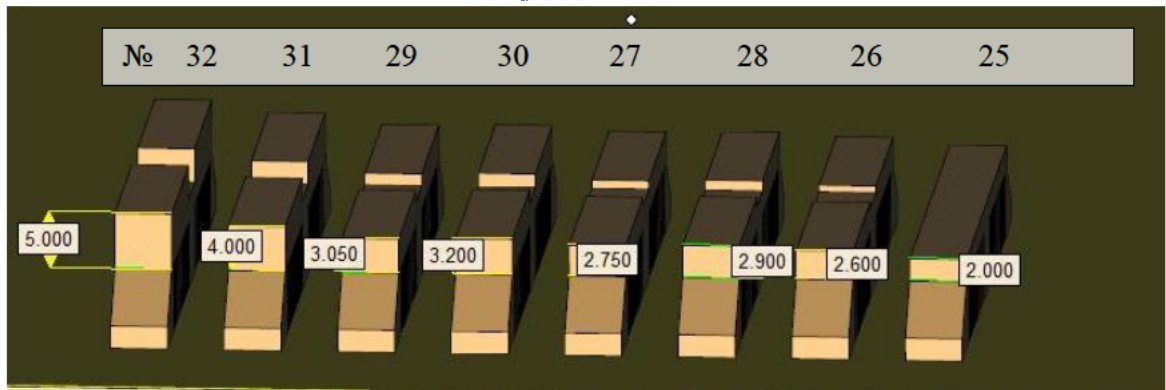


Fig. 3.6.1. Cantilever's geometry (for specimen №24).



Name	№	Thickness of the bar placed on the 2-mm beam
Cantilever	25	0 mm
	26	0.60 mm
	27	0.75 mm
	28	0.90 mm
	29	1.05 mm
	30	1.20 mm
	31	2.0 mm
	32	3.0 mm

Figure. 3.6.2. Cantilevers for curvature method (8 specimens).

Four sets of 8 cantilevers were produced (Fig. 3.6.3), the substrate consisted of the same material (Ti6Al4V) and standard process parameters were used.

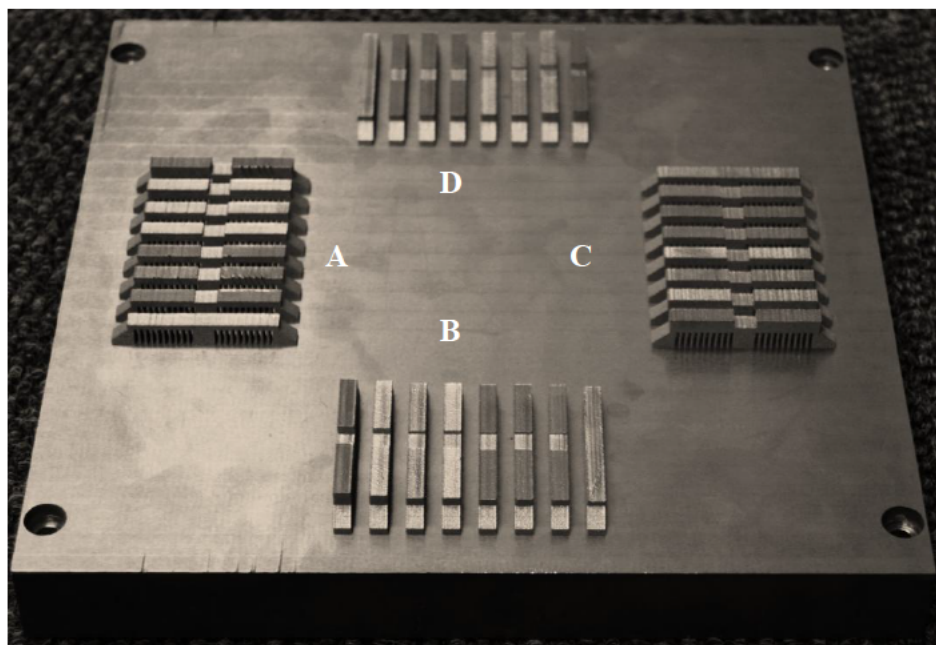


Fig. 3.6.3. DMLS Ti6Al4V (ELI) cantilevers on the base plate.

After the samples were produced, half of the cantilever was separated from the substrate via EDM. Due to the residual stress present the cantilevers deflected up at a certain

angle. This angle was then measured and correlated giving a qualitative measurement of the residual stress present. The process was as follows:

1. Design via CAD cantilevers of specific geometry
2. Feed the data into the Materialise software and position samples on the substrate as desired
3. Commence with the building process on the M280 system
4. Remove from system, and separate half the geometry from the substrate
5. Measure deflection via Kreon Ace (See section 3.8.)
6. Determine the residual stress for the samples
7. Stress relieve the cantilevers in an argon furnace
8. Separate the remaining half from the substrate
9. Take note of the deflection (no deflection expected)

3.7. Metallographic Analysis of Microstructure and Porosity

Metallographic analysis was necessary to determine as the title describes as well as the microstructure and porosity of the questioned specimens. The process for the preparation of specimens as well as the etching of alloys are described with ASTM E3 and ASTM E407.

The microstructure as well as porosity was studied by utilising a SEM. The SEM utilised was the JEOL JSM-7800F at the University of the Free State (UFS). The samples for analysis were prepared in the following order:

1. Due to the high ductility and toughness of titanium and titanium alloys they have low machinability. Consequently it can be very difficult to cut with wet abrasive cutting using the standard cut-off wheels because the edge will clog-up with abraded material. This is why wire-EDM cutting was used
2. Templates were set in resin with a Hot Mounting Press from Struers (CitoPress-1) Fig. 3.7.1 (a)
3. A grinding and polishing procedure with the Tegramin polishing machine (Fig. 3.7.1) are shown in Fig. 3.7.2
4. Samples were etched using Kroll's reagent
5. Processes were inspected via an optical and SE microscopes (Fig. 3.7.3)
6. If needed processes were repeated to ensure accuracy and clarity

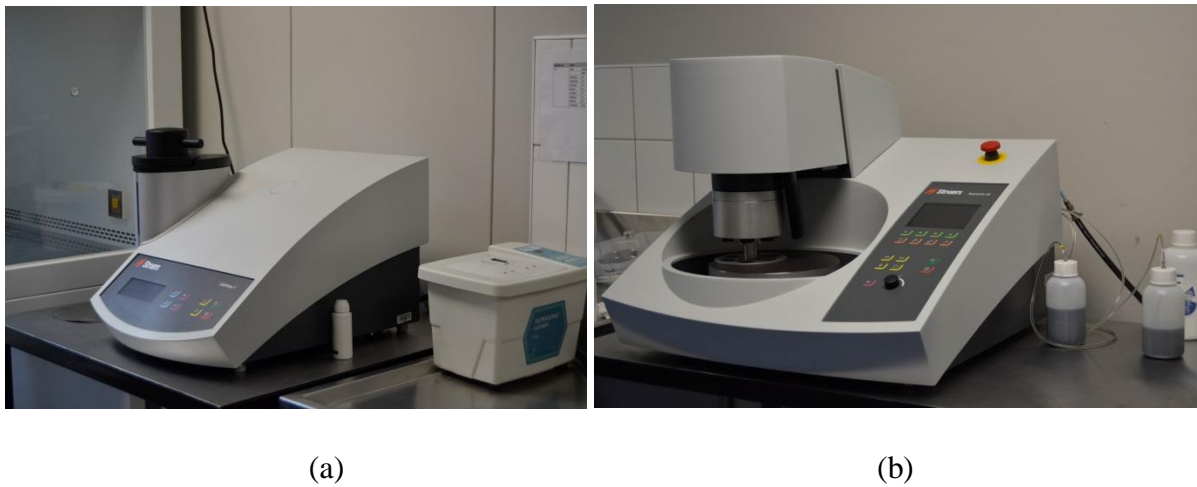


Fig. 3.7.1. Struers CitoPress-1 (a) and polishing machine Tegramin-25 (b).

Grinding				Polishing		
Step	PG 	FG 	Step	OP 		
 Surface	MD-Mezzo	MD-Largo	 Surface	MD-Chem		
 Abrasive Type Size	Diamond #220	Diamond 9 μm	 Abrasive Type Size	Colloidal Silica 0.04 μm		
 Suspension / Lubricant	Water	DiaPro Allegro/Largo	 Suspension / Lubricant	OP-S*		
 rpm	300	150	 rpm	150		
 Force [N]/specimen	40 ***	30	 Force [N]/specimen	30 per sample		
 Time (min)	Until Plane	5	 Time (min)	5 **		

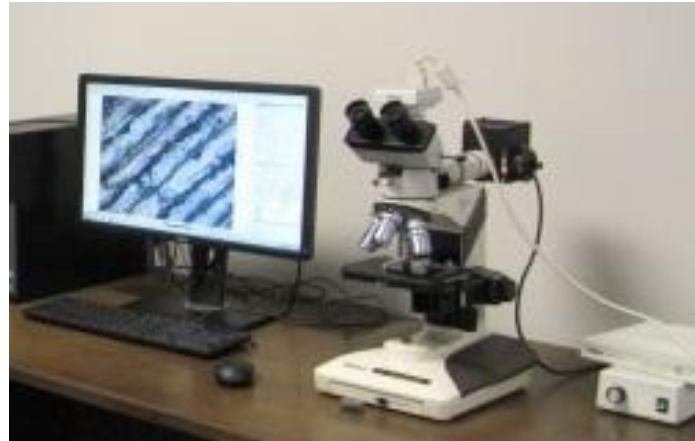
* Mix 90 ml OP-S with 10 ml H₂O₂ (30%).

** The polishing time depends on the sample area. Very large samples require more polishing time than small ones.

*** Decrease to 25 N to avoid pencil shapes in single sample preparation.

Note: during the last 10 seconds of the preparation step with OP-S, the rotating cloth is flushed with water. This will clean the samples, holder and cloth

Fig. 3.7.2. Method used for polishing titanium alloy (Struers, 2015).



(a)



(b)

Fig. 3.7.3. (a) Optical microscope (CUT) and (b) SEM (utilised at UFS).

3.8. Deformation Estimation (3D Scanning of Specimens)

The Kreon 3D Ace Arm 7-Axis is a portable coordinate measuring machine that allows the measuring of complex geometry (Fig. 3.8.1). The possibility of interchangeable scanners also allows for various analysis from single point probing to laser scanning of greater geometry. This device is mostly employed for Reverse Engineering applications. For this specific study, the device was used to scan the as-built samples, the information from the scanning device was then imported into GeoMagics. This yielded geometrical data which could then be compared to the original CAD geometry of the samples that were produce (this would give an indication of the influence of residual stress on geometry deformations but also the accuracy of the M280 system).

Step by step process for reverse engineering utilizing Kreon Ace:

1. The device was connected to the required software
2. The substrate with samples to be measured were placed on a flush flat surface
3. The scanning head (green light and red laser line) was then maneuvered over the samples that required analysis
4. Real-time software integration revealed many nodes (points of accuracy) that were picked up via the high resolution scanning.
5. The complete data was then compared with the Solidworks CAD geometry

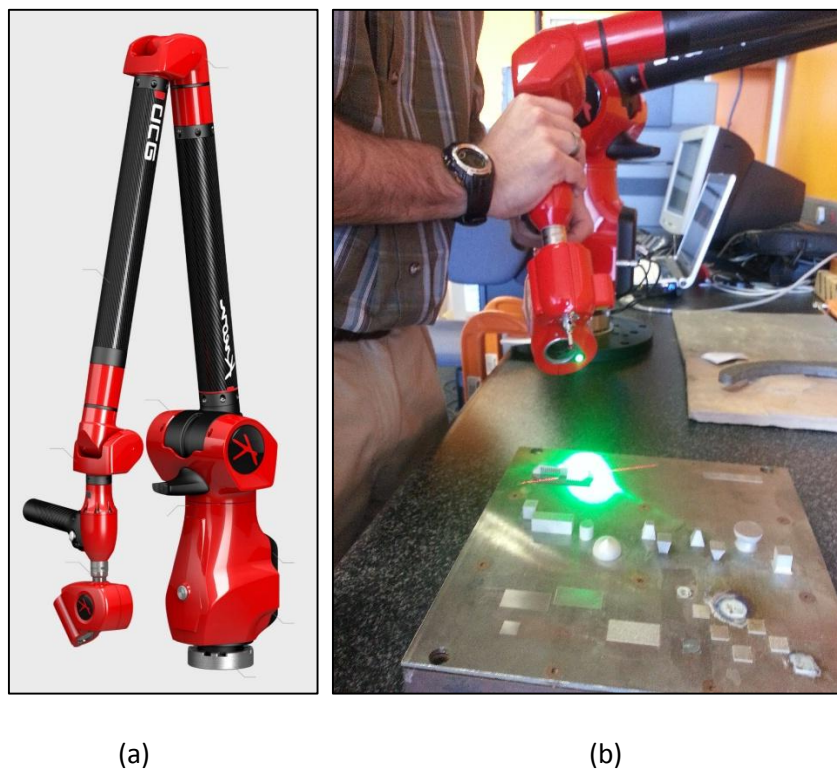


Fig. 3.8.1. Kreon Ace 7-Axis Scanner (a) and scanning of the samples (b).

3.9. Surface Roughness Testing

Surface roughness often shortened to roughness, is a component of surface texture. It is quantified by the deviations in the direction of the normal vector of a real surface from its ideal form. If these deviations are large, the surface is rough; if they are small, the surface is smooth. The surface roughness was measured by using a Mitutoyo SJ-210 which fulfils ISO 1997 requirements (Fig. 3.9.1).

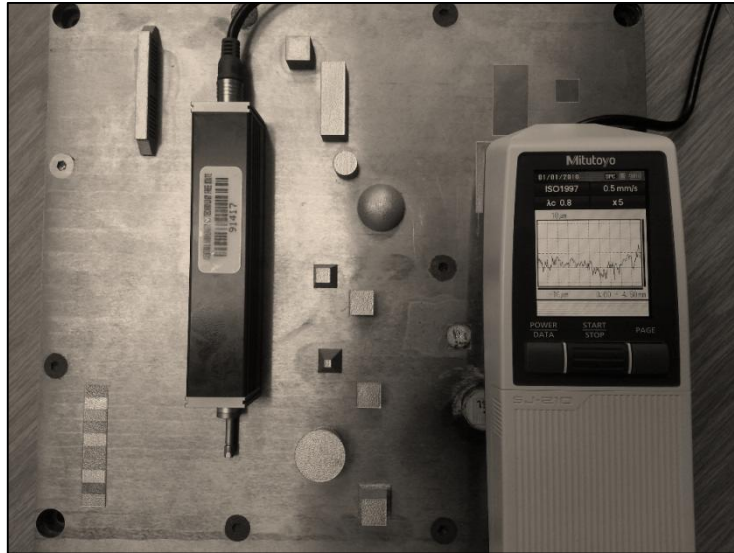


Fig. 3.9.1. Mitutoyo SJ-210 on top of substrate with samples.

The parameters used for the measurements are as follows;

- Distance of measurement 5 mm
- Speed of detector 0.5 mm/s
- Two directions of measurements 0° and 90° (Longitudinal)
- Three measurements in each direction

When measurements are made, the device has been completely stationary.

3.10. Micro-Hardness Testing

The micro-hardness as a part of the metallographic analysis was done using a FM-700 Digital Micro-hardness Tester for the Future-Tech Corporation as seen in Fig. 3.10.1. The Vickers hardness denotes to a value obtained from a test load, applied to a specimen to form an indentation on it with a square-based pyramidal diamond indenter which has face angle of 136°. The surface area of the permanent indentation found from its diagonal length, using the following equation:

$$HV = 0.102 \frac{F}{S} = 0.102 \frac{2F \sin \frac{\phi}{2}}{l^2} = 0.1891 F / l^2 \quad (\text{Equation 3.1})$$

Where, HV Vickers hardness; F test load (N), S surface area of an indentation (mm^2); l average diagonal length of an indentation (mm); ϕ face angle of the pyramidal diamond indenter (°).



Fig. 3.10.1. FM-700 microhardness tester.

3.11. Stress Relieving of Ti6Al4V parts

Stress relieving of Ti6Al4V as described by Donachie (2000) is effective in heat ranges of 480 °C to 650 °C with times ranging from 1-4 hours. Cooling rates for titanium alloys are not crucial, but uniformity of cooling is important. For titanium alloys produced by DMLS furnace cooling is acceptable and proven to be effective.

The stress relieving employed by CRPM in an Argon furnace is at 650 °C;

- The ramp up rate is 200 °C (per hour)
- The dwell time is 3 hours
- Furnace cooling is employed

The temperature during stress relieving does not exceed the β – transus of the material, no recrystallization takes place, thus no material properties are adversely effected or improved, except that the crystal structure ‘settles out’ in such a way that residual stress is eliminated.

Heat treatment to gain or change different properties in the Ti6Al4V components is done at the CSIR where they employ a vacuum furnace for recrystallization annealing at 950 °C

- The ramp up rate is 200 °C (per hour)
- The dwell time is 2 hours

- Furnace cool down rate is 4 hours

Mechanical properties of specimens have been influenced to some extent due to oxidation during the stress relieving process and will be discussed further later on in this chapter.

3.12. Oven Inert Box Design and Implementation

Stress relieving of titanium samples are done in-house at the CRPM, utilizing the aforementioned Argon furnace. Samples outside of the scope of this specific study were observed to have oxidized to some extent; a specific darker grey almost brown colour was present showing the presence of interstitial elements especially oxygen in the Argon furnace. The furnace being quite large the specific entry point of interstitial elements has not been identified as yet, though the quality of gas has been inspected and found to be satisfactory (Base 5 Argon – Afrox).

Due to the fact that the size of the samples or parts that enter the furnace are not too great, most of the space in the furnace it is not utilized. It was then proposed to design and implement a solution. A basic box structure was designed from 3CR12 type of stainless steel. The mechanical properties of this steel allows intermittent use at 750°C which is above the required standards (use for the oven), this was important due to the box needing longevity (Fig. 3.12.1).

Steps followed:

1. The furnace was measured and scrutinized for possible fittings and size
2. The box was designed using CAD software keeping in mind the limitations of the furnace
3. Manufacture drawings of parts and files for laser cutting were prepared
4. The production was outsourced to UFS
5. The final product was received
6. Installation of the box commenced with the purchasing of fittings and stainless steel tube
7. The box was finally set in place
8. Medical implant with test specimens was stress relieved
9. Oxidation afterwards seemed to be much lower
10. Ductility results confirmed the success of the box

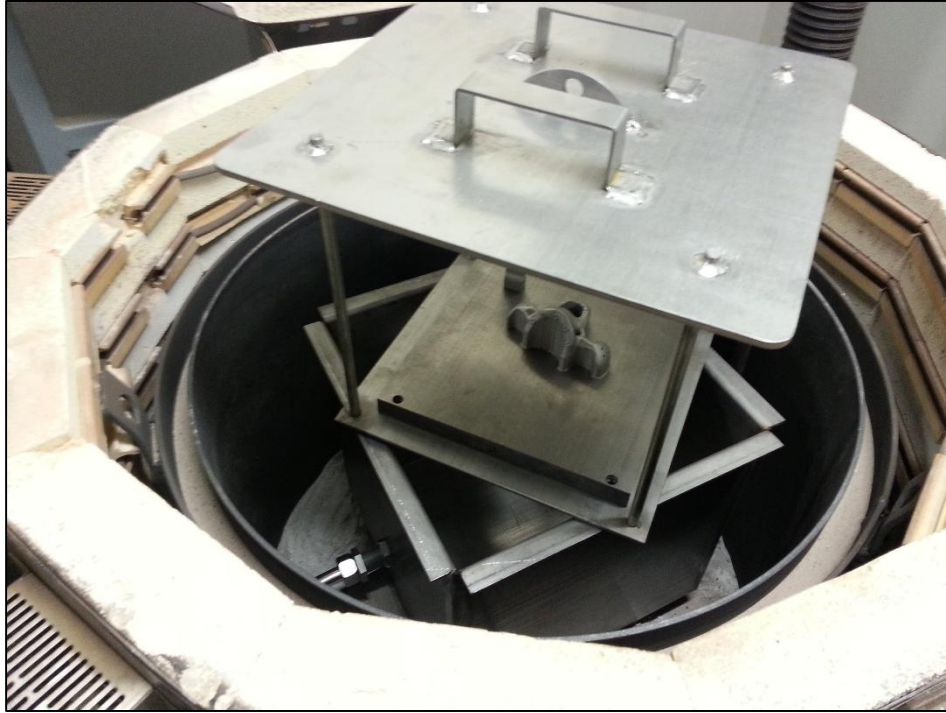


Fig. 3.12.1. Oven inert box.

3.13. Simulation of the Heat Transfer for DMLS

To estimate the temperature fields during DMLS, numerical simulations were conducted. In order to obtain accurate results, the density of the mesh in the region around the irradiation, and on the top region of the sample (100 μm), was higher than in the sample as a whole, the minimal mesh size was 0.1 μm . The laser beam with Gaussian profile scans along the X - axis at the surface of the solid sample. The evolution of the temperature due to heat conduction is

$$\rho c_p \frac{\partial T}{\partial t} - \nabla(k\nabla T) = P(1 - R) \frac{A_z}{\pi r_0^2} e^{-\frac{(x-Vt)^2 + y^2}{r_0^2}} e^{-A_z z} \quad (\text{Equation 3.2})$$

T is the temperature, t is the time, ρ is the density of material, c_p is the specific heat capacity, k is the thermal conductivity, P is the laser power; R is the surface reflectivity of material for given wavelength; A_z is coefficient of absorption; r_0 is the characteristic radius of the laser beam; x, y, z are dimensional values and V is the laser scanning speed. Equation (3.2) takes into consideration only the effect of conduction into the solid (Sanders, 1984).

All properties of material were temperature-dependent. Temperature-dependent specific heat capacity was selected with respect to latent heat of fusion $H_f=290$ kJ/kgK

$$c_p = \begin{cases} 556.2 \times \exp(0.0002T) & \text{for } T > T_m \\ c_p + H_f / (T_{liquidus} - T_{solidus}) & \text{for } T_{solidus} < T < T_{liquidus} \\ 1126 & \text{for } T \geq T_m \end{cases} \quad (\text{Equation 3.3})$$

where T_m is melting temperature, H_f is latent heat of fusion, $T_{solidus}=1877$ K, $T_{liquidus}=1923$ K.

The effect called surface-tension-driven convection or thermocapillary (Marangoni) flow, is a phenomenon whereby movement of a liquid occurs due to a local difference in the surface tension of the liquid. In general, surface tension depends on both the temperature and chemical composition at the interface; consequently, Marangoni flows may be generated by gradients in either temperature or chemical additives (Davis, 1987; Edwards *et al.*, 1991; Sternling *et al.*, 1959; Limmaneevichitr & Kou, 2000). In the liquid molten pool Marangoni flow contributes significantly to temperature distribution and shape of the pool because this flow serves as the heat transfer way transporting energy from the laser beam. Effect on heat exchange by thermocapillary driven flow can be approximated by an equivalent thermal conductivity. As a result of this assumption, the temperature distribution can be determined by a pseudoconduction model (Pan & Lin, 1989). To simulate metal welding, effective thermal conductivity of the liquid metal has been introduced by Kim *et al.* 2003, Zhang *et al.* 2004 and He *et al.*, 2003. For Ti6Al4V alloy the effective thermal conductivity of the liquid metal was introduced as value multiplied by a factor of 1.5-3 taking into account heat transfer due to flows. Except for the top surface, all other boundaries are assumed to be thermally insulated. The heat flux on the top surface simulates convective cooling. Heat losses due to convection is expressed by $q_c = h_c(T - T_o)$, where $T_o = 293$ K is initial temperature, $h_c = 10$ W/(m²K) is convection coefficient.

To validate the model, the actual experimental true temperatures from Yadroitsev *et al.* (2014) were used as input for the simulation. A back-and-forth scanning by strips with the hatch distance of 100 μm is applied by the M280 machine for manufacturing of the Ti6Al4V specimens. Four scan lines were simulated; 3D numerical simulation of SLM was carried out using Comsol 5.1 software (Comsol, Inc.). Numerical simulations of the temperature fields and stresses have been conducted on the basis of the models developed by Dr. I. Yadroitsava.

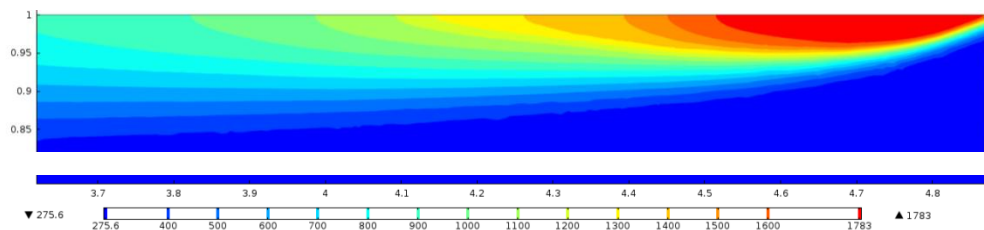
3.14. Summary

A general methodology flow diagram for this study was presented in this chapter. A material characterization of Ti6Al4V ELI powder was done. The powder supplied by TLS Technik was used in all test samples produced by the EOSINT M280 for this study. The design of specimens were done with Solidworks a CAD interface, samples were placed in a simulated chamber via the Magics interface (communicating directly with the M280) and were produced by DMLS via the EOSINT M280. XRD measurements of residual stress were done at NMMU on a ProtoXRD platform in Port Elizabeth by S. Grewar, Senior Project Engineer and specialist in the field of residual stress measurement via HDM and XRD. Cantilever Curvature Method was used to confirm or disprove XRD results. Deformation of samples was analyzed using the Kreon-Arm as well as DesignX software (from Geomagics). Surface roughness characterization was done for samples produced for this study. An inert box was designed, built and installed in the argon furnace and stress relieving of the DMLS pieces was done. Numerical simulation of the DMLS process for the prediction of residual stress was done via COMSOL Software.

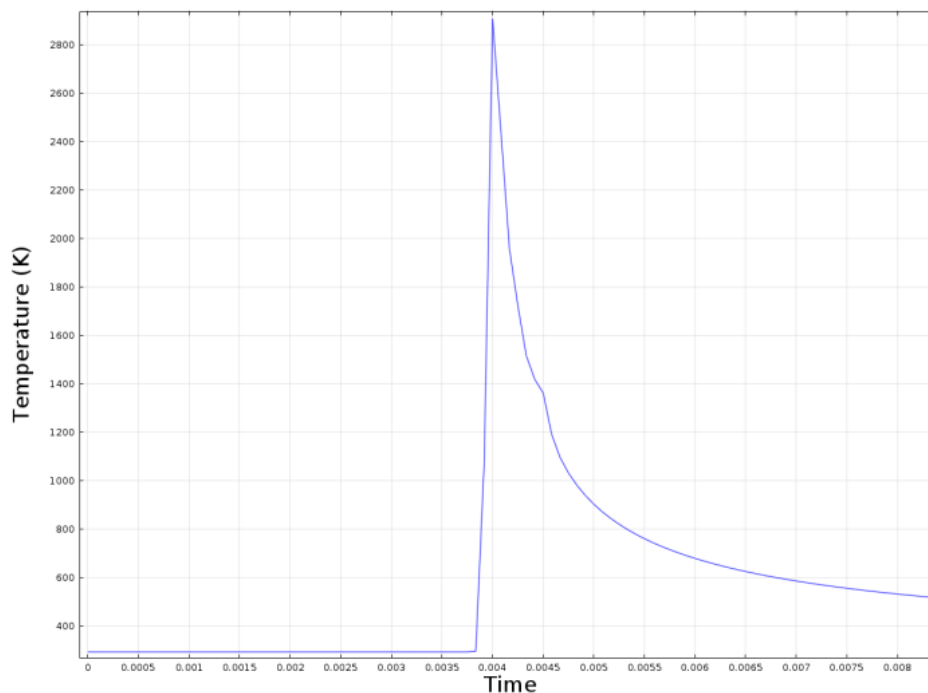
Chapter 4: Results and Discussion

4.1. Temperature evaluation and microstructure of Ti6Al4V DMLS samples

Numerical simulations showed that, at laser power of 150 W, spot size of 100 μm (laser power density is 19.1 kW/mm^2) and scanning speed of 1.2 m/s, the maximum temperature during the laser melting of Ti6Al4V alloy was approximately 3000 K. The heat-affected zone and the molten pool had an elongated shape in the scanning direction (Fig. 4.1.1).



(a)

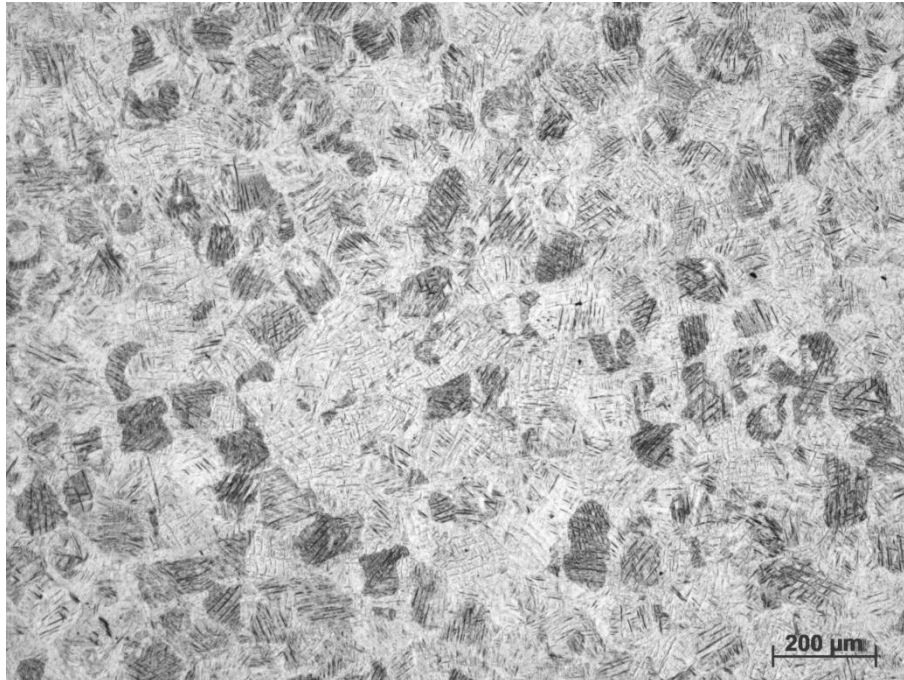


(b)

Fig. 4.1.1. Temperature gradient for cross-section of the track along scanning direction at $t=0.004$ s (a) and temperature profile for point at the top surface $x=4.8$ mm during laser scanning of the Ti6Al4V sample with the length of 1 cm, the laser power density of 19.1 kW/mm^2 and the scanning speed of 1.2 m/s.

Fig. 4.1.2 (c) shows optical microscope photos of etched cross-sections in the different planes of the sample (xyz 35mm \times 5mm \times 20mm) built in z direction. An observed martensitic microstructure is typical for Ti6Al4V samples manufactured by DMLS. In (xz) and (yz) planes columnar growth is observed, in the transverse direction (xy) bundles of columnar grains are seen. The microstructure of the DMLS samples differ from the microstructure of wrought Ti6Al4V alloy since the cooling rates during DMLS reach 10^5 – 10^6 K/s (Fig 4.1.4). The as-built DMLS microstructure of Ti6Al4V (ELI) shown in Fig. 4.1.3 has a very fine, acicular morphology. Scrupulous analysis of different cross-sections showed that maximum size of a pore that was discovered was about 50 μm , but such anomalies were rare; typical pore size was less than 20 μm (Appendix 1).

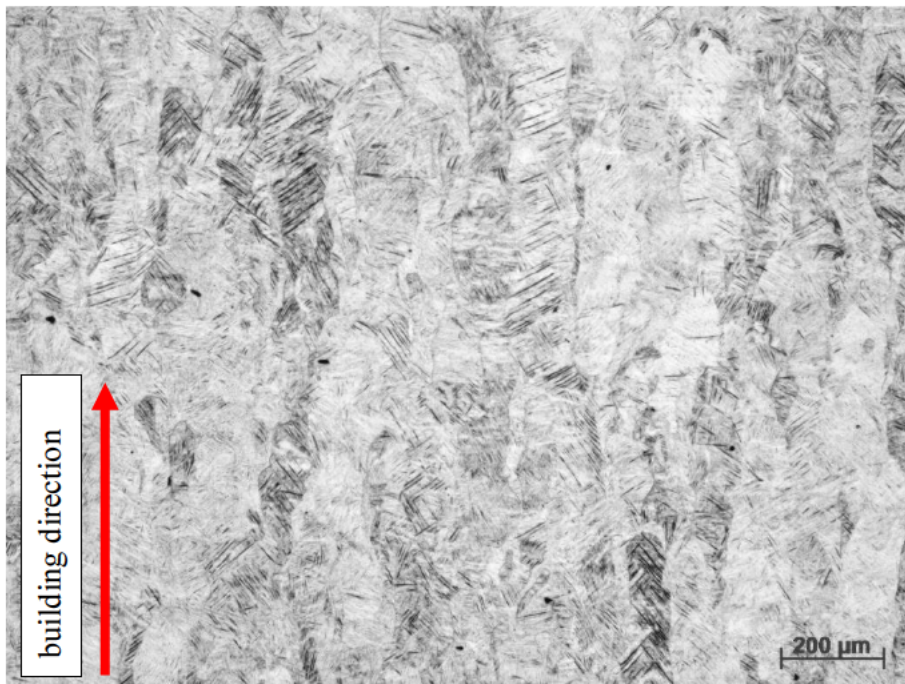
The DMLS microstructure is a result of rapid solidification and its features correlate with the heat conducting direction. During DMLS, sintered material is subjected to cycling heating/cooling (Fig 4.1.4). DMLS promotes the formation of an acicular/lamellar α' hcp phase (martensitic), which has a finer microstructure and exhibits larger residual stresses, but it is inherently less ductile than the globular microstructure formed during conventional processing (Kasperovich & Hausmann, 2015).



(a)



(b)



(c)

Fig. 4.1.2. Microstructure of the as-built Ti6Al4V (ELI) sample at different cross-sections: xy (a), yz (b) and xz (c) planes.

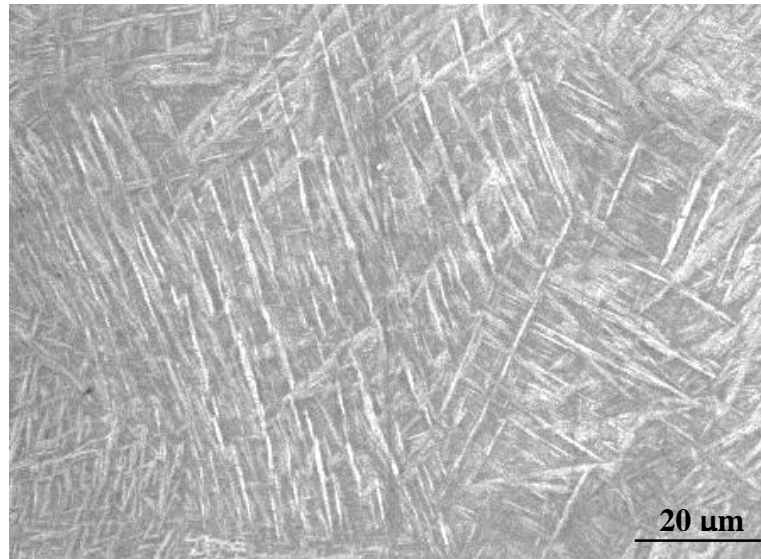


Fig. 4.1.3. SEM image of the martensitic microstructure of as-built Ti6Al4V (ELI) sample.

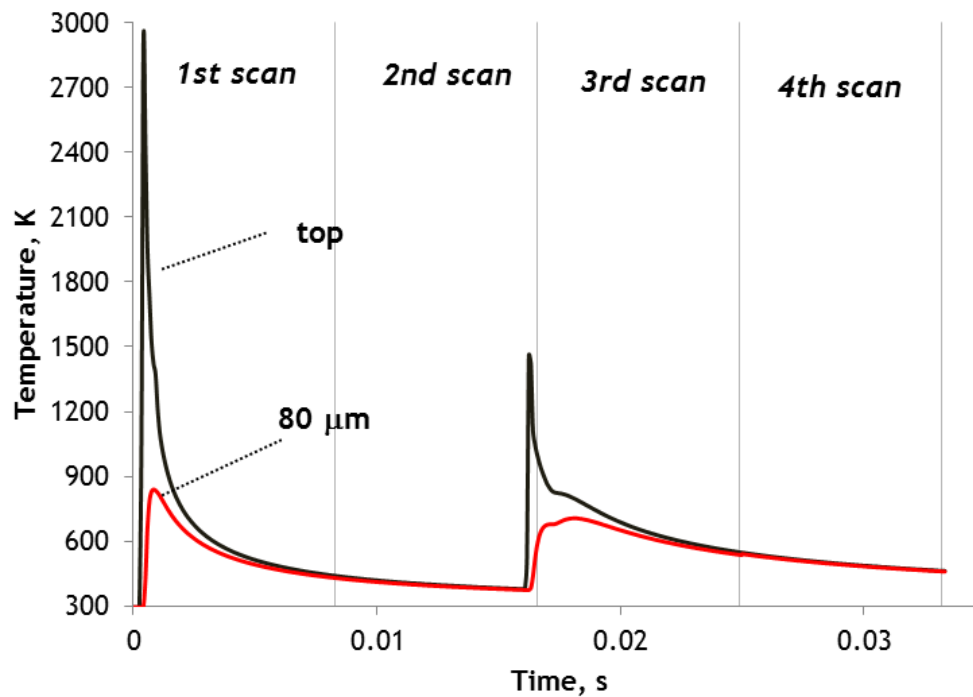


Fig. 4.1.4. Temperature profiles (point $x=0.5$ mm, depth $z=0$ and $80\ \mu\text{m}$) during back-and-forth laser scanning of the Ti6Al4V sample with length of 1 cm, laser power density of $19.1\ \text{kW}/\text{mm}^2$ and scanning speed of 1.2 m/s.

The microstructure achieved by DMLS of Ti6Al4V is a martensitic microstructure alpha-prime or acicular alpha denoted α' , as indicated Rafi *et al.* (2013), Cain *et al.* (2015) (Fig. 4.1.5). Microstructure and mechanical properties of as-built DMLS objects depend on not only temperature-dependent material properties, but also process-parameters such as laser power density, scanning speed, powder layer thickness, scanning strategy, preheating and building strategies (Klocke *et al.*, 2003; Yadroitsev, 2009).

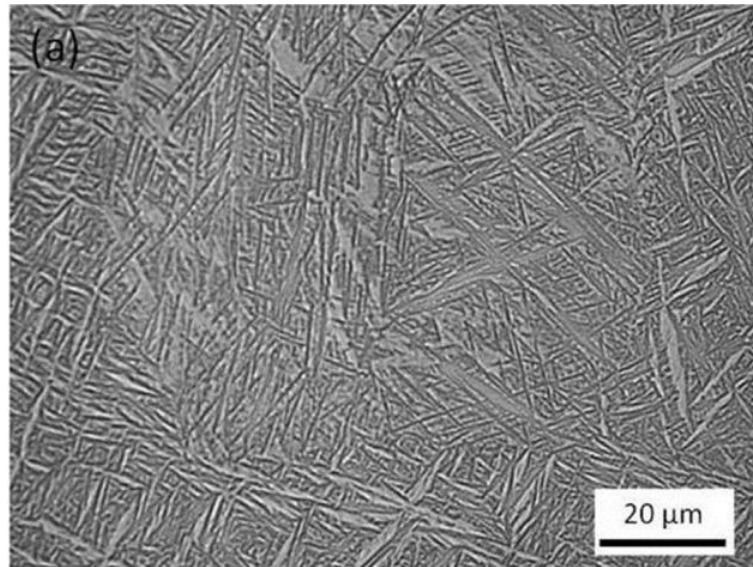


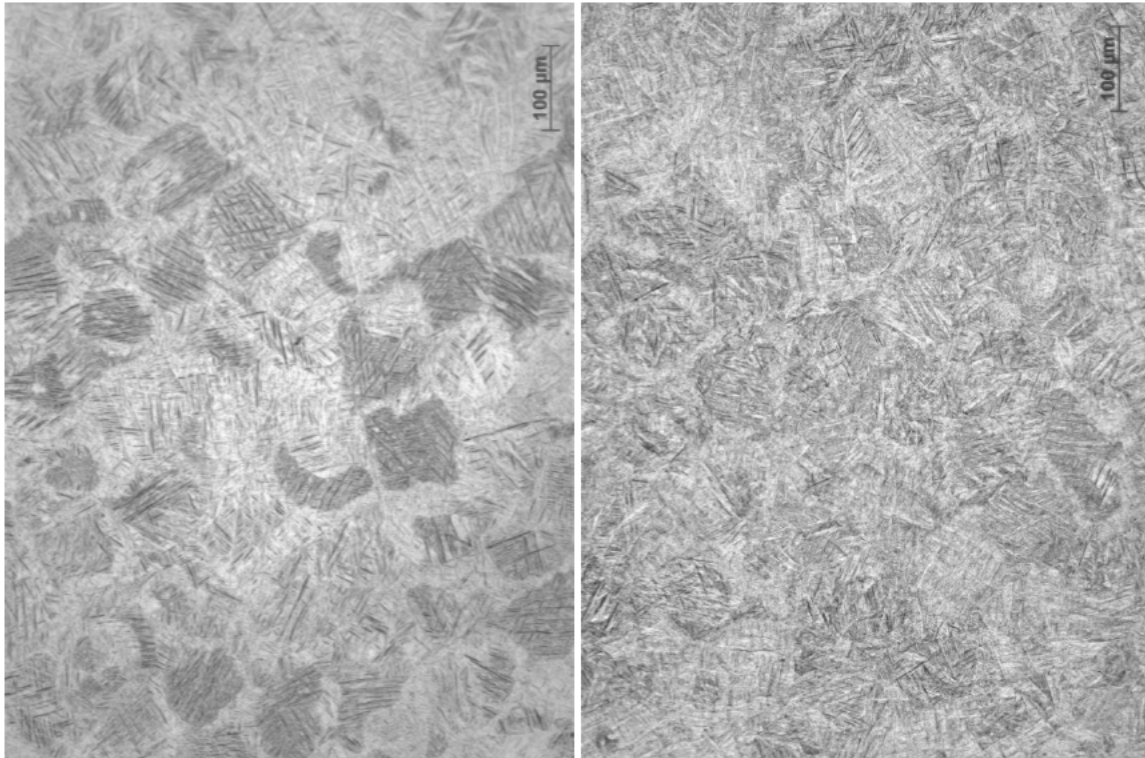
Fig. 4.1.5. Martensitic microstructure of as-built Ti6Al4V (Cain *et al.*, 2015).

As expected from literature, martensitic crystal structure in the as-built DMLS samples is characterized by fine needles. There is very little β phase present in the as-built state or even only α' phase.

After stress-relieving at 650 °C during 3 hours in Ar atmosphere the microstructure of Ti6Al4V samples didn't change (Fig 4.1.6). Cain *et al.* (2015) by SEM found a small change from fine alpha plates to a coarser acicular structure after stress relieving (Fig. 4.1.7); stress relieving was also done at 650 °C.

Another speculative estimate would be that differences in chemical composition and manufacturing process parameters may lead to different crystal structure properties as the martensitic breakdown may take place at lower or higher temperatures (Fig 3.1.6). The martensitic structure breaks down at 575°C (Ahmed & Rack, 1998) but according to Xu *et al.* (2014), this breakdown can occur at temperatures as low as 400°C.

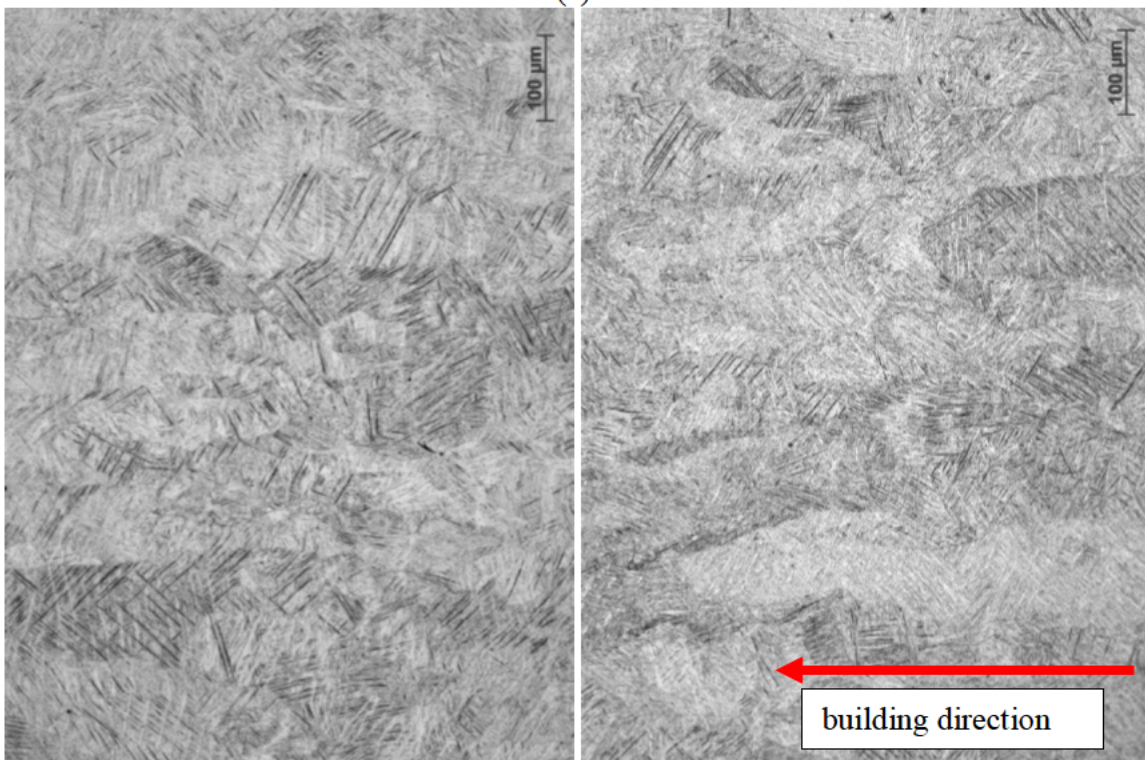
A martensitic α' structure is a needle type structure giving good mechanical properties in terms of Yield strength and UTS, but low ductility or tensile elongation, to qualify for critical structure application this value should be above 10% (Xu *et al.*, 2014). With successful stress relieving, ductility is regained. This unfortunately increases the time from manufacturing of the component to its application, other solutions are required. In-situ solutions would be beneficial especially if this does not add additional time in processing.



as-built

stress-relieved

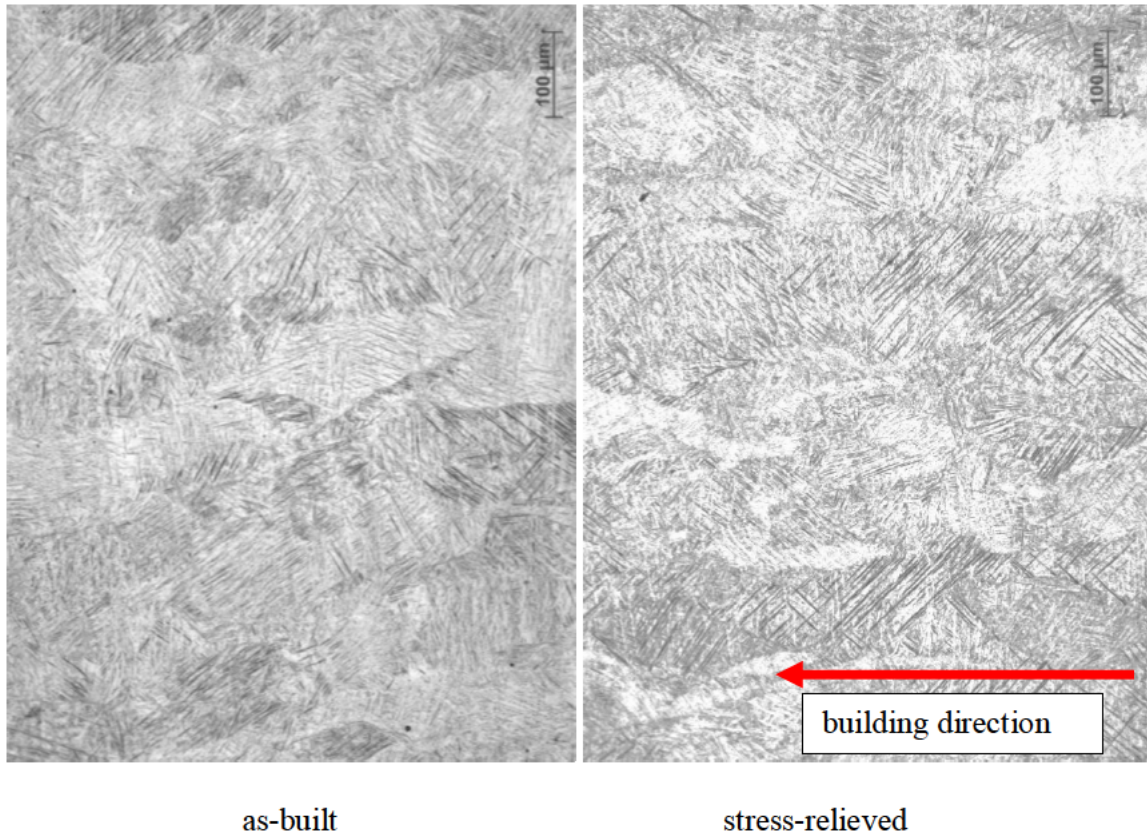
(a)



as-built

stress-relieved

(b)



(c)
Fig. 4.1.6 Microstructure of the as-built and stress relieved Ti6Al4V (ELI) sample in different planes: xy (a), zx (b), zy (c).

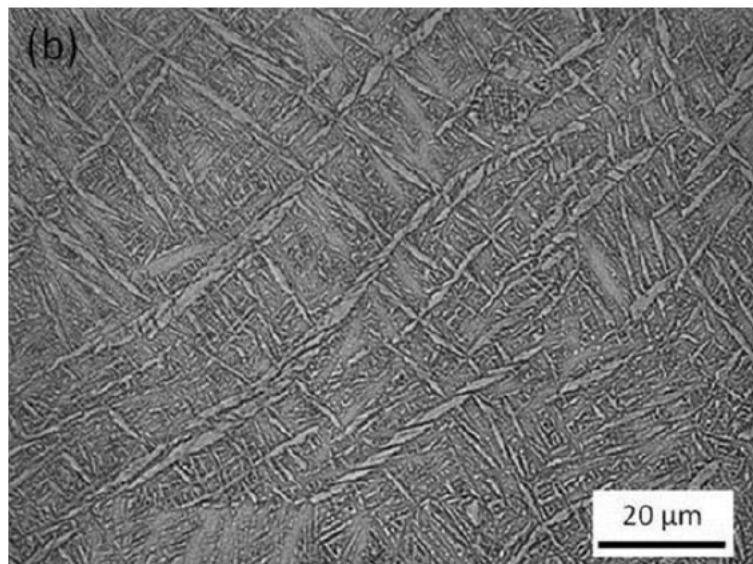


Fig. 4.1.7. Microstructure of stress relieved Ti6Al4V sample (Cain *et al.*, 2015).

4.2. Principal residual stresses measured by XRD

Table 4.2.1 and Fig 4.2.1 show the principal stresses near the surface of the samples (points indicated in Fig. 3.5.2) which were produced on the EOSINT M280 system using standard process parameters. Normal stresses are shown in Appendix 2. Due to the aperture being 3 mm in diameter, sample №22 could not be measured by the XRD system which was employed, results from an area smaller than the aperture will be inaccurate and difficult to obtain.

Table 4.2.1. Principle Stresses via XRD

Sample No.	σ_I (MPa)	σ_{II} (MPa)
1	576	240
2	615	224
3	705	413
4	777	83
5	572	334
6	824	352
7	582	316
8	826	275
9	472	392
10	688	417
11a	452	128
11b	480	164
11c	542	135
12a	456	70
12b	448	129
12c	510	127
13a	433	230
13b	463	290
13c	751	472
14	662	434
15	582	279
16a	625	320
16b	688	261
16c	509	120
17	547	148
18	316	191
19	643	381
20	578	262
21	628	377
22		
23	915	237
24a	1024	377
24b	622	558
24c	786	163

From the table 4.2.1 it is clear that the maximum residual stresses were in sample №24 (cantilever). In Fig 4.2.1 one cannot see a distinctive linear relation of residual stress, coinciding with the literature that indicated that residual stress in DMLS has an inherent anisotropic nature. The following observations were made:

- Sample №1 and №11 were done without powder, the substrate which is of the same material Ti6Al4V was exposed to the laser beam, melting and solidification occurred leading to residual stress, though low in comparison to the rest of the samples.
- Sample №15 delaminated from the supports, resulting in a lower residual stress, as the part yielded (crystal lattice relaxation).
- Sample №16 delaminated from the substrate at position C hence a lower magnitude of residual stress resulted.

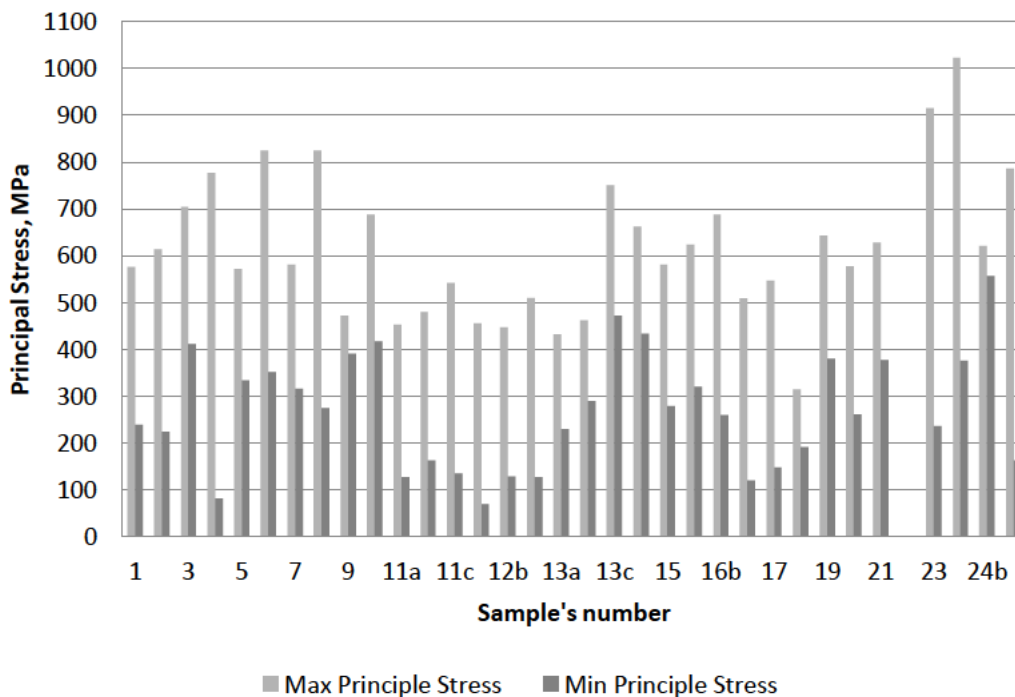


Fig. 4.2.1 Principle residual stresses for each Ti6Al4V (ELI) sample produced by DMLS.

4.2.1. Residual stress in the samples with successively increasing thickness

Samples №1–10 adhered to the substrate, values of residual stresses near the surface measured in the central point, varied significantly with the height (from 470–825 MPa for first principal stress and 225–420 MPa for the second principal stress, Fig. 4.2.2). The first principal stresses near the surface were also practically coaxial with the scanning direction (Fig 4.2.3). Yadroitsava *et al.* (2015) studied residual stress near the surface in Ti6Al4V

DMLS 1–46 layers step samples (size of step samples were chosen to receive only one strip i.e. 5 mm in width, 10 mm length, layer thickness 30 μm). It was found that tensile stress increased with the number of layers, first principle stress varied from 500 to 700 MPa.

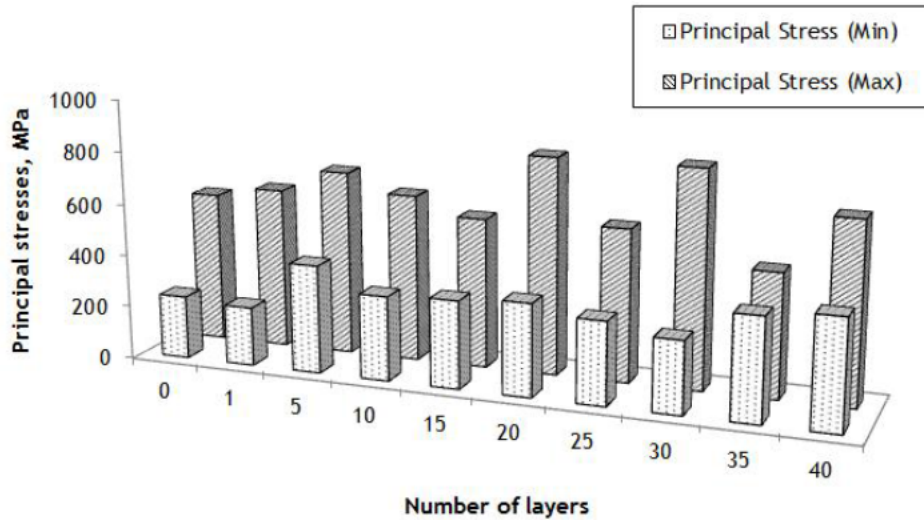


Fig. 4.2.2. Principal stresses near the surface in 10 x 10 mm square Ti6Al4V samples with 0–40 layers in height. Powder layer thickness is 30 μm .

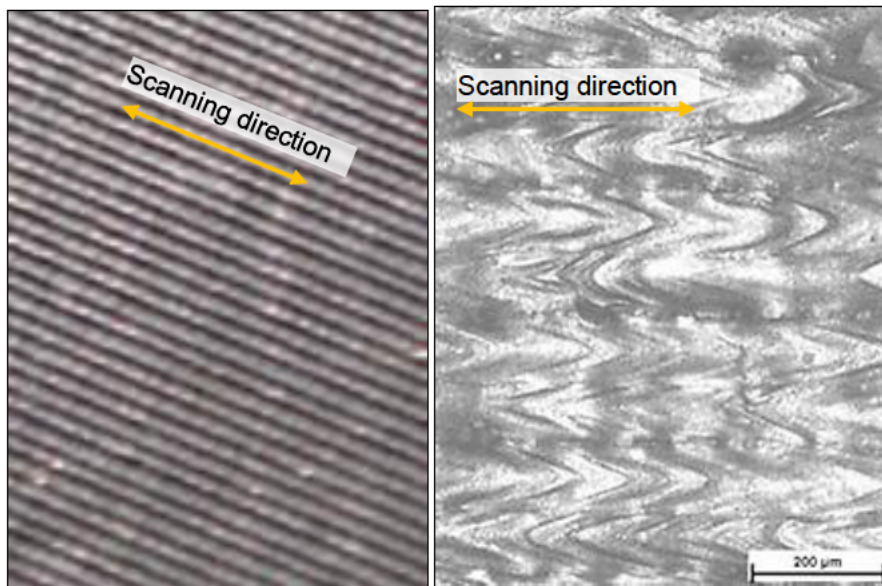


Fig. 4.2.3. Residual stresses are coaxial with the scanning direction of the top layer of the DMLS samples.

The strain during cooling can be described as a superposition of elastic, thermal and plastic properties, as well as a creep strain component. When the laser beam leaves the irradiated zone, the track begins to solidify and to cool down. Various layers of material, cool at different rates, therefore contraction also occurs at different speeds. During laser melting, high compressive and tensile stresses are present under the front of the molten pool

(Yadroitsava *et al.*, 2015; Yadroitsev *et al.*, 2015). As a result, deformations in the surrounding material and the solidifying track occur.

Laser scanning of the Ti6Al4V substrate led to similar residual stresses near the surface at 5 mm from the edges and in the middle point of the rectangle (Fig.4.2.4). First principal stresses were along the scanning direction (450–540 MPa), and second principal stresses (in a perpendicular direction) were 130–160 MPa. In the one-layer sample stresses in scanning direction for 3 points were 450-460 MPa, but stresses in perpendicular to the scanning direction varied considerably and were 70–290 MPa. The reason can be due to the inhomogeneity of delivered powder layer which led to different thermal and mechanical strains during cooling. Deformations and loss of the metallurgical contact with the substrate during manufacturing led to accumulation of heat; redistribution of stresses occurred. Possibly these phenomena were the reason for a significant difference of stresses at points 1-2 and 3 in 10-layers sample (Yadroitsava &Yadroitsev, 2015).

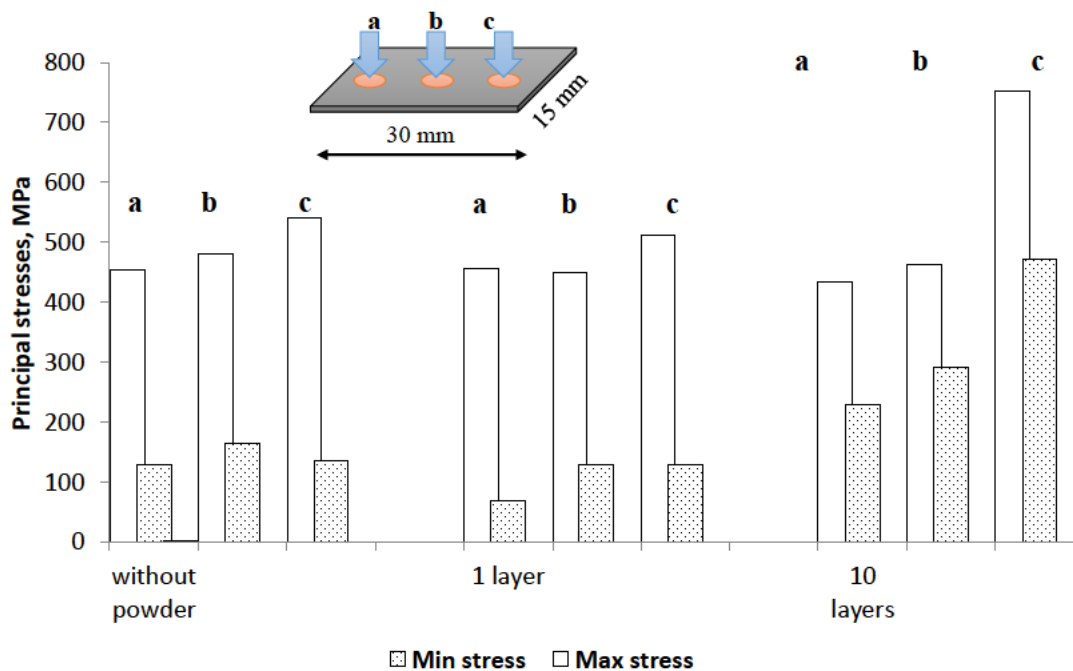


Fig. 4.2.4. XRD data for residual stress in cantilever near the surface.

The most AM methods usually do not have quality surface finishing directly after the process. Post process polishing is done to smooth surfaces. Surface roughness may influence XRD measurements, as XRD only penetrates 10-15 μm into the exposed surface. If the surface roughness is high and the finish inconsistent, it may lead to discrepancies in the XRD results. DMLS has better surface quality than most AM methods but usually still requires

polishing. The results from the surface roughness measurement are shown in Appendix 3. From the results, it is shown that the roughness values were quite low, and it will be safe to conclude that the surface finish of the as-built DMLS samples did not have an adverse effect on the XRD residual stress measurements.

The direction of the maximum principal stress coincided with the direction of the laser scanning of each of the top layers. It was found, that the average maximum height of profile R_z correlated with second principal stress, which is perpendicular to the scanning direction. Coefficient of correlation was of -0.8479 (Fig 4.2.5).

As Li *et al.* (1995) indicated there are two principal reasons for the surface roughness influencing the XRD stress determination:

- the stress distribution on the specimen surface (at rough surface, there would be a stress relaxation in the crest zone and a stress concentration in the hollow zone);
- X-ray diffraction geometry effects (surface curvature, ratio of surface size and irradiation beam diameter, shadow effect, integration effect and surface inclination effect).

For steel samples it was shown that if surface roughness more than the X-ray beam penetration depth ($10\ \mu\text{m}$), the roughness effects on stress determination by X-ray diffraction became more prominent: only the information coming from crest zone is taken account where an important stress relaxation effect is observed comparing with the imposed stress (Li *et al.* 1995).

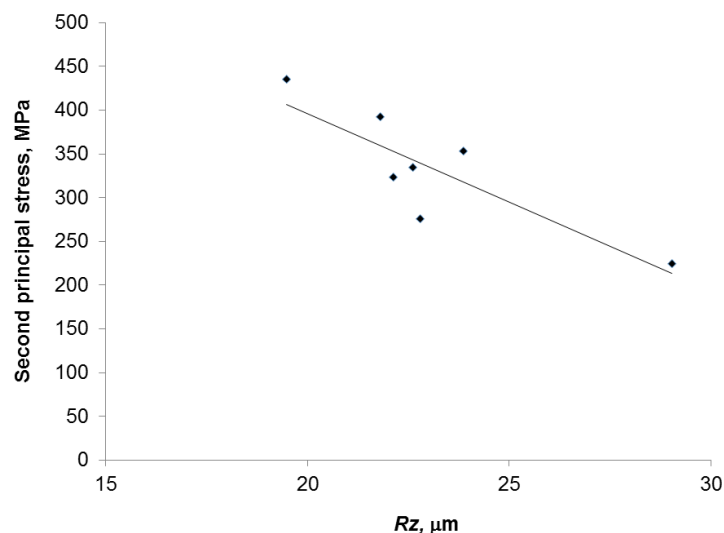
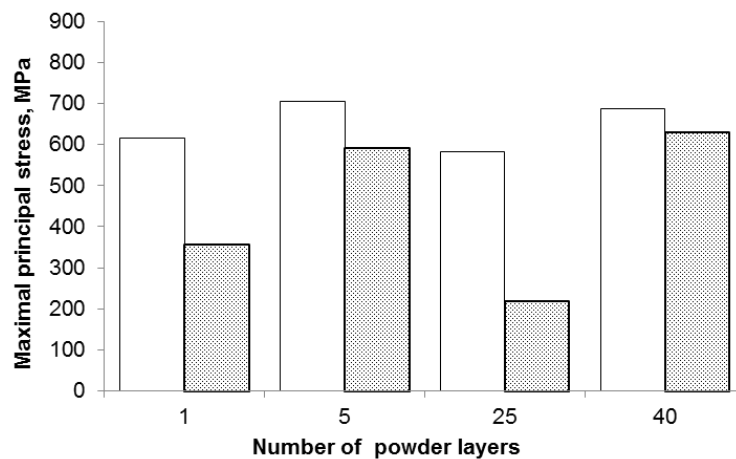


Fig. 4.2.5. Second principal stress near DMLS surface *versus* R_z .

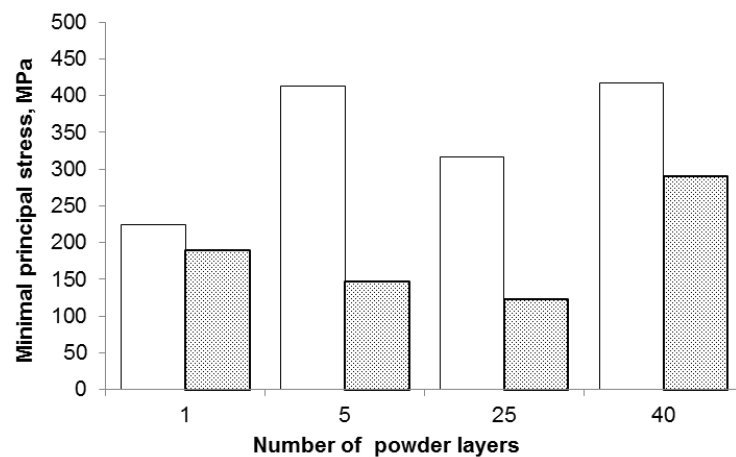
In present work, electrochemical removing of $15\text{--}80\ \mu\text{m}$ was used to determine residual stresses of the samples consisting of 1, 5, 25 and 40 layers. Results are shown in

Fig. 4.2.6. After electrochemical removal of top layers, measured principal residual stresses were 630–150 MPa, which is lower than those measured near the surface. It is very difficult to separate those different kinds of influence on residual stress. The reason also can be in-situ heat treatment taking place during scanning of the upper layers. As it was calculated for used process-parameters, at depth of 80 μm the temperature reaches about 840 K which is close to stress-relieving temperature 750-920 K. Also, the M280 machine applied different process-parameters and scanning strategy for top and inner layers. Different energy input can lead to different residual stresses.

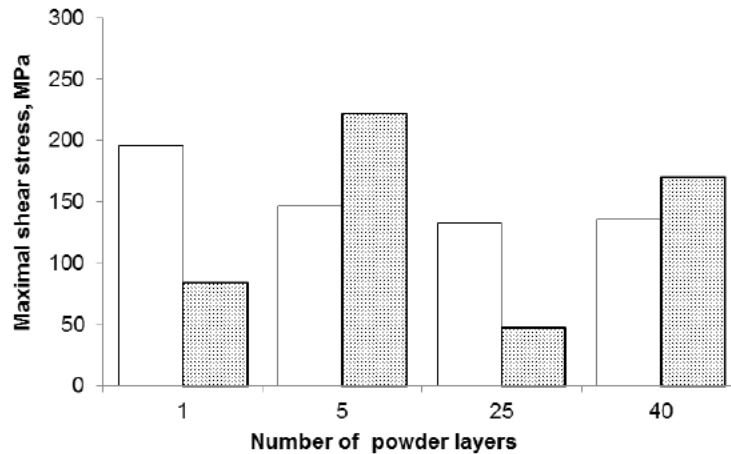
As indicated Fitzpatrick *et al.* (2005), sources of uncertainty in residual stress measurements and the accuracy of calculations depends on elastic constants, non-linearity due to texture, stress gradients with depth and micro-stresses due to plastic deformation or grain interactions, etc. A surface roughness or interference of the sample geometry with the diffracted X-ray beam can result in systematic error in residual stress measurements (Prev y, 1986).



(a)



(b)



(c)

Fig. 4.2.6. Residual stresses on the top surface (white) and in depth of 15-80 μm (grey colour).

4.2.2. Residual stress in 3D samples with different shapes

Residual stresses were measured in the middle of the top surface of the cubes manufactured with/without support structures. For both cubes the values of the maximum residual stress were similar to the mean residual stress received for the samples that were 10–40 layers in height. Residual stresses in the cube produced with supports, were partially relieved by separation from the support structures during manufacturing (Figs. 4.2.7 – 4.2.8).

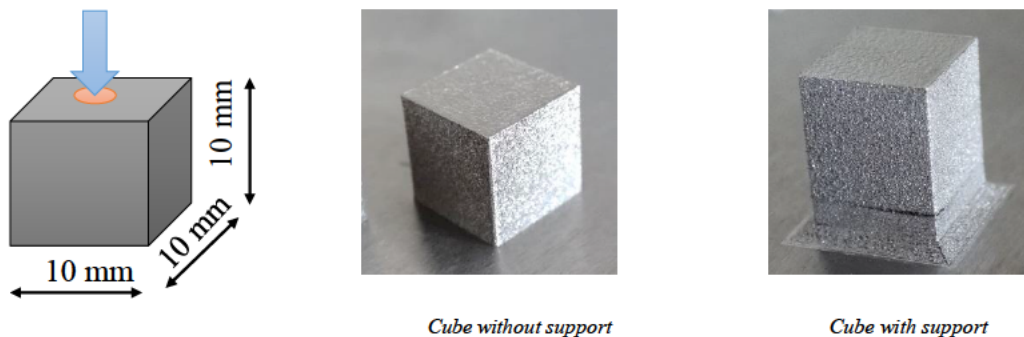


Fig. 4.2.7. As-built DMLS cubes produced with/without support structures

In the present work, residual stresses near the top surface in Ti6Al4V samples were tensile and very high. High variability of residual stresses can be linked to inhomogeneity of delivered powder layers which lead to different strains during cooling. Deformations and loss of the metallurgical contact with the previous layers during manufacturing led to the redistribution of stresses. A combination of high values of residual stresses in DMLS parts and imperfections such as porosity or lack of fusion between layers/supports/substrate can cause deformation and stress relaxation; it can finally affect the integrity of the part and its dimensions during manufacturing (Yadroitsava & Yadroitsev, 2015). Relaxation of the

stresses caused by partial separation of the 30mm×10mm×10mm parallelepiped from the substrate shown in Fig. 4.2.9. Residual stresses were lower in point 3 near the detached part of the sample.

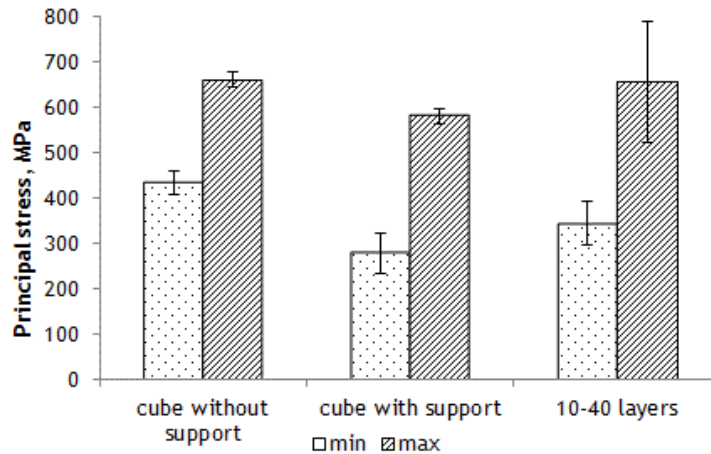


Fig. 4.2.8. Residual stress measured via XRD of cubes and layer samples produced via DMLS.

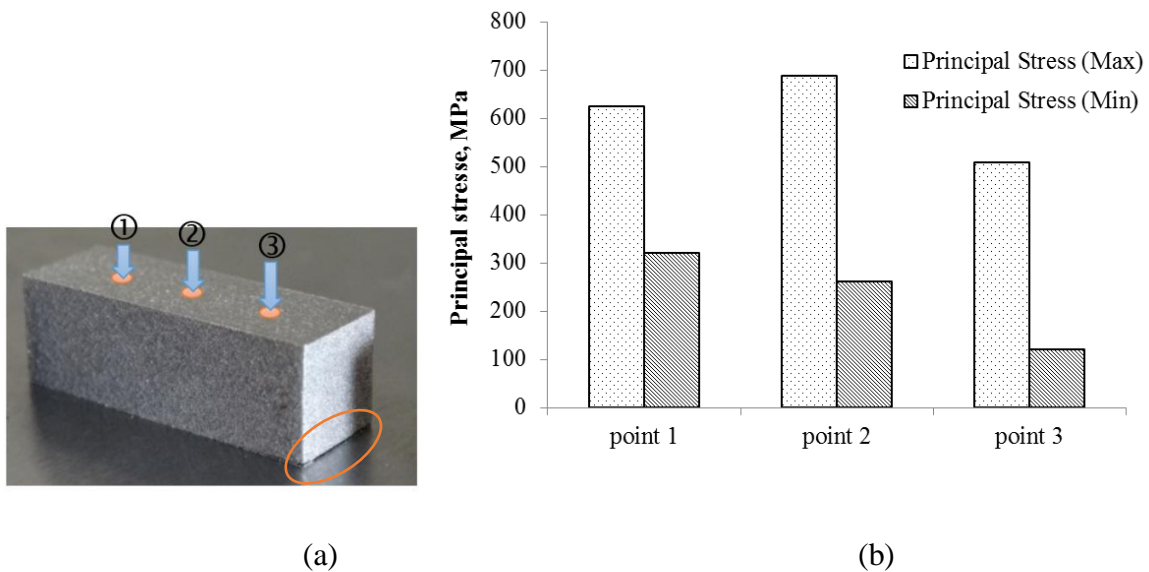


Fig. 4.2.9. a) The three points of measurement, delamination from the substrate circled; b) Measured Residual stress for the three points.

Fig. 4.2.10 illustrates how an imperfection of 0.005 mm³ (lack of metallurgical contact with the substrate) can influence the residual stress distribution. Residual stresses were lower in point 3 (Fig 4.2.9 (a)) near the detached part of the sample, which corresponds with *case 4* in Fig. 4.2.10. In the simulation basic internal stresses were introduced into the object.

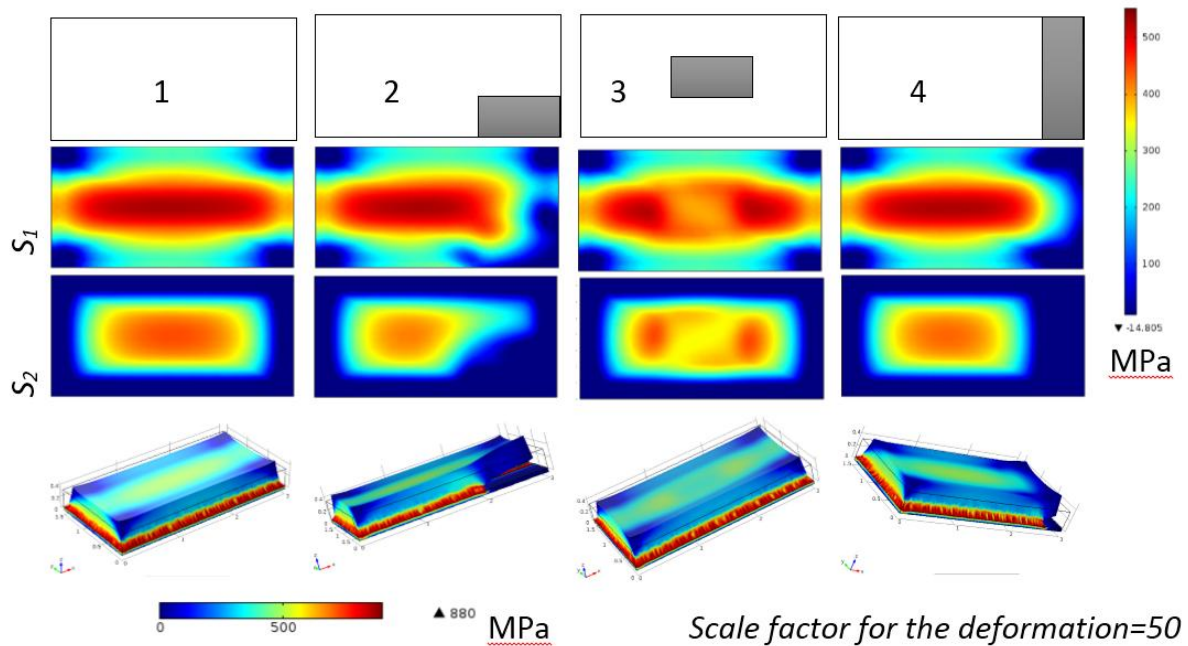


Fig. 4.2.10. Comsol simulation of residual stresses at the top surface in the parts $3 \times 1.5 \times 0.3$ ($x \times y \times z$ mm³) with/without imperfections. Initial stress $\sigma_{xx}=600$ MPa, $\sigma_{yy}=900$ MPa, $\sigma_{xy}=\sigma_{xz}=25$ MPa (Yadroitsava & Yadroitsev, 2015).

The residual stress near the surface in the primitive 3D objects that were produced as shown in Fig 3.5.2 was measured by XRD and the results are shown in Fig 4.2.11. For the semisphere without supports, the residual stress is lower in comparison to the general trend. In prisms, maximum residual stress near the surface was 915 MPa, where ratio of the top area to base surface was $100:9 = 11.1$. Prism with a lower ratio ($100:36 = 2.77$) had residual stress near the surface of 628 MPa. So during manufacturing for the samples with overhanging parts there is a higher probability of deformation of the upper part for stress relaxation.

Sample №24 is a cantilever 55 mm in length, 5 mm in width with beam 2 mm in height that was-built; thin walls as a support structure had a thickness of 0.8 mm (Figs. 3.6.1 and 3.5.2, sample №24). Residual stresses near the surface were measured (Fig. 4.2.12) in 3 places of the object: 6 mm from the edges (points a, c) and in the middle of the top part (point b). Partial separation of the cantilever from the substrate caused relaxation of the stresses. Residual stresses were lower in point c near the detached side of the sample, which corresponds with case 4 in Fig. 4.2.10. Principal residual stresses varied greatly, the maximum value was higher than residual stresses in Ti6Al4V objects manufactured without support structures (Fig. 4.2.12).

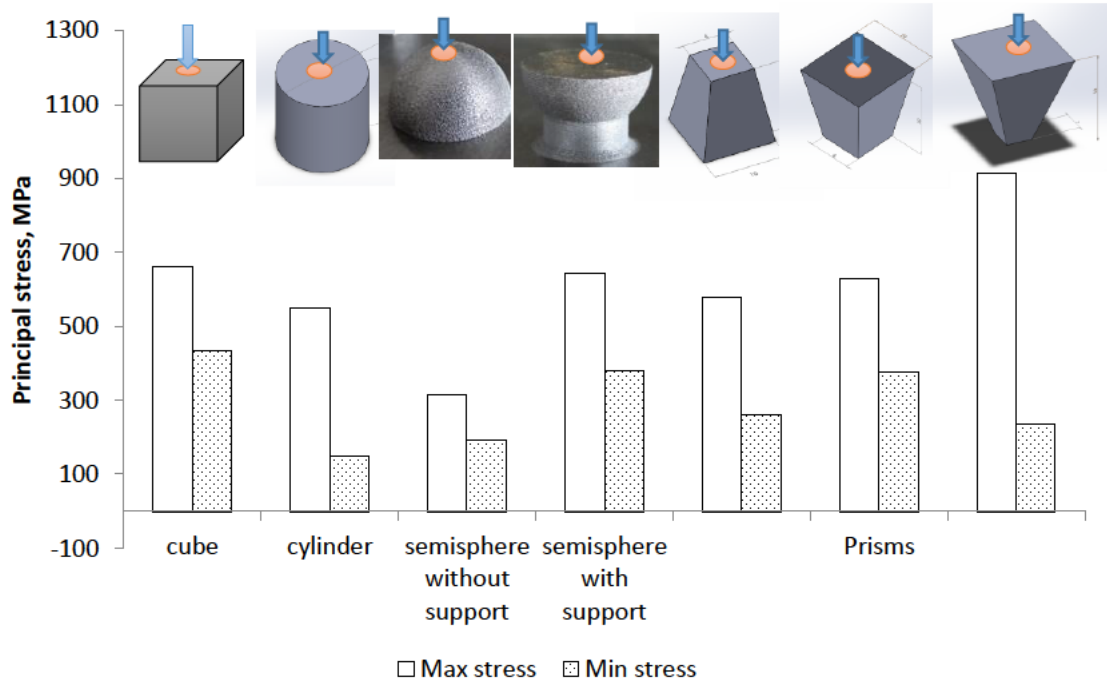


Fig. 4.2.11. Residual stress near the surface in 3D DMLS objects.

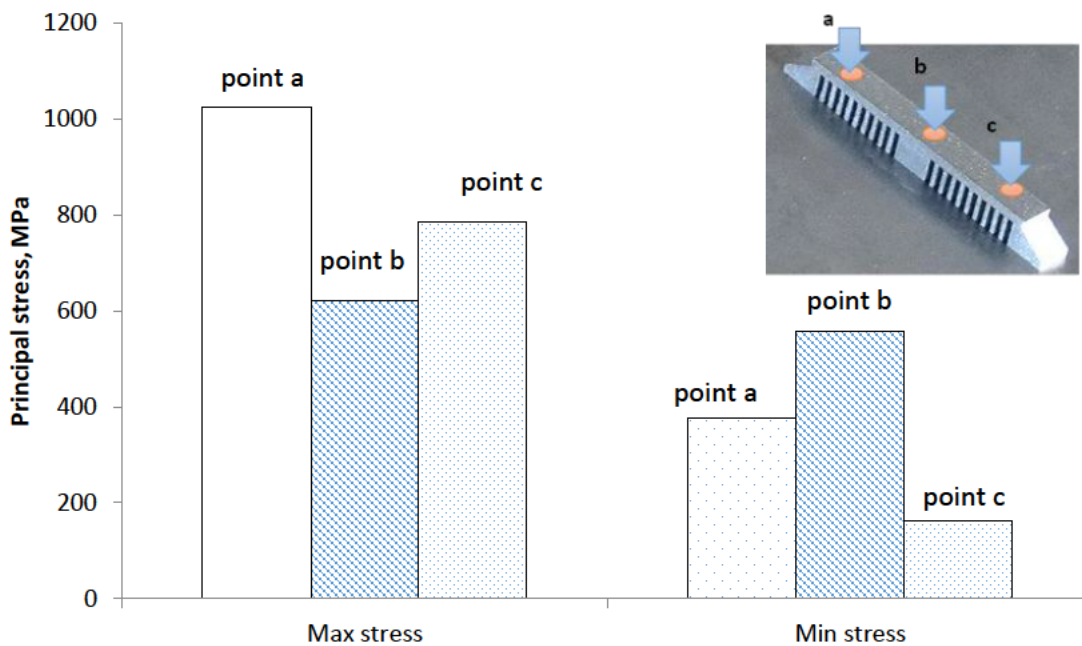


Fig. 4.2.12. XRD data for residual stress in cantilever near the surface.

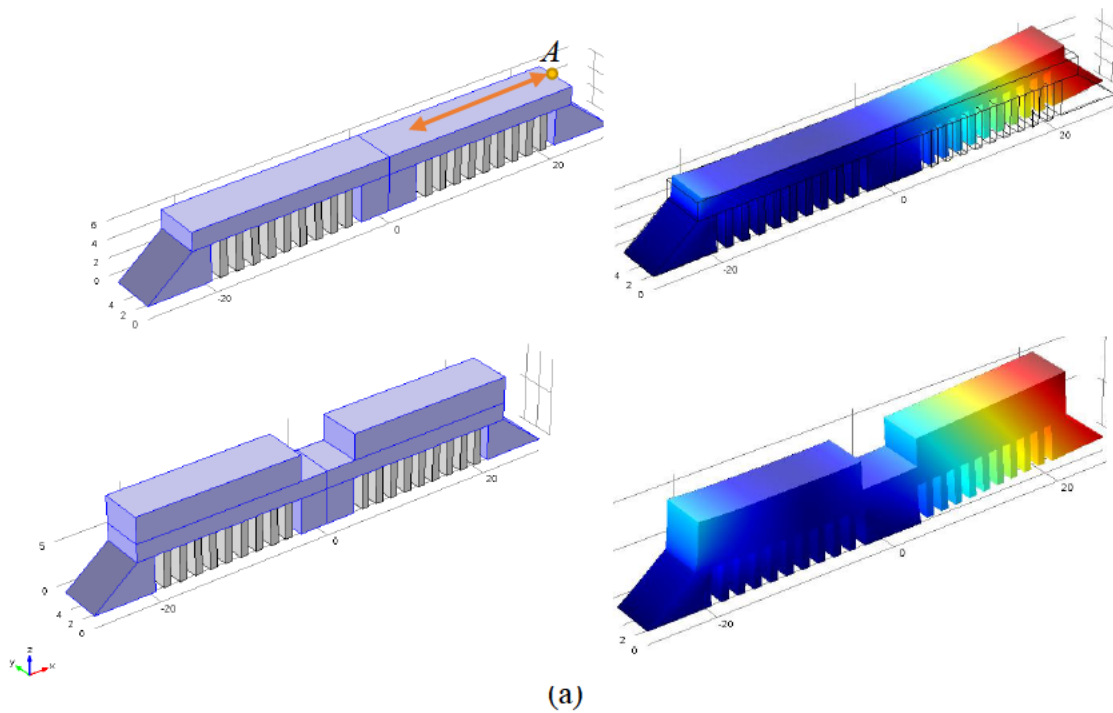
The residual stress present in the cantilever could be explained by the shape, as it was built with the longitudinal area exposed, this leads to a multiplication effect of the residual stress, this also declares the high value at point a as well as the delamination at point c.

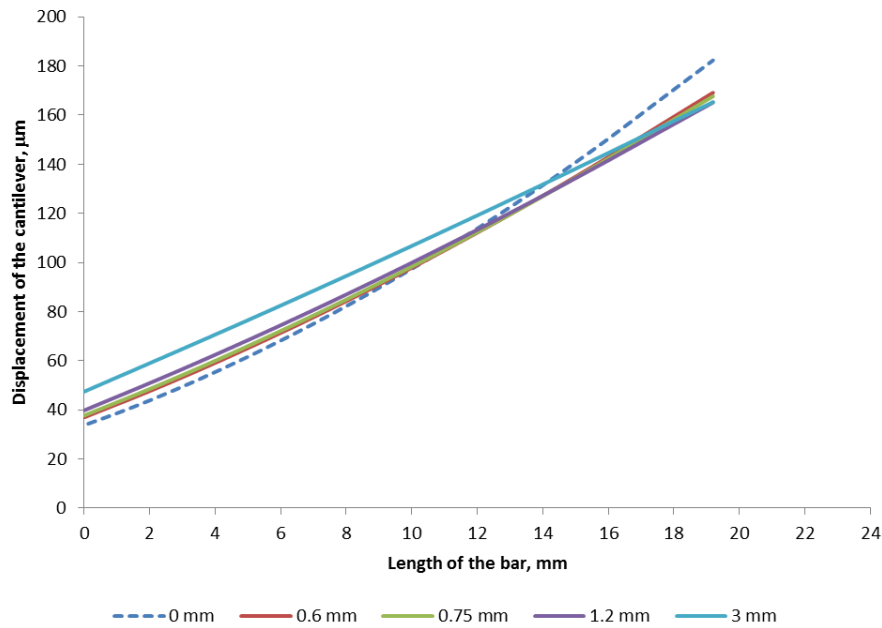
From the results given and discussed there are a few observations that can be made. Firstly, the residual stress in the DMLS samples produced were highly directional and coaxial with the scanning direction. The shape of the samples and supports structure influence on the residual stress near the surface. XRD measures were made only near the surface of the 3D objects, so from the XRD there is no evidence of the in-depth (multiple layers) residual stress within the samples.

4.3. Cantilever Curvature Method

The cantilevers were produced via DMLS on the EOSINT M280 system, different geometries were used to see whether height of samples or thickness play a vital role in the residual stress. Additional triangular supports at the end the cantilever arms were attached, as recommended by Buchbinder *et al.* (2014). 2 mm bars were built in the bottom part for EDM cutting. One arm of the cantilevers was separated from the substrate.

Numerical simulations by Comsol were done for cantilevers from wrought material with initial internal stress $\sigma_{xx}=900$ MPa and $\sigma_{yy} = 450$ MPa. Young's modulus was 113.8 GPa, Poisson's ratio was 0.342, density was 4423 kg/m³. For point A, maximum displacement was for the cantilever without upper block, deflections of the cantilevers with blocks were very close to each other (Fig. 4.3.1).





(b)

Fig. 4.3.1. Numerical simulation of the cantilevers with/without different upper blocks (a) and displacements of the cantilevers in z direction (b).

One arm of the manufactured cantilevers was separated from the substrate via EDM as seen in Fig 4.3.2 and then scanning was done by the Kreon Ace scanner. For manufactured cantilevers with different top thickness, the deflection in the z direction was obtained via the data received from the GeoMagics software, the deflection relatively consistent especially for sample sets C and D though some inconsistencies were picked up (Table 4.3.1 Fig. 4.3.3). The error of the Kreon arm is roughly 5-7 μm , this may explain most of the inconsistencies but certainly not all.

In relation of the geometric variations of the samples to the deflection it was found, that there is no distinction in the data (Fig. 4.3.3). Since the mechanical properties of the DMLS and wrought material are different, and introduced stresses were uniform, values of the deflections differ considerably for the model and experimental data; but the same behaviour suggests independence stress and the height of the produced DMLS samples up to 3 mm.

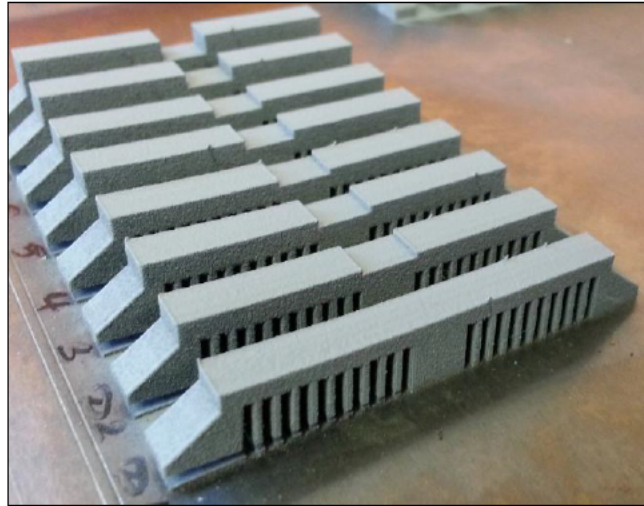


Fig. 4.3.2. Samples after separation with EDM, the deflection clearly visible.

Table 4.3.1. Deflections of the cantilevers

Sample's No	Deflection of the cantilever, μm			
	Group A	Group B	Group C	Group D
25	673	889	880	842
26	536	867	694	786
27	628	840	726	793
28	850	784	786	727
29	840	861	746	740
30	1006	806	715	765
31	840	739	758	714
32	821	783	727	785

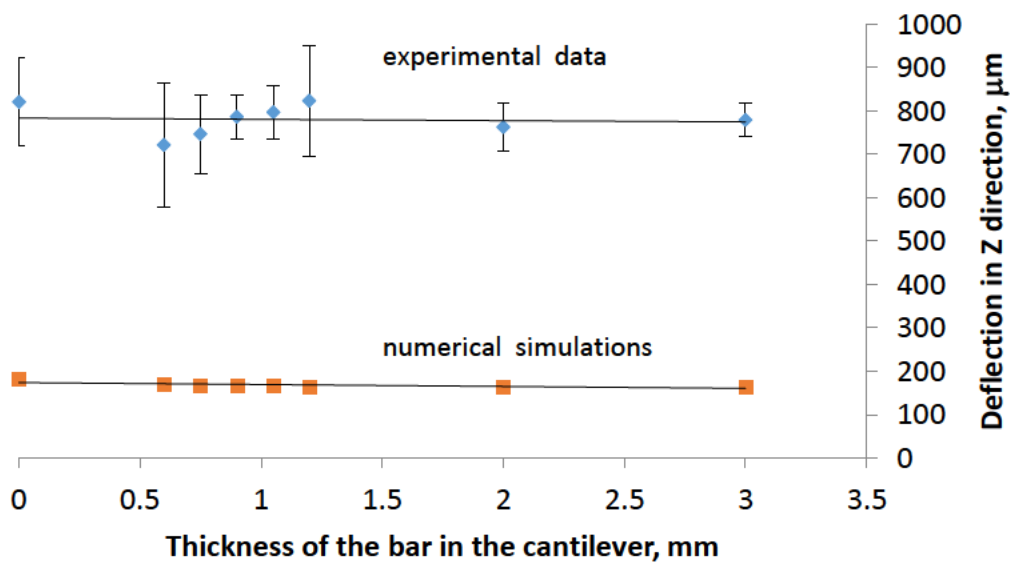


Fig. 4.3.3. Measured deflection of the samples *versus* thickness of the bar on the arm of the cantilever.

With the increase in volume of the sample at addition of layers with high stresses, a zone with a high resulting stress is formed at the bottom of the sample, which leads to a separation of the sample from the substrate/support structures (Fig 4.3.4 & 4.3.5). This is especially true when the geometry is such that there is the possibility of point or spike stress at severe angles. Therefore it justified the use of most of the base area for mounting parts on the substrate, as it is shown in Fig. 4.3.5. In this work only stress in the xy plane was investigated, and of course, the magnitude and direction of the stresses along the z axis are also important and should be subject to further studies.

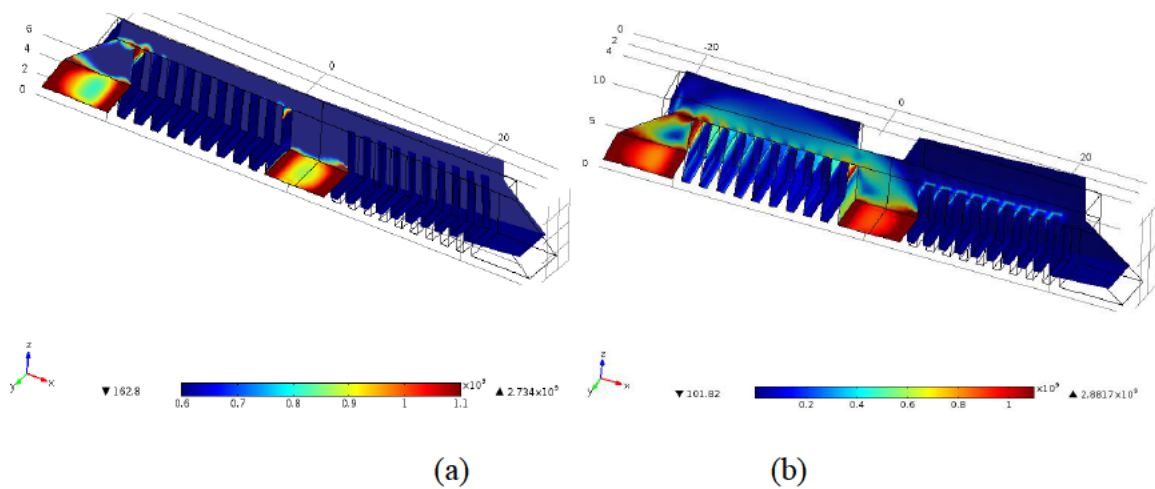


Fig. 4.3.4. Von Mises resulting stress of the cantilevers with increasing volume.

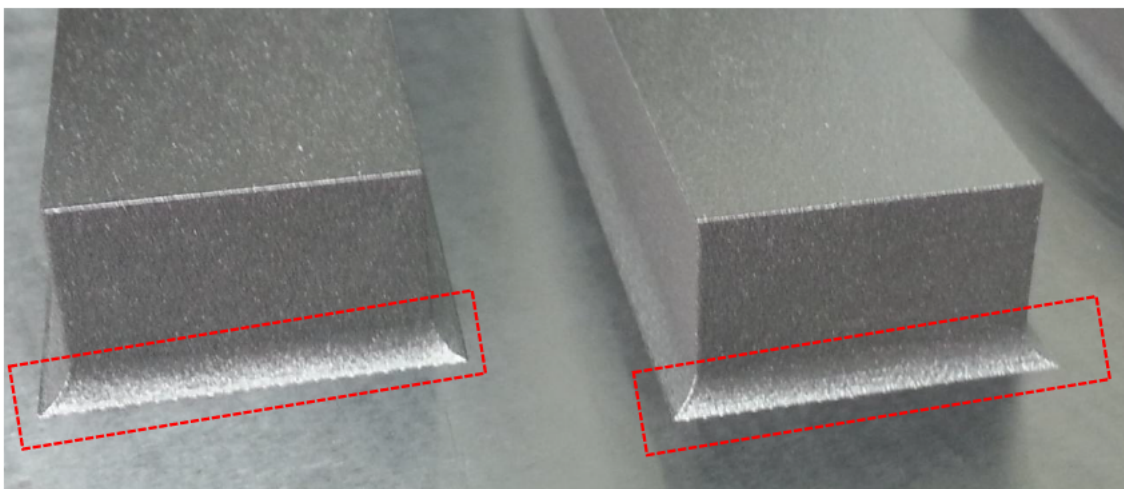
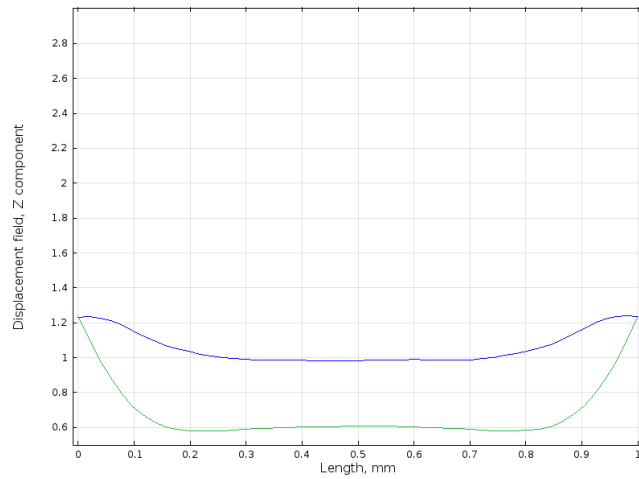
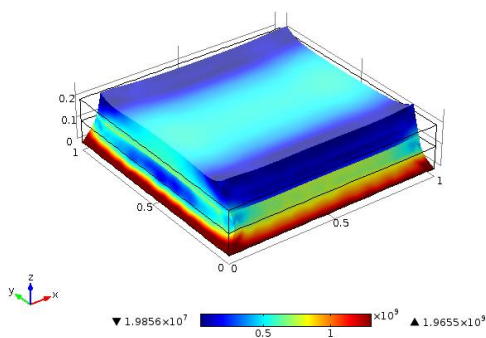


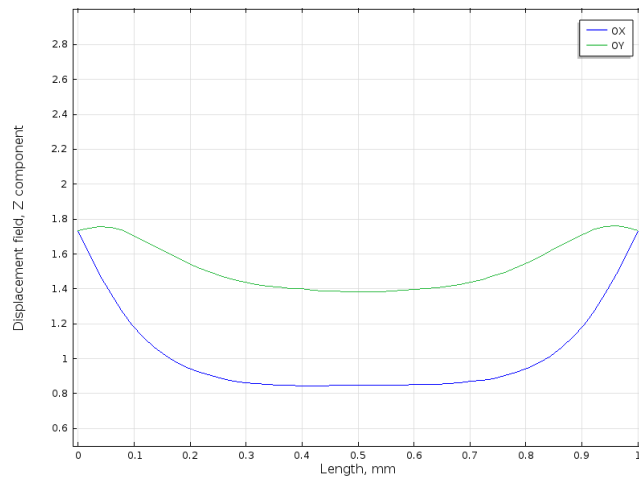
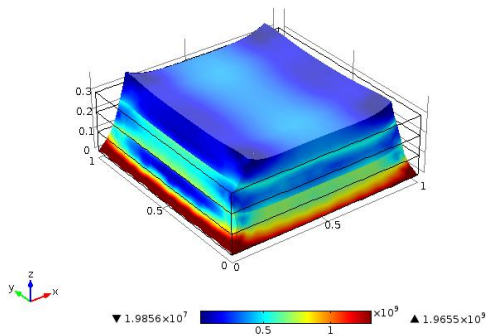
Fig. 4.3.5. Special mounting for the massive samples at the substrate.

Internal stresses are formed during solidification of molten material. For the same process-parameters for certain powder, the value of stress does not change, but stress

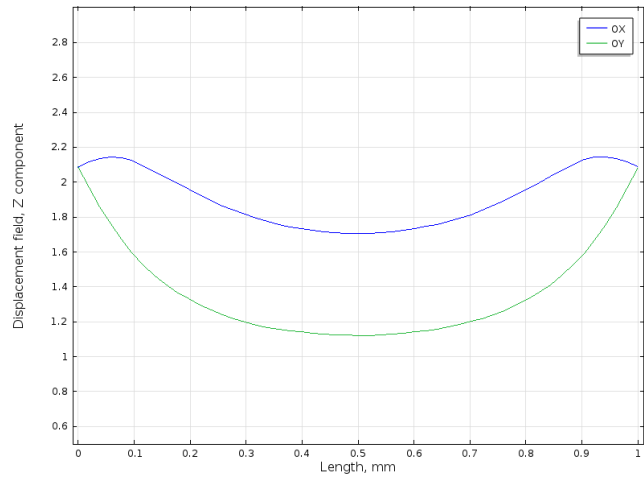
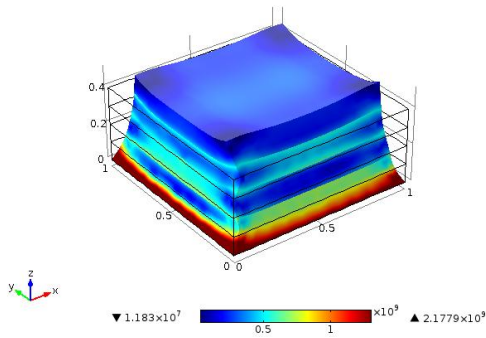
relieving and deformation of 3D objects with various shapes during processing DMLS are different. To describe deformations in z direction for multi-layer samples (height of the each layer is $100\ \mu\text{m}$), a simple model with alternating initial stresses in each layers was used (Fig. 4.3.6-4.3.8). For example, for 4-layer sample, 1st and 3rd layers had initial stresses $S_{xx} = 900\ \text{MPa}$ and $S_{yy} = 450\ \text{MPa}$; 2nd and 4th layer these values were $\sigma_{xx} = 450\ \text{MPa}$, $\sigma_{yy} = 900\ \text{MPa}$.



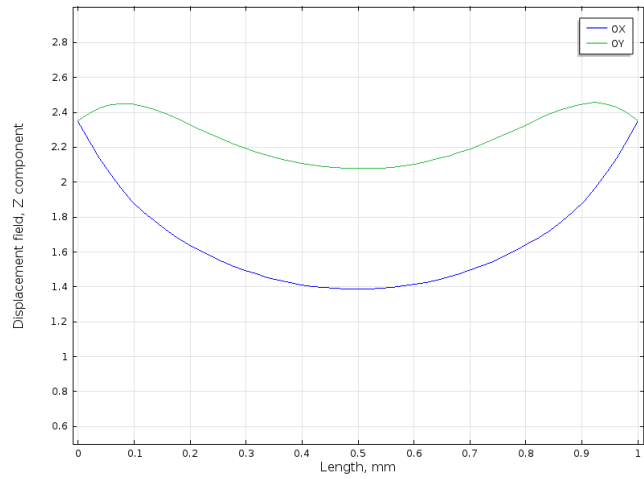
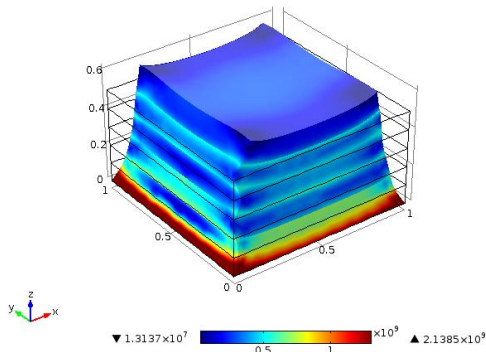
Two-layer sample



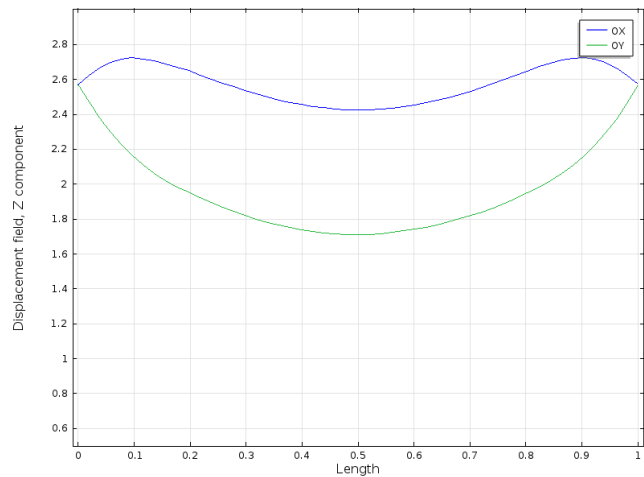
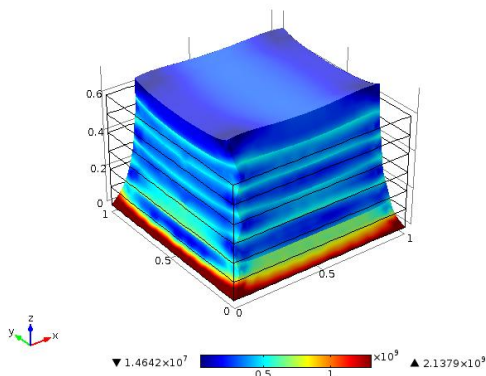
Three-layer sample



Four-layer sample

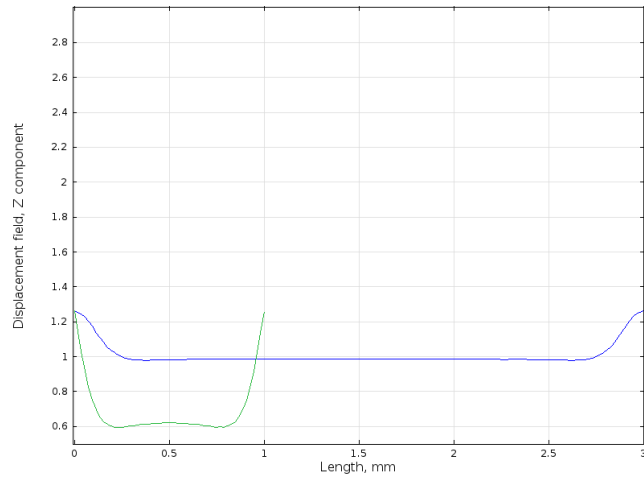
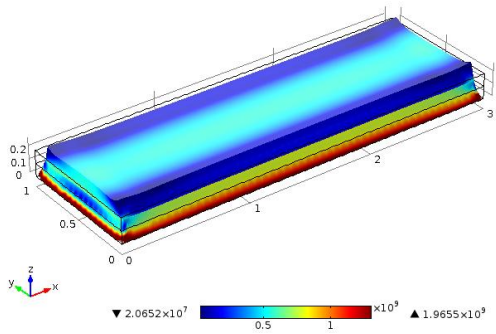


Five-layer sample

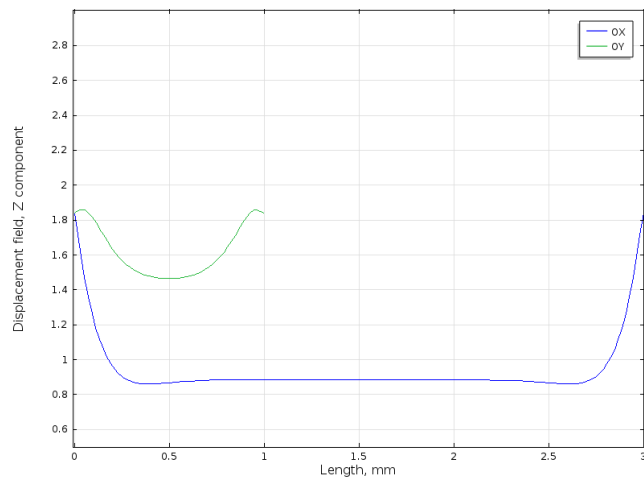
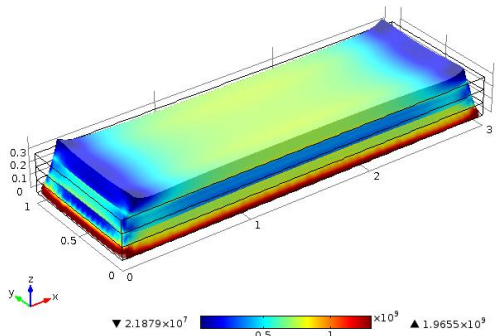


Six-layer sample

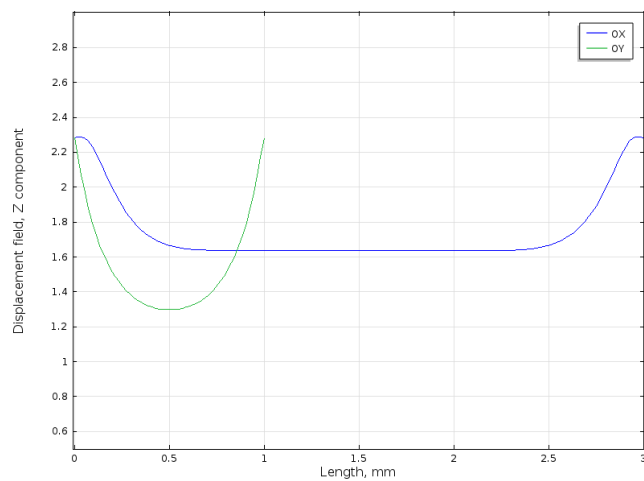
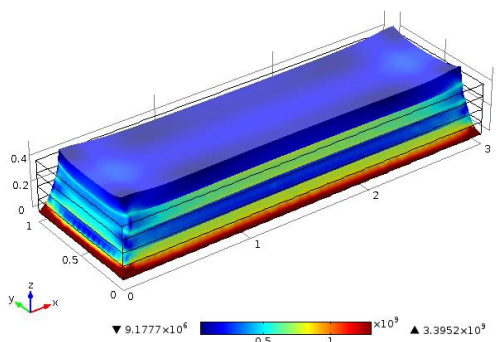
Fig. 4.3.6. Von Mises stress and deflection in z direction (μm) of the square samples *versus* the number of layers.



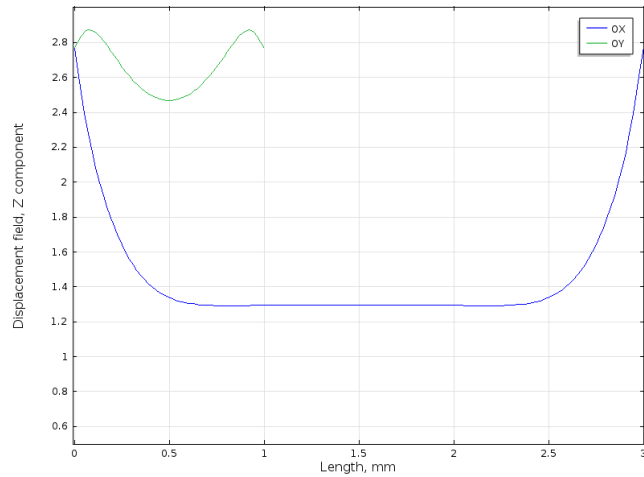
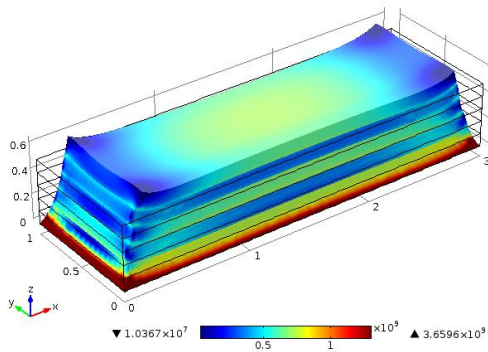
Two-layer sample



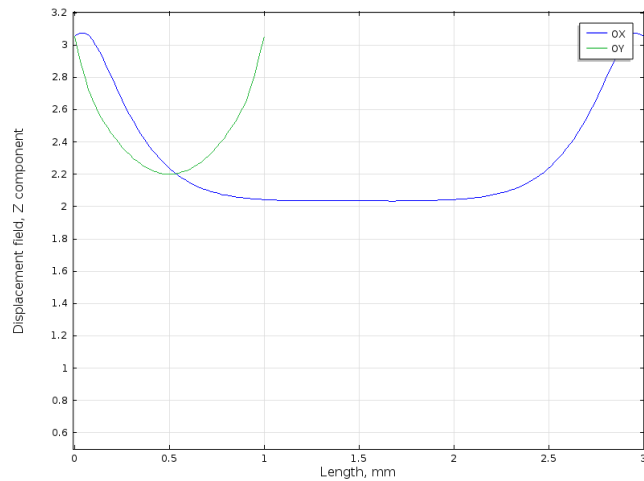
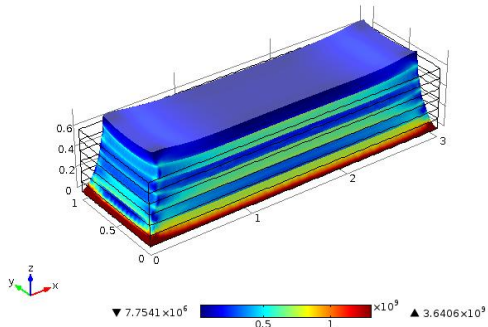
Three-layer sample



Four-layer sample



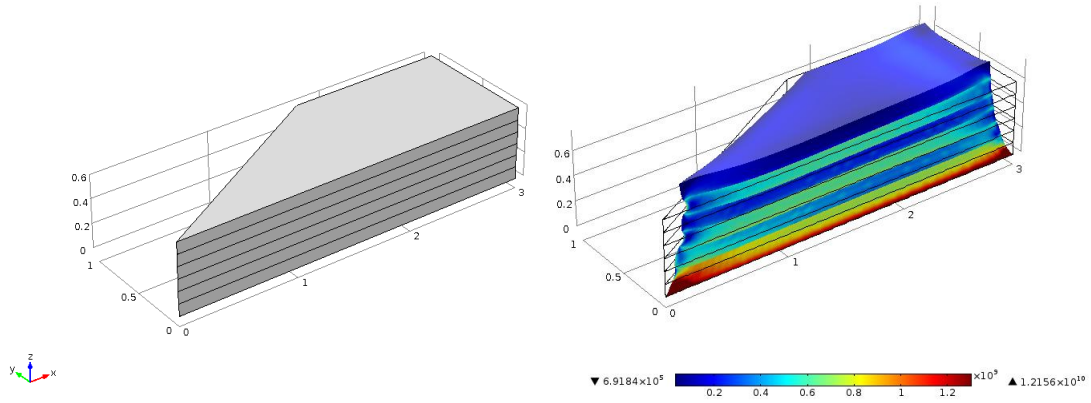
Five-layer sample



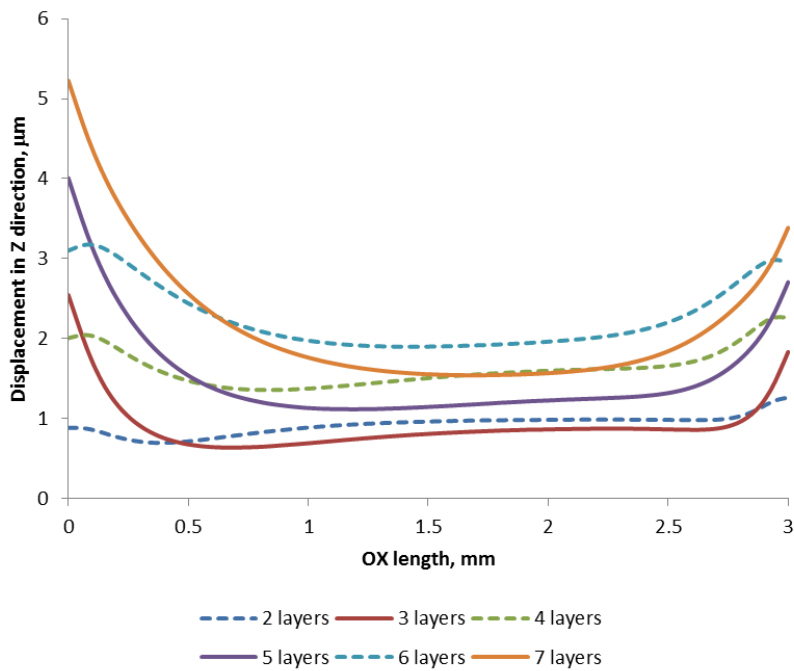
Six-layer sample

Fig. 4.3.7. Von Mises stress and deflection in z direction of the rectangular samples *versus* the number of layers.

For DMLS samples with a complex shape, due to the fact that the maximum stress during DMLS develops in the scanning direction, relieved stress within the elastic model will be more complex and those areas of the object, which are small in size or sharpness, will be greatly deformed in comparison with the rest of the areas of the object (Fig. 4.3.8– 4.3.9).



(a)



(b)

Fig. 4.3.8. Von Mises stress for six-layer sample (a) and deflection in z direction of the complex samples versus the number of layers (b).

As seen in Fig. 4.3.8, the deformation of multi-layer complex shapes vary vastly in context of the Z direction displacement, depending on the scanning direction the amount of displacement will be affected adversely with every alternating layer depending on the direction change. In Fig. 4.3.9, it is possible to see the deformation a similar complex geometric part.

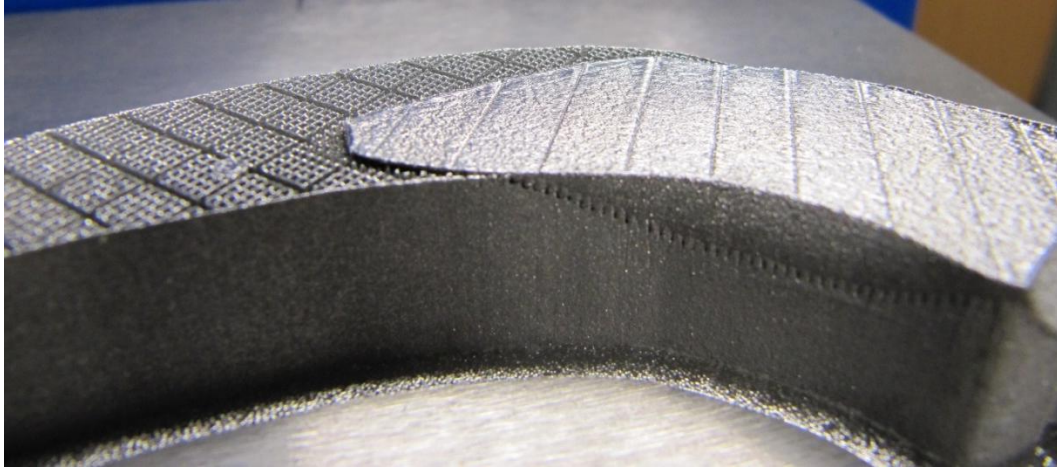


Fig. 4.3.9. Distortion of the thin long part of the sample during manufacturing.

4.4. Hardness Test and Mechanical Properties

Vickers micro-hardness at loading 300 g was applied to as-built DMLS components. Sample 16 (rectangular block) was removed from the substrate. The sample was sectioned by EDM to obtain 3 planes, xy , zx and yz . Hardness tests were done on all sections (Appendix 3), and the average hardness obtained was as follows:

- $HV_{xy} = 387 \pm 11.9$
- $HV_{zx} = 390 \pm 19.5$
- $HV_{yz} = 391 \pm 11.6$
- $HV_{total} = 389 \pm 14.8$

The values for each of the cross-sections is relatively equal and do not show statistically significant differences with reference to the building direction of the DMLS process. The indentations that were made in different cross-sections showed similar shapes (Fig. 4.4.1).

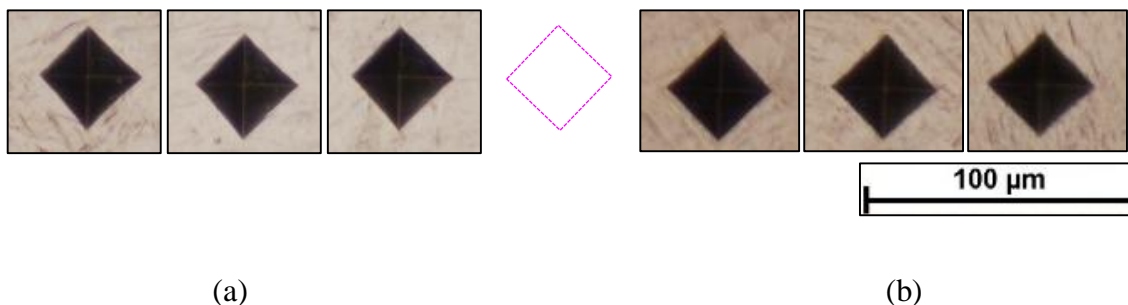


Fig. 4.4.1. Indentations in the xy (a) and zx cross-sections (b). Building direction is z axis.

48 Rectangular horizontal Ti6Al4V (ELI) samples were built on the M280 machine. 5 as-built samples was cut and tensile round specimens 4 mm in diameter and gauge length 4 times the diameter were produced as recommended by the ASTM E8M-13a standard (Table 4.5.1 and Appendix 6).

Table 4.5.1. Tensile properties of as-built DMLS samples

Specimen label	Area, mm ²	Tensile stress at Yield (Offset 0.2 %), MPa	Modulus (Chord 200 MPa – 800 MPa), GPa	UTS, MPa	Elongation, % 4.D	Area reduction, %
1	14.79	1101	111	1271	8.8	24.94
2	14.79	1096	115	1267	9.1	25.34
3	14.73	1099	109	1259	9.8	29.33
4	14.73	1096	113	1261	9.7	25.79
5	14.66	1097	111	1266	9.6	22.63
Mean	14.74	1098	112	1265	9.4	25.61
Standard deviation	0.057	2	2	5	0.46	2.414
Coefficient of variation	0.39	0.18	1.89	0.38	4.44	9.43

The horizontally built DMLS Ti6Al4V specimens showed higher microhardness, yield and ultimate strength but lower failure strain and reduction of area were lower than the conventional Ti6Al4V alloy (Table 3.1.1). This is most likely due to dominant martensitic α' structure and also the residual stress present (Vlcak *et al.*, 2015) in the components.

4.5. Stress Relieving in Inert Atmosphere

Stress relieving of DMLS samples was done in-house at CRPM, the furnace utilizing argon as protective atmosphere. This is important as titanium picks up interstitial elements (N, O, H) readily above 500°C. Nitrogen especially hardens the surface of titanium. The furnace showed evidence of interstitial pick up as shown in Fig. 4.5.1 and 4.5.2 with oxide layers forming on samples that were stress relieved.

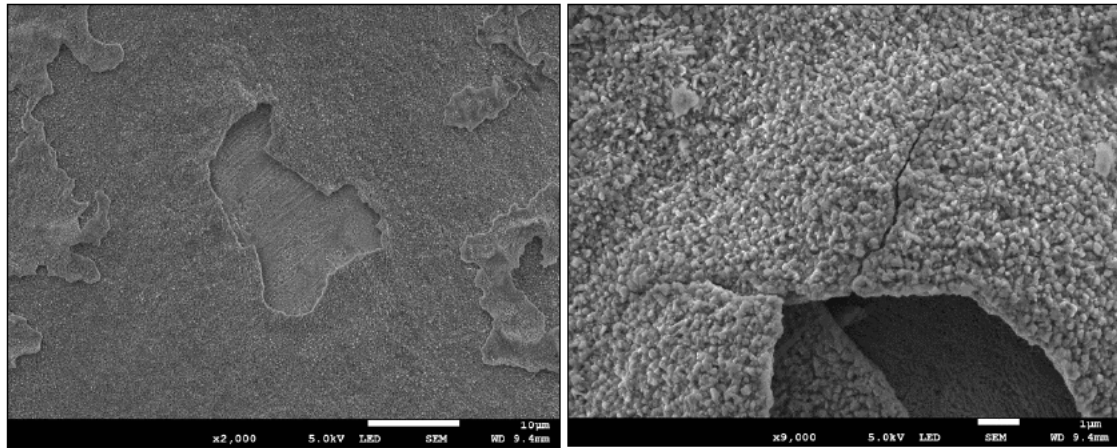


Fig. 4.5.1. Oxide layer formed during stress relieving heat treatment of Ti6Al4V sample without Inert Box.

The concern was that oxidation had reduced ductility, hence the Inert Box was designed and installed as mentioned in the previous Chapter. The results from the implementation of the Inert Box seemed promising. Discoloration (oxidation/ nitrogenisation) still took place as shown in Fig. 4.5.3, but only in the part where argon gas entered to the chamber directly. ‘Cleaning’ of the entered Ar can take place since at 650°C Ti alloy is very active at this temperature.

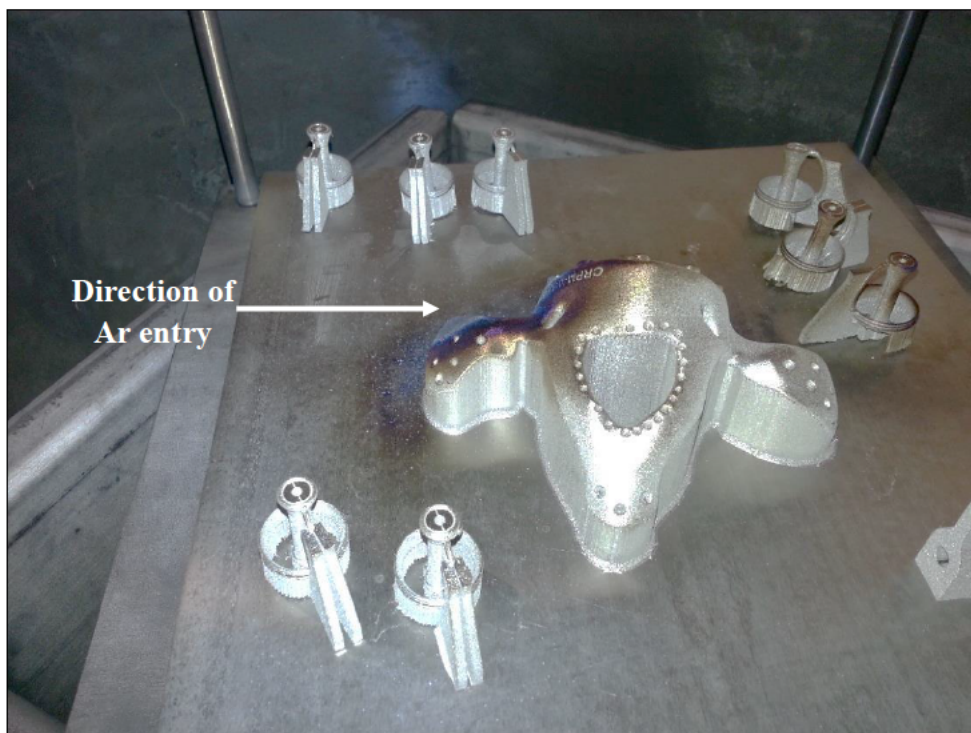


Fig. 4.5.3 Medical implant showing slight discoloration after stress relieving at 650°C for 3 hours.

After the aforementioned post processes little or no residual stress is present in parts manufactured by DMLS. After stress relieving was done the other half of the sets of

cantilevers were separated via EDM, little to no deflection was present (Fig 4.5.4 the deflection from the cantilevers were about 0 degrees).

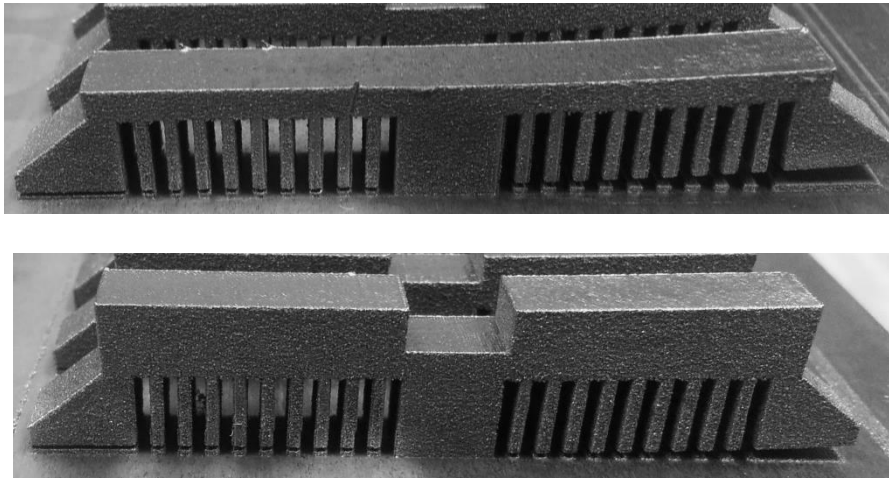


Fig. 4.5.4. Cantilevers after stress relieving (left arm didn't curl up after stress-relieving heat treatment).

This indicates that the stress relieving that was introduced was successful (the same regime was followed throughout), other results from tensile tests which were done independent of this study also confirmed that the stress relieving process was successful, this is a noteworthy accomplishment with the light on the application of Ti6Al4V parts for industry purposes. Measured residual stress after heat treatment was about 30 MPa (Yadroitsava *et al.*, 2015). Vickers microhardness for stress-relieved DMLS samples was 374 ± 17 (Appendix 5). This value was statistically lower (*t-test*, $p < 0.001$) than in the as-built samples.

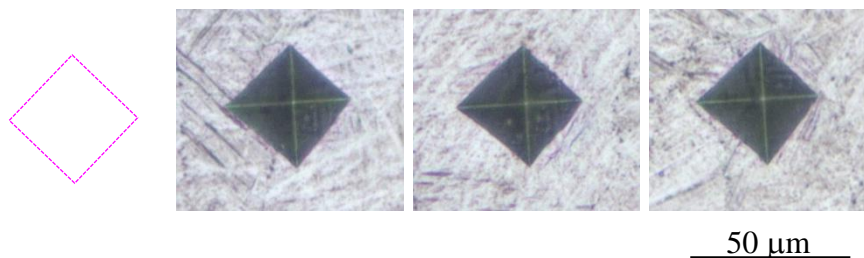


Fig. 4.5.5. Indentations in zx cross-section of stress-relieved sample. Building direction is z axis

The indentations that were made in as-built and stress-relieved samples showed similar shapes (Figs. 4.5.5 and 4.4.1). Slight concavity can suppose that the surface measured were slightly out of plane. As Totten (2002) indicated, various approaches to interpreting and correlating the indentation loads and shapes with residual-stress field on the surface and near surface regions of materials have been proposed. “*However, indentation methods have not*

earned the degree of confidence of XRD or hole-drilling methods for general applications and thus are rarely applied” (Totten, 2002).

Knowles *et al.* (2012) found that the stress-relieving heat treatment (650°C for 8 hours) didn’t affect the DMLS Ti6Al4V significantly on the microstructural and hardness levels. HV₁₀ for as-built samples was 379±5 *versus* 377±9 for stress-relieved samples. After stress-relieving the thin α’ phase in the microstructure was noticeable, as before with the untreated specimens. Residual stress near the surface measured by drilling method was about 1000 MPa and it was ~400 MPa in the top surface stress-relieved samples (Knowles *et al.*, 2012).

With regard to the mechanical properties, there seems to be a slight gain in ductility of the specimens once stress relieved (Table 4.5.2.) in comparison to the as-built samples. After stress-relieving horizontal tensile specimens had an average ultimate tensile strength of 1170±5.7 MPa and elongation at break of 10.9±0.75% (Table 4.5.2). Cain *et al.* (2015) also applied the stress relieving heat treatment at 650 °C and the average ultimate tensile strength dropped from 1279 to 1187 MPa with a slight increase in elongation at failure (from 6% to 7%). The gain in ductility is critical in consideration with qualifying materials for application such as aerospace and medical fields, so these results seem promising.

Table 4.5.2. Tensile properties of stress-relieved DMLS horizontally built samples

Specimen label	Area, mm ²	Tensile stress at Yield (Offset 0.2 %), MPa	Modulus (Chord 200 MPa – 800 MPa), GPa	UTS, MPa	Elongation, % 4.D	Area reduction, %
1	19.63	1090	114	1160	10.8	30.44
2	19.40	1098	120	1173	10.3	28.59
3	19.48	1103	116	1174	10.7	29.21
4	19.48	1099	117	1171	10.7	28.53
5	19.56	1100	118	1172	12.2	29.49
Mean	19.5	1098	117	1170	10.9	29.3
Standard deviation	0.088	5	2	6	0.8	0.78
Coefficient of variation	0.45	0.44	1.91	0.49	6.86	2.66

4.6. Summary

An overview of this section is as follows. Simulation of single track formation was done on the Comsol software, utilizing some of the known process parameters, this was not

done to simulate stress but rather the thermal cycle during the DMLS process, the thermal gradient was shown to be high.

The microstructure of produced samples were compared to that of literature, the martensitic structure coincided with the literature as expected for DMLS, after stress relieving no visible changes in the microstructure were found as viewed by optical microscopy.

The residual stresses in multi-layer samples were shown to be high in the top layer, as well as coaxial to the scanning direction. The roughness of these samples were investigated to see whether it may have affected the XRD results adversely it was found not to be the case though some correlation was found between the 2nd principle stress and the roughness.

The residual stresses in primitive 3D components were investigated, the results conformed to the multi-layer samples though two anomalies were present and explained, delamination occurred in some of the 3D samples.

Delamination from normal internal stress were simulated in Comsol for basic rectangular samples, the redistribution of residual stress due to delamination confirmed the real redistribution of stress that was found with the XRD results.

Cantilevers were produced and separated via EDM in the as-built state, the deflection due to residual stress was measured showing a certain trend and this coincided with simulations done in Comsol which showed the same trend. Residual stress was high. The cantilevers were then stress relieved and separated via EDM, in this instance there was insignificant deflection observed, showing no presence of residual stress.

To reduce stresses in samples that are made for industry the mounting method has been adapted slightly to reduce the multiplication effect of residual stress on sharp corners and geometries. Further investigating of the stress concentration a basic simulation was done with a rotation of internal stress at each layer, this clearly showed displacement in the Z axis at the corners of the objects. A more complex shape (triangle) was also done and this clearly showed a more severe deflection due to internal stresses, this was compared to a similar real world case where a similar shape delaminated during processing, showing that the shape and volume of objects play a definitive role in residual stress.

Micro hardness tests were conducted on the as-built samples; the hardness was high this may be due to the residual stress involved, stress relieved samples were also tested and found that the hardness value was lower this may show evidence of a correlation between residual stress and hardness of samples.



Stress relieving was plagued with oxidation and interstitial pick up, therefore an inert-box was produced to limit the contamination. The samples were stress relieved in the box and lower interstitial pick up was seen as colouration still occurred.

From recent tensile tests, stress relieved samples showed good strength and ductility which is promising.

Chapter 5: Conclusion and Future work

The aim of this study was to determine the residual stress in Ti6Al4V (ELI) components, produced by DMLS using standard EOS process parameters, as well as the post-processing treatment required to relieve the residual stress.

The residual stress was determined using quantitative and qualitative methods. The XRD results revealed high amounts of surface residual stress in the as-built samples. Cantilevers that were produced and then analysed namely by the cantilever-curvature method showed conclusively the presence of residual stress throughout the components.

Further investigation revealed multiple in-process failures of parts due to residual stress, these were also attentively studied. The stress relieving at 650°C for 3 hours is satisfactory for stress relieving of DMLS Ti6Al4V alloy.

The objectives for this study was the following:

1. Studying the DMLS process
2. Powder characterisation
3. Microstructure and residual stress investigations
4. Analysis of the sources of residual stress during DMLS
5. Simulation of temperature distribution at laser melting and residual stress relaxation in 3D objects
6. Determine the residual stress and mechanical properties in as-built Ti6Al4V(ELI) experimental parts produced by EOSINT M280 DMLS with standard process parameters
7. Determination of regime of stress relieving heat treatment for Ti6Al4V alloy and improvement of existing CUT/CRPM equipment.

Touching on the aforementioned briefly;

- DMLS process and its capabilities were studied.
- Employed Ti6Al4V (ELI) powder was described.
- Properties of wrought Ti6Al4V α/β alloy and microstructure of as-built and stress-relieved DMLS Ti6Al4V (ELI) were analysed.
- Definition, origin and nature of residual stress for processes are explained as well as the detrimental effects of residual stress for DMLS: distortion, cracks and delamination from support structures during manufacturing. Different techniques for detection and measurement of residual stress were studied.

- The residual stress in as-built DMLS components was determined to be large and has very variable values. The maximum stresses were co-axial with the scanning direction.
- The source of residual stress in DMLS have multiple facets, the most critical from this study are rapid solidification, high thermal gradients and thermal cycling during DMLS. Lack of fusion and pores play critical role in distribution of residual stress in 3D objects.
- Simulation of residual stress and temperature distribution of 3D DMLS objects is challenging and this study further ascertained this.
- Some basic structures with perpendicular internal stresses were introduced to simulate relieving of the residual stress during manufacturing have shown that the volume and shape of samples play a critical role in the residual stresses in 3D DMLS components.
- Microhardness and tensile properties in as-built Ti6Al4V(ELI) experimental parts were studied.
- Chosen regime of stress relieving heat treatment for Ti6Al4V alloy was effective in the 'improved' (Inert Box addition) oven.
- Residual stress in relieved parts was shown to be low. The currently employed stress relieving process is satisfactory though interstitial control must be ensured.

The study also turned into the direction of focussing on avoiding in-process failure, this is by all means the main concern and worst symptom of residual stress in the DMLS process. Some of the following recommendations touch on this topic specifically.

Preheating the Substrate: Literature indicated that preheating even at 200°C is effective for limiting residual stress for DMLS; it seems as a promising avenue in preventing in process failure due to residual stress. Preheating at high temperatures might lower the life cycle of powder and limit its reusability.

In-Situ Stress-Relief: Apart from pre-heating other in situ relief may have to be looked into. Rescanning with a second heat source which is not as focused as the main energy source in the DMLS process, may lead to better control of thermal gradients, though this solution is more of a machine building problem, as it will have to be integrated into the system as a whole. Yet this is just a proposal on the authors' side for possible further

investigation, according to his knowledge some institutions are already pursuing this avenue of research.

Part Orientation on the building platform is a key area which engineers and designers must take into account before initialising the DMLS process. Objects need be oriented at the building platform to minimise overhanging.

Design and Supports. A lot in the media has been said about 3D specific design. This is an agreed concern as designers must take into account for which process they are modelling SLA, DMLS, EBM, FDM etc. There are unfortunately some design limitations for manufacturing purposes though AM is marketed as making the impossible possible. These limitations include influences of residual stress in some geometries and most processes. In DMLS, support structures are utilised in parts with acute overhanging elements, usually less than 30° to the horizontal, in the powder bed of DMLS such overhanging elements cannot support itself under its own weight and cannot accommodate the force exerted by the recoater. Supports are crucial, as the area of contact with the actual part will influence the heat transfer throughout the process which in turn will have an either positive or negative effect on the distribution and development of residual stress. The influence of the contact area and type of support on residual stress is the subject of further research. These two elements, part design and supports structures, may hold another key to manage residual stresses, parts in themselves may be designed more robust ensuring minimal or no distortion, but also supports that allow some minimal flexibility but maintain strong metallurgical contact could aid microns of flexing of the part but prevent failure as a whole. This aforementioned is a generalisation of a possible management solution, but could be tailored to specific components.

Authors' note: The ideal solution to residual stress, will not add additional manufacturing time. Post processing of Ti6Al4V parts will most likely remain a vital process especially concerning aerospace and medical application. As innovators, researchers and manufacturers develop intrinsic solutions to the obstacles such as residual stress it will lead to a more general application of this technology. The critical point in DMLS now is to eliminate in process failure due to residual stress, so that cost and time inputs by industry may be cut, so doing the DMLS process may be more attractive to mid-market users, at present it remains in a niche market.

Chapter 6: References

- Additively Ltd. (Additively AG) (2013). Laser Melting. (Online) Available from: www.additively.com/en/learn-about/laser-melting (Accessed January 29, 2015).
- Aero (2015). Ti6Al4V. (Online) Available from: www.aerospacemetals.com/titanium-ti-6al-4v-ams-4911 (Accessed May 7, 2015).
- AMT (2015). Connecting Rods. (Online) Available from: www.amt-advanced-materials-technology.com/connectingrods (Accessed February 25, 2015)
- ASTM E 837 *Standard method for determining residual stresses by the hole-drilling strain gage method*, Annual Book of ASTM Standards, (2008).
- ASTM E8 / E8M-15a, *Standard Test Methods for Tension Testing of Metallic Materials*, ASTM International, West Conshohocken, PA, 2015.
- ASTM F136-13, *Standard Specification for Wrought Titanium-6Aluminum-4Vanadium ELI (Extra Low Interstitial) Alloy for Surgical Implant Applications (UNS R56401)*, ASTM International, West Conshohocken, PA, 2013
- ASTM F2792-12a, *Standard Terminology for Additive Manufacturing Technologies*, (Withdrawn 2015), ASTM International, West Conshohocken, PA, 2012, pp. 10-12.
- Balasubramanian, S. & Anand, L. (2002). Plasticity of initially textured hexagonal polycrystals at high homologous temperatures: application to titanium. *Acta Materiala*, 50, pp. 133-48
- Barile, C., Casavola, C., Pappalettera, G & Pappalattere C, (2014). Analysis of the effects of process parameters in residual stress measurements on Titanium plates by HDM/ESPI. *Measurement*, 48, pp.220–227.
- Bertol, L.S., Kindlein J.W., da Silva F.P. & Aumund-Kopp C. (2010). Medical design: Direct metal laser sintering of Ti–6Al–4V, *Materials & Design*, 31 (8), pp. 3982–3988.
- Boivineau, M. Cagran, C. Doytier, D., Eyraud, V., Nadal, M.-H., Wilthan, B. and Pottlacher, G. 2006. Thermophysical properties of solid and liquid Ti-6Al-4V alloy, *International Journal of Thermophysics*, 27 (2), pp 507-529.
- Bourhis, F.L., Kerbrat, O., Dembinski, L., Hascoet, J.Y. & Mognol, P. (2014) Predictive model for environmental assessment in additive manufacturing process. *Procedia CIRP*, 15, pp.26–31.
- Britannica (2015). Bragg's Law & Crystal Structure. (Online) Available from: www.britannica.com (Accessed March 20, 2015)
- Brown, M.S., Arnold, C.B. (2010). Fundamentals of laser-material interaction and application to multiscale surface modification. In: Laser Precision Microfabrication, *Springer Series in Materials Science*, 135, pp. 91-120
- Buchbinder, D., W. Meiners, N. Pirch, K. Wissenbach, J. Schrage (2014), Investigation on reducing distortion by preheating during manufacture of aluminum components using selective laser melting, *Journal of Laser Applications* 26, 012004.

- Cain, V., Thijs, L., Van Humbeeck, J., Van Hooreweder, B., Knutsen, R. (2015) Crack propagation and fracture toughness of Ti6Al4V alloy produced by selective laser melting, *Additive Manufacturing*, 5, pp 68-76.
- CAMAL (2015). 3D Printing an Argon Diffuser for Heat Treatment of DMLS Parts. (Online) Available from: camal.ncsu.edu/3d-printing-argon-diffuser-heat-treatment-dmls-parts/ (Accessed January 29, 2015).
- Campoli, G., Borleffs, M.S., Amin Yavari, S., Wauthle, R., Weinans, H. &Zadpoor, A.A.(2013). Mechanical properties of open-cell metallic biomaterials manufactured using additive manufacturing. *Materials & Design*, 49,pp.957–965.
- Casalino, G., Campanelli, S.L., Contuzzi, N. & Ludovico, A.D. (2015) Experimental investigation and statistical optimization of the selective laser melting process of a maraging steel. *Optics & Laser Technology*. 65, pp. 151–158.
- Casavola, C., Pappalettere, C. & Tursi, F. (2011) Residual Stress on Aisi 300 Sintered Materials. *Experimental and Applied Mechanics*, Volume 6 17: 201-208.
- Casavola, C., Pappalettere, C. Tursi, F. (2010)Non-uniform residual stress fields on sintered materials // *9th Youth Symposium on Experimental Solid Mechanics*, Trieste, Italy, July 7-10, 132-137.
- Cheng, X.Y., Li, S.J., Murr, L.E., Zhang, Z.B., Hao, Y.L., Yang, R., Medina, F. & Wicker, R.B. (2012).Compression deformation behavior of Ti-6Al-4V alloy with cellular structures fabricated by electron beam melting. *Journal of the Mechanical Behavior of Biomedical Materials*, 16, pp.153–62.
- Colegrove, P.A., Coules, H.E., Fairman, F., Martina, F.,Kashoob, T., Mamash, H. &Cozzolino, L.D. (2013). Microstructure and residual stress improvement in wire and arc additively manufactured parts through high-pressure rolling. *Journal of Materials Processing Technology*, 213(10), pp.1782–1791.
- ConceptLaser (2015).Concept Laser. (Online) Available from: <http://www.concept-laser.de/en/technology/lasercusingr.html> (Accessed February 3, 2015).
- Dabrowski, R. (2011) The kinetics of phase transformations during continuous cooling of the ti6al4v alloy from the single-phase (beta) range. *Archives of Metallurgy and Materials*. 56 (3), pp. 703-707.
- Davis, S. H. Thermocapillary instabilities. *Ann. Rev. Fluid Mech*. 19: 403–435, 1987.
- Denlinger, E.R., Heigel, J.C., Michaleris, P. & Palmer, T.A. (2015).Effect of inter-layer dwell time on distortion and residual stress in additive manufacturing of titanium and nickel alloys. *Journal of Materials Processing Technology*, 215, pp.123–131.
- Donachie, M.J., (2000) Titanium: A Technical Guide 2nd ed., ASM International.
- Du Preez, W. (2014) Qualification of Additive Manufacturing of Ti6Al4V for medical implants and aerospace components. *Ti AM & Design* 001, pp 4-77

Du Preez, W.B & D.J. de Beer (2015) Implementing the South African additive manufacturing technology roadmap - the role of an additive manufacturing centre of competence. *South African Journal of Industrial Engineering*, 26 (2), pp 85-92.

Dynamet-Holdings (2000). Technical Datasheet Ti6Al4V. (Online) Available from: <http://cartech.ides.com> (Accessed February 4, 2015).

Edwards, D. A., Brenner, H., Wassan, D.T. Interfacial transport processes and rheology. *Butterworth Heinemann*, 1991.

Edwards, P. & Ramulu, M. (2014). A Fatigue performance evaluation of selective laser melted Ti – 6Al – 4V. *Materials Science & Engineering*, 598, pp.327–337.

Elmer, J.W., Palmer, T.A., Babu, S.S. & Specht, E.D. (2005). In situ observations of lattice expansion and transformation rates of α and β phases in Ti – 6Al – 4V. *Materials Science and Engineering*, 391, pp.104–113.

Engineering.com (2016) (online) Available from <http://www.eng-tips.com/> (Accessed on 30 January, 2016).

EOS GmbH (2015) Electro Optical Systems (Online) Available from: <http://www.eos.info/> (Accessed on 23 January, 2015).

Fitzpatric, M.E., Fry, A.T., Holdway, P., Kandil, F.A., Shackleton J. and Suominen, L. (2005). Determination of Residual Stresses by X-ray Diffraction. *A National Measurement Good Practice Guide*, 52(2), National Physical Laboratory, Teddington, Middlesex, UK.

Furumoto, T., Ueda, T., Abdul Aziz M.S., Hosokawa, A. & Tanaka, R. (2010). Study on reduction of residual stress induced during rapid tooling process: influence of heating conditions on residual stress. *Key Engineering Materials*, 447-448, pp. 785-789.

Gao, W., Zhang, Y., Ramanujan, D., Ramani, K., Chen, Y., Williams, C.B., Wang, C.C.L., Shin, Y.C., Zhang, S., Zavattieri, P.D. (2015) The status, challenges and future of additive manufacturing in engineering. *Computer-Aided Design*, 69, pp 65-89.

Gray, D.G. (ed.) (1972). *American institute of physics handbook*. McGraw-Hill Book Company, 3rd ed.

Gu, D. & Shen, Y. (2009) Effects of processing parameters on consolidation and microstructure of W–Cu components by DMLS. *Journal of Alloys and Compounds*, 473(1-2), pp.107–115.

Gusarov, A., Malakhova-Ziablova, I., and Pavlov, M., 2013. Thermoelastic residual stresses and deformations at laser treatment. *Physics Procedia*, 41, pp. 889–896.

Gusarov, A.V., Yadroitsev, I., Bertrand, P.H. & Smurov, I. (2007) Heat transfer modelling and stability analysis of selective laser melting. *Applied Surface Science*, 254, pp.975–979.

Hauk, V. (1977). Structural and residual stress analysis by nondestructive methods. *Elsevier*, Amsterdam, 655 p.

He, X., Fuerschbach, P.W., DebRoy, T. (2003) Heat transfer and fluid flow during laser spot welding of 304 stainless steel, *Journal of Physics D: Applied Physics*. 36, 1388–98.

- Hodge, N.E., Ferencz, R. M. and Solberg J. M. 2014. Implementation of a thermo-mechanical model for the simulation of selective laser melting, *Computational Mechanics*, DOI 10.1007/s00466-014-1024-2.
- Hoffman-Innovation (2015) Direct Manufacturing. (Online) Available from: <https://www.hofmann-innovation.com/en/solutions/concept-laser.html> (Accessed February 3, 2015).
- Honeywell (2014) Innovations in Manufacturing. (Online) Available from: www.ornl.gov/manufacturing (Honeywell aerospace) (Accessed May 7, 2015)
- Ilin A, Logvinov R, Kulikov A, Prihodovsky A, Xu H, Ploshikhin V, (2014) Computer aided optimisation of the thermal management during laser beam melting process. *Physics Procedia*, ;56:390–9.
- James, M.N., Hughes, D.J., Chen, Z., Lombard, H., Hattingh, D.G., Asquith, D., Yates J.R. & P.J. Webster, (2007). Residual stresses and fatigue performance. *Engineering Failure Analysis*, 14, pp. 384–395.
- James, M.N., Rall, W.H., Hattingh, D.G. & Steuer, A. (2011) Assessing residual stresses in predicting the service life of welded structures. In: *Fracture and Fatigue of Welded Joints and Structures*, Woodhead Publishing Limited, pp. 276-296.
- James, M.N., Ting S.-P., Bosi M., Lombard, H. & Hattingh D.G.(2009). Residual strain and hardness as predictors of the fatigue ranking of steel welds. *International Journal of Fatigue*, 31, pp. 1366–1377.
- Jardini, A.L., Larosa, M.A., Filho, R.M., Zavalgia, C.A., Bernardes, L.F., Lambert, C.S., Calderoni, D.R. & Kharmandayan, P. (2014) Cranial reconstruction: 3D biomodel and custom-built implant created using additive manufacturing. *Journal of cranio-maxillo-facial surgery* 42(8), pp.1877–84.
- Kasperovich, G. & Hausmann, J. (2015) Improvement of fatigue resistance and ductility of Ti6Al4V processed by selective laser melting. *Journal of Materials Processing Technology*, 220, pp. 202 – 214.
- Kay, D. 2010 Brazing Fundamentals: Differential Metal Expansion. (Online) Available from: <http://www.kaybrazing.com/> (Accessed on May 7, 2015)
- Key to Metals AG, 2015.Key to Metals. (Online) Available from: <http://www.keytometals.com/> (Accessed on May 7, 2015)
- Kim, C.H., Zhang, W., DebRoy, T. (2003) Modeling of temperature field and solidified surface profile during gas-metal arc fillet welding, *Journal of Applied Physics* 94, 2667-79.
- Kim, D.B., Witherell, P. Lipman, R. & Feng, S.C. (2014) Streamlining the additive manufacturing digital spectrum : A systems approach. *Additive Manufacturing*. 17 pp. 1-11.
- Klingbeil, N.W., Beuth, J.L., Chin, R.K. & Amon, C.H. (2002) Residual stress-induced distortion in direct metal solid freeform fabrication. *International Journal of Mechanical Sciences*, 44, pp.57–77.

- Klocke, F., Wagner, C., Ader, C. (2003) Development of an integrated model for selective laser sintering. *Proc. 36th CIRP International Seminar on Manufacturing Systems*, June 3-5, Saarbrücken, Germany, pp. 387-392.
- Knowles, C.R., Becker, T.H. & Tait, R.B. (2012) The effect of heat treatment on residual stress levels within DMLS Ti6Al4V as measured using the hole drilling strain gauge method. *RAPDASA conference*, 5, p.10.
- Kruth, J.P., Deckers, J., Yasa, E. & Wauthle, R. (2012). Assessing and comparing influencing factors of residual stresses in selective laser melting using a novel analysis method, *Proc IMechE Part B: J Engineering Manufacture*, 0(0) 1–12, Catholic University of Leuven 2012, doi: 10.1177/0954405412437085.
- Lackner, M. (2008). *Lasers in Chemistry*, Wiley-VCH, Weinheim, 1466 p.
- Lambda Technologies (2012) (Online) Available from: www.lambdatechs.com (Accessed on 12 April 2015)
- Leuders, S., Thone, M., Reiner, A., Niendorf, T., Troster, T., Richard, H.A. & Maier, H.J. (2013) On the mechanical behaviour of titanium alloy TiAl6V4 manufactured by selective laser melting: Fatigue resistance and crack growth performance. *International Journal of Fatigue*, 48, pp.300–307.
- Li, A., Ji, V., Lebrun, J.L. & Ingelbert, G. (1995) Surface roughness effects on stress determination by the X-ray diffraction method. *Experimental Techniques*, 19(2), pp. 9–11.
- Lide, D.R. (2001). *CRC Handbook of Chemistry and Physics*, 82nd edition. *CRC: Boca Raton*
- Limmaneevichitr, C., Kou, S. (2000) Experiments to simulate effects of Marangoni convection on weld pool shape. *Welding Journal*. 79: 231-237.
- Limmaneevichitr, C., Kou, S. (2000) Visualization of Marangoni convection in simulated weld pools. *Welding Journal*. 79, pp. 126–135.
- Lou, A. & Grosvenor, C. (2012) *Selective Laser Sintering, Birth of an Industry*. Available at: http://www.me.utexas.edu/news/2012/0712_sls_history.php (Accessed January 28, 2015).
- Manfredi, D., Calignano, F., Krishnan, M., Canali, R., Ambrosio, E.P., Biamino, S., Ugues, D., Pavese, M. & Fino, P. (2014) Additive Manufacturing of Al alloys and aluminium matrix composites (AMCs). *INTECH*. pp 1-32
- Matilainen V., Piili H., Salminen A., Syvänen T., Nyrhiläc O. (2014) Characterization of process efficiency improvement in Laser Additive Manufacturing. *Physics Procedia*, 56, pp. 317–26.
- Meada, A., Jin, Y. & Kuboki, T. (2014) Method of reducing residual stress generated by laser cutting by light indentation of sheet metal edge. *Procedia Engineering (11th Int Conference on Technology of Plasticity)*, pp.1-6.
- Meier, H. & Haberland, C.H. (2008) Experimental studies on selective laser melting metallic parts. *Mat.-wiss.u. Werkstofftech*, 39 No. 8. pp. 1-6

- Mercelis, P. & Kruth, J.-P. (2006). Residual stresses in selective laser sintering and selective laser melting. *Rapid Prototyping Journal*, 12 (5), pp. 254 – 265.
- Mills, K.C. 2002. Recommended values of thermo-physical properties for selected commercial alloys. *Woodhead Publishing Ltd*, Cambridge, England, UK.
- Mohanty S. & Hattel J.H. (2014) Numerical model based reliability estimation of selective laser melting process. *Physics. Procedia*, 56, pp. 379–89.
- Murr, L.E., Quinones, S.A., Gaytan, S.M., Lopez, M.I., Rodela, A., Martinez, E.Y., Hernandez, D.H., Martinez, E., Medina, F. & Wicker R.B. (2009) Microstructure and mechanical behaviour of Ti–6Al–4V produced by rapid-layer manufacturing, for biomedical applications. *Journal of Mechanical Behaviour of Biomedical Material*, 2, pp. 20-32.
- Mutombo, K. (2013) Metallurgical evaluation of laser additive manufactured Ti6Al4V components. *MSM/Light Metals CSIR*, pp.4–6.
- Niebling, F., Otto, A. & Geiger M. (2002) Analyzing the DML- process by a macroscopic FE-model. *Solid Freeform Fabrication Symposium*. pp.384–391.
- Olson, M. D., DeWald, A. T., Prime, M. B. & Hill, M. R. (2015) Estimation of uncertainty for contour method residual stress measurements, *Experimental Mechanics*, 55(3), 577-585.
- Pan, Ch. & Lin, T.L. (1989) Marangoni flow on pool boiling near critical heat flux, *International Communications in Heat and Mass Transfer*, 16 (4), pp. 475-486.
- Phenix (2015) Phenix Systems. (Online) Available at: <http://www.phenix-systems.com/en/phenix-systems> (Accessed January 29, 2015).
- Pohl, H., Simchi, A., Issa, M. & Dias, H.C. (2002) Thermal Stresses in Direct Metal Laser Sintering. *Fraunhofer Institute for Manufacturing and Advanced Materials* (Bremen, Germany) pp. 1-7
- Prevey, P.S. (2015) X-ray Diffraction Residual Stress Techniques. (Online) Available from: www.lamdatechs.com (Accessed May 20, 2015)
- Prevey, P.S. (1986) X-ray Diffraction Residual Stress Techniques. In *Metals Handbook* edited by G.M. Crankovic (ASM International), 10, p. 381
- PROTO (2015) Residual Stress Info. Available at: <http://www.protoxrd.com/residual-stress-info.html> (Accessed January 28, 2015).
- Qiu, C., Adkins, N.J.E. & Attallah, M.M. (2013) Microstructure and tensile properties of selectively laser-melted and of HIPed laser-melted Ti–6Al–4V. *Materials Science and Engineering: A*, 578, pp.230–239.
- Quan, Y., Zhang, F., Rebl, H., Nebe, B., Kebler, O. & Burkel, E. (2013) Ti6Al4V foams fabricated by spark plasma sintering with post-heat treatment. *Materials Science and Engineering: A*, 565, pp.118 – 125.
- Rafi, H. *et al.* (2013). Microstructures and mechanical properties of Ti6Al4V parts fabricated by selective laser melting and electron beam melting. *Journal of Materials Engineering and Performance*, 22, pp.3873–3883.

Rangaswamy, P., Prime, M.B., Daymond, M., Bourke, M.A.M., Clausen, B., Choo, H. & Jayaraman, N. (1999) Comparison of residual strains measured by X-ray and neutron diffraction in a titanium (Ti–6Al–4V) matrix composite. *Materials Science and Engineering: A*, 259(2), pp.209–219.

Residual (2015) Residual Stress.(Online) Available from: <http://www.residualstress.org/> (Accessed January 15, 2015).

Roberts, I.A. (2012) Investigation of residual stresses in the laser melting of metal powders in additive layer manufacturing. *Thesis for Doctor of Philosophy (University of Wolverhampton)* pp. 1-246

Rombouts, M., Froyen, L., Gusarov, A.V., Bentefour, E.H. & Glorieux, C. (2004) Photopyroelectric measurement of thermal conductivity of metallic powders. *Journal of Applied Physics*, 97, 024905, pp.1-9.

Sanders, D.J., 1984. Temperature distributions produced by scanning Gaussian laser beams. *Applied Optics*, 23 (1), 30-35.

Sanz, C. & Navas, G. V. (2013) Structural integrity of direct metal laser sintered parts subjected to thermal and finishing treatments. *Journal of Materials Processing Technology*, 213(12), pp.2126–2136.

Scudamore, R., Allison, A. & Stucker, B. (2014). Additive Manufacturing: Strategic Research Agenda. *SRA Agenda*.

Shiomi, M., Osakada, K., Nakamura, K., Yamashita, T. & Abe, F. (2003) Residual stress within metallic model made by selective laser melting process. Institute of Structural and Engineering Materials, *AIST (Nagoya, Japan)*, (1), pp.3–6.

Sternling, C. V. Scriven, L. E. (1959) Interfacial turbulence: hydrodynamic instability and the Marangoni effect. *AIChE J.*, 5, pp. 514–523.

Stresstech (2015) (Online) Available from: <http://www.stresstechgroup.com/> (Accessed on 12 September 2015)

Struers (2015) Streuer Products (Online) Available from: www.struers.com (Accessed on 20 November 2015)

Styger, G., Laubscher, R.F. & Oosthuizen, G. (2014) Effect of constitutive modeling during finite element analysis of machining-induced residual stresses in Ti6Al4V. *Procedia CIRP*, 13, pp.294–301.

Sun, J., Yang, Y. & Wang, D. (2013). Parametric optimization of selective laser melting for forming Ti6Al4V samples by Taguchi method. *Optics & Laser Technology*, 49, pp. 118–24.

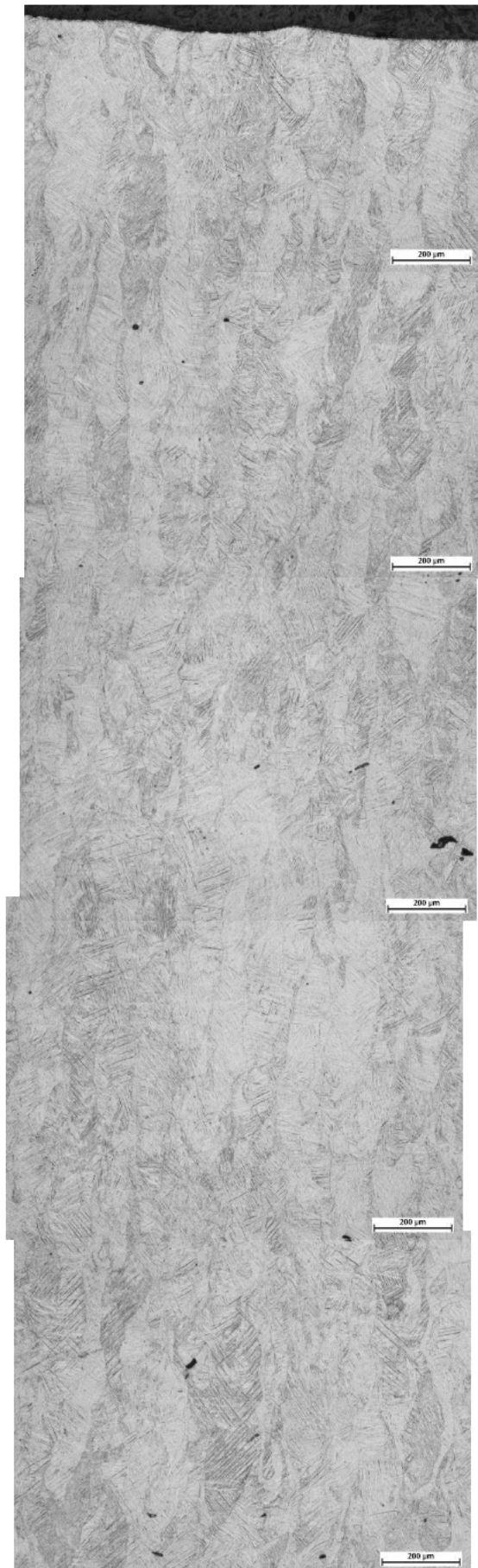
Thijs L, Kempen K, Kruth J-P, Van Humbeeck J. (2013). Fine-structured aluminium products with controllable texture by selective laser melting of pre-alloyed AlSi10Mg powder. *Acta Materialia*, 61, pp. 1809–1819.

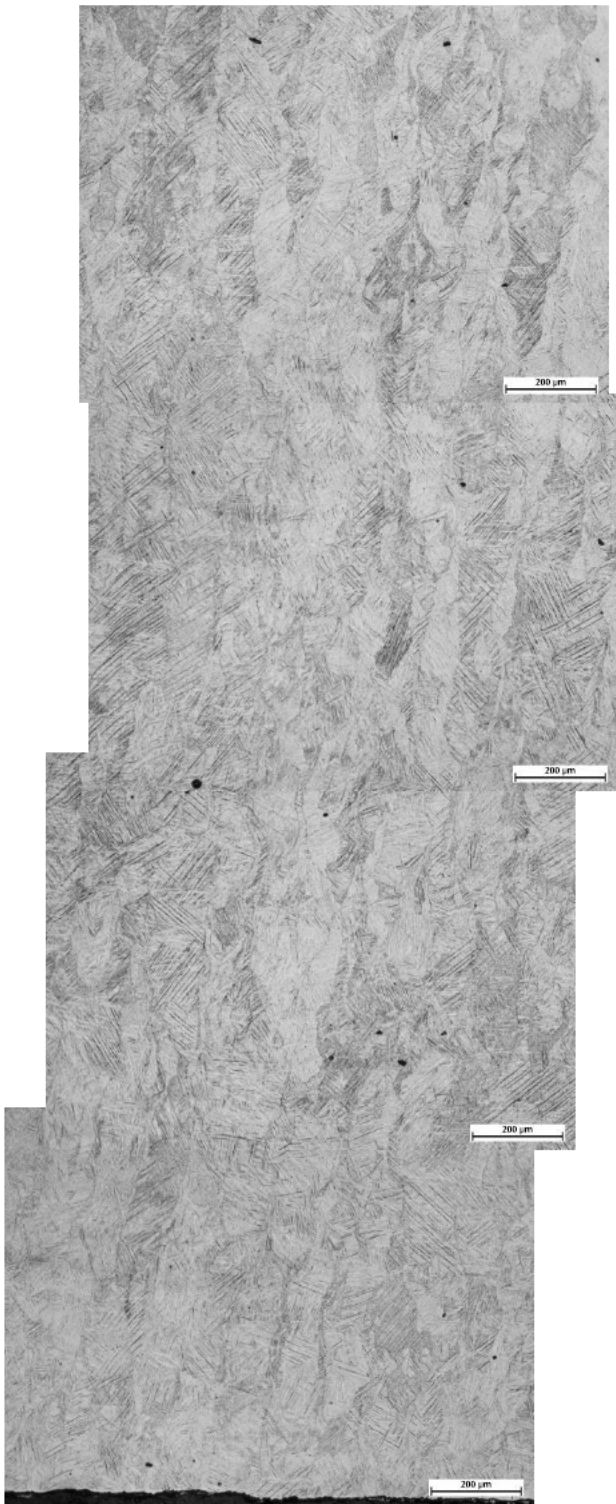
Totten, G., Howes, M. and Inoue, T. (2002). Handbook of residual stress and deformation of steel. *Materials Park, Ohio*, 500 p.

- Vishay Measurements Group, Inc. (1993). Measurement of Residual Stresses by the Hole-Drilling Strain-Gage. *Method Tech Note TN-503-6*. Vishay Measurements Group, Inc., Raleigh, NC. 16 p.
- Vlcak, P., Cerny, F., Drahokoupil, J., Sepitka, J., Tolde, Z. (2015). The microstructure and surface hardness of Ti6Al4V alloy implanted with nitrogen ions at an elevated temperature. *Journal of Alloys and Compounds*, 620, pp. 48–54
- Vrancken, B., Cain, V., Knutsen, R. & Van Humbeeck, J. (2014) Residual stress via the contour method in compact tension specimens produced via selective laser melting. *Scripta Materialia*, 87, pp.29–32.
- Vrancken, B., Thijs, L., Kruth, J.P. & Van Humbeeck, J. (2014) Microstructure and mechanical properties of a novel β titanium metallic composite by selective laser melting. *Acta Materialia*, 68, pp.150–158.
- Vrancken, B., Wauthle, J., Kruth, J.P. & Van Humbeeck, J. (2013) Study of the influence of material properties in selective laser melting. *LayerWise NV*, pp.131–139.
- Wang D, Yang Y, Liu R, Xiao D, Sun J. (2013) Study on the designing rules and process ability of porous structure based on selective laser melting (SLM). *Journal of Materials Processing Technology*. 213, pp. 1734–42
- Withers, P. J. and Bhadeshia, H. K. D. H. (2001). Residual stress. *Materials Science and Technology*, 17, pp. 355-375.
- Wycisk, E., Solbach, A., Siddique, S., Herzog, D., Walther, F. & Emmelmann, C. (2014) Effects of defects in laser additive manufactured TI-6AL-4V on fatigue properties. *Physica Procedia*, 56, pp.371–378.
- Xu, W., Sun, S., Elambasseril, J., Liu, Q., Brandt, M., Qian, M. (2015). Ti-6Al-4V Additively Manufactured by Selective Laser Melting with Superior Mechanical Properties. *JOM*, pp. 668–673.
- Yadroitsava, I., Els J., Booyesen G., Yadroitsev I., (2015). Peculiarities of single track formation from TI6AL4V alloy at different laser power densities by SLM. *South African Journal of Industrial Engineering*, 26 (3), pp. 86-95.
- Yadroitsava, I., Grewar, S., Hattingh D., Yadroitsev I., (2015). Residual stress in SLM Ti6Al4V alloy specimens, *Materials Science Forum*, 828-829, pp. 305-310.
- Yadroitsev, I. & Yadroitsava, I., (2015). Evaluation of residual stress in stainless steel 316L and Ti6Al4V samples produced by selective laser melting, *Virtual and Physical Prototyping*, 10 (2), pp. 67-76.
- Yadroitsava, I. & Yadroitsev, I. (2015) Residual stress in metal specimens produced by Direct Metal Laser Sintering. *International Solid Freeform Fabrication Symposium*, University of Texas at Austin, USA.
- Yadroitsev I. (2009). Selective laser melting: direct manufacturing of 3D-objects by selective laser melting of metal powders. Saarbrücken: *LAP Lambert Academic Publishing AG & Co. KG*; 307 p.

- Yadroitsev I., Gusarov A., Yadroitsava I., Smurov I. (2010). Single track formation in selective laser melting of metal powders. *Journal of Materials Processing Technology*; 210, pp. 1624–31.
- Yadroitsev I., Yadroitsava I., Ph. Bertrand, Smurov I. (2012) Factor analysis of selective laser melting process parameters and geometrical characteristics of synthesized single tracks. *Rapid Prototyping Journal*, 18, pp. 201–208.
- Yadroitsev, I., Bertrand, P. & Smurov, I. (2007). Parametric analysis of the selective laser melting process. *Applied Surface Science*, 253, pp.8064–8069.
- Yadroitsev, I., Krakhmalev, P. & Yadroitsava, I. (2015) Hierarchical design principles of selective laser melting for high quality metallic objects. *Additive Manufacturing*, 7, pp. 45-56.
- Yadroitsev, I., Krakhmalev, P. and Yadroitsava, I. (2014). Selective laser melting of Ti6Al4V alloy for biomedical applications: temperature monitoring and microstructural evolution, *Journal of Alloys and Compounds*, 583, pp 404-409.
- Yasa, E., Deckers, J. & Kruth J-P. (2011) The investigation of the influence of laser re-melting on density, surface quality and microstructure of selective laser melting parts. *Rapid Prototyping Journal*, 17, pp.312–27.
- Zaeh, M.F. and Branner, G. (2010) Investigation on residual stresses and deformation in selective laser melting. *Production Engineering*, 4(1), pp. 35-45
- Zhang, S., Wei, Q., Chen, L., Li, S. & Shi, Y. (2014) Effects of scan line spacing on pore characteristics and mechanical properties of porous Ti6Al4V implants fabricated by selective laser melting. *Materials & Design*, 63, pp.185–193.
- Zhang, W., Kim, C.H., Debroy, T. (2004) Heat and fluid flow in complex joints during gas metal arc welding – Part II: Application to fillet welding of mild steel, *Journal of Applied Physics*. 95, 5220-29.

Appendix 1. Cross-section (in the building direction) of the middle block of the cantilever





Appendix 2. Normal and principal stresses near the surface in Ti6Al4V (ELI) DMLS samples

Sample №1

Stress Tensor			Error		
468.01	-156.57	-2.81	7.78	8.66	2.16
	347.68	-53.1		7.78	2.16
		0			4.29
<i>Principal Stress Max :</i>	575.57	s ₁			
<i>Principal Stress Min :</i>	240.11	s ₂			
<i>Direction Of Principal Stress :</i>	-34.49	α			
<i>Max Shear Stress :</i>	167.73				

Sample №2

Stress Tensor			Error		
552.98	-142.93	-6.71	1.83	2.04	0.51
	286.24	-23.43		1.83	0.51
		0			1.01
<i>Principal Stress Max :</i>	615.09	s ₁			
<i>Principal Stress Min :</i>	224.12	s ₂			
<i>Direction Of Principal Stress :</i>	-23.49	α			
<i>Max Shear Stress :</i>	195.49				

Sample №3

Stress Tensor			Error		
476.03	120.67	-13.36	1.17	1.25	0.27
	641.82	-1.14		1.17	0.27
		0			0.64
<i>Principal Stress Max :</i>	705.33	s ₁			
<i>Principal Stress Min :</i>	412.53	s ₂			
<i>Direction Of Principal Stress :</i>	-27.76	α			
<i>Max Shear Stress :</i>	146.4				

Sample №4

Stress Tensor			Error		
339.4	335.13	87.06	17.44	18.62	4.07

	520.76	4.21		17.44	4.07
		0			9.59
<i>Principal Stress Max :</i>	777.26	s₁			
<i>Principal Stress Min :</i>	82.9	s₂			
<i>Direction Of Principal Stress :</i>	-37.43	α			
<i>Max Shear Stress :</i>	347.18				

Sample №5

Stress Tensor			Error		
	429.49	-116.32	7.94	8.48	1.85
		476.29	26.6	7.94	1.85
		0	0		4.37
<i>Principal Stress Max :</i>	571.54	s₁			
<i>Principal Stress Min :</i>	334.24	s₂			
<i>Direction Of Principal Stress :</i>	39.31	α			
<i>Max Shear Stress :</i>	118.65				

Sample №6

Stress Tensor			Error		
	804.75	-94.45	6.03	6.44	1.41
		372.16	-26.3	6.03	1.41
		0	0		3.32
<i>Principal Stress Max :</i>	824.48	s₁			
<i>Principal Stress Min :</i>	352.44	s₂			
<i>Direction Of Principal Stress :</i>	-11.79	α			
<i>Max Shear Stress :</i>	236.02				

Sample №7

Stress Tensor			Error		
	325.99	50.74	10.24	10.94	2.39
		571.95	5.93	10.24	2.39
		0	0		5.63
<i>Principal Stress Max :</i>	582	s₁			
<i>Principal Stress Min :</i>	315.94	s₂			
<i>Direction Of Principal Stress :</i>	-11.21	α			

Max Shear Stress : 133.03

Sample №8

Stress Tensor

				Error		
467.66	262.31	188.42	28.75	31.5	7.88	
	633.41	8.91		28.72	7.93	
		0			15.7	

Principal Stress Max : 825.63 **s₁**

Principal Stress Min : 275.44 **s₂**

Direction Of Principal Stress : -36.23 **α**

Max Shear Stress : 275.09

Sample №9

Stress Tensor

				Error		
393.5	12.29	72.81	20.21	22.12	5.75	
	470.04	-26.13		19.93	5.52	
		0			11.07	

Principal Stress Max : 471.97 **s₁**

Principal Stress Min : 391.58 **s₂**

Direction Of Principal Stress : -8.9 **α**

Max Shear Stress : 40.19

Sample №10

Stress Tensor

				Error		
523.63	132.45	-16.7	29.07	32.33	8.07	
	581.89	19.27		29.07	8.07	
		0			16.04	

Principal Stress Max : 688.38 **s₁**

Principal Stress Min : 417.14 **s₂**

Direction Of Principal Stress : -38.8 **α**

Max Shear Stress : 135.62

Sample №11a

Stress Tensor

				Error		
387.1	-130.14	-11.94	5.33	5.93	1.48	
	193.54	-36.66		5.33	1.48	
		0			2.94	

<i>Principal Stress Max :</i>	452.49	s₁
<i>Principal Stress Min :</i>	128.14	s₂
<i>Direction Of Principal Stress :</i>	-26.68	α
<i>Max Shear Stress :</i>	162.18	

Sample №11b

Stress Tensor				Error		
	399.01	-138.47	-38.2	26.84	29.85	7.45
		245.04	-19.79		26.84	7.45
			0			14.81
<i>Principal Stress Max :</i>	480.46	s₁				
<i>Principal Stress Min :</i>	163.59	s₂				
<i>Direction Of Principal Stress :</i>	-30.46	α				
<i>Max Shear Stress :</i>	158.43					

Sample №11c

Stress Tensor				Error		
	461.86	-161.85	-12.32	5.6	6.23	1.55
		215.34	-33.35		5.6	1.55
			0			3.09
<i>Principal Stress Max :</i>	542.04	s₁				
<i>Principal Stress Min :</i>	135.16	s₂				
<i>Direction Of Principal Stress :</i>	-26.35	α				
<i>Max Shear Stress :</i>	203.44					

Sample №12a

Stress Tensor				Error		
	382.65	-151.68	-15.61	12.9	14.35	3.58
		143.09	-38.03		12.9	3.58
			0			7.12
<i>Principal Stress Max :</i>	456.14	s₁				
<i>Principal Stress Min :</i>	69.6	s₂				
<i>Direction Of Principal Stress :</i>	-25.85	α				
<i>Max Shear Stress :</i>	193.27					

Sample №12b

Stress Tensor			Error		
366.15	-139.61	-22.46	24.08	26.78	6.69
	210.75	-2.82		24.08	6.69
		0			13.28
<i>Principal Stress Max :</i>	448.22	s₁			
<i>Principal Stress Min :</i>	128.68	s₂			
<i>Direction Of Principal Stress :</i>	-30.45	α			
<i>Max Shear Stress :</i>	159.77				

Sample №112c

Stress Tensor			Error		
436.94	-150.55	-20.9	3.41	3.79	0.95
	200.68	-31.58		3.41	0.95
		0			1.88
<i>Principal Stress Max :</i>	510.17	s₁			
<i>Principal Stress Min :</i>	127.45	s₂			
<i>Direction Of Principal Stress :</i>	-25.94	α			
<i>Max Shear Stress :</i>	191.36				

Sample №13a

Stress Tensor			Error		
377.68	90.61	4.65	10.86	12.08	3.02
	285.04	0.53		10.86	3.02
		0			5.99
<i>Principal Stress Max :</i>	433.12	s₁			
<i>Principal Stress Min :</i>	229.59	s₂			
<i>Direction Of Principal Stress :</i>	31.46	α			
<i>Max Shear Stress :</i>	101.77				

Sample №13b

Stress Tensor			Error		
368.96	86.05	-13.23	22.97	25.54	6.38
	384.46	-16.68		22.97	6.38
		0			12.67

<i>Principal Stress Max :</i>	463.11	s₁
<i>Principal Stress Min :</i>	290.31	s₂
<i>Direction Of Principal Stress :</i>	-42.43	α
<i>Max Shear Stress :</i>	86.4	

Sample №13c

Stress Tensor				Error		
	724.96	-81.61	93.65	1.53	1.7	0.43
		497.87	-53.24		1.53	0.43
			0			0.85
<i>Principal Stress Max :</i>	751.25	s₁				
<i>Principal Stress Min :</i>	471.59	s₂				
<i>Direction Of Principal Stress :</i>	-17.85	α				
<i>Max Shear Stress :</i>	139.83					

Sample №14

Stress Tensor				Error		
	446.1	50.25	-21.43	4.9	5.44	1.36
		650.01	-43.16		4.9	1.36
			0			2.7
<i>Principal Stress Max :</i>	661.72	s₁				
<i>Principal Stress Min :</i>	434.39	s₂				
<i>Direction Of Principal Stress :</i>	-13.12	α				
<i>Max Shear Stress :</i>	113.66					

Sample №15

Stress Tensor				Error		
	423.27	-151.58	-19.15	16.72	18.6	4.64
		437.86	-40.74		16.72	4.64
			0			9.23
<i>Principal Stress Max :</i>	582.32	s₁				
<i>Principal Stress Min :</i>	278.81	s₂				
<i>Direction Of Principal Stress :</i>	43.62	α				
<i>Max Shear Stress :</i>	151.76					

Sample №16a

Stress Tensor			Error		
330.96	56.21	7.55	16.12	17.93	4.47
	613.94	-17.25		16.12	4.47
		0			8.89
<i>Principal Stress Max :</i>	624.7	s₁			
<i>Principal Stress Min :</i>	320.2	s₂			
<i>Direction Of Principal Stress :</i>	-10.83	α			
<i>Max Shear Stress :</i>	152.25				

Sample №16b

Stress Tensor			Error		
263.14	-31.88	27.84	17.85	19.85	4.95
	685.3	-128.67		17.85	4.95
		0			9.85
<i>Principal Stress Max :</i>	687.69	s₁			
<i>Principal Stress Min :</i>	260.75	s₂			
<i>Direction Of Principal Stress :</i>	4.29	α			
<i>Max Shear Stress :</i>	213.47				

Sample №16c

Stress Tensor			Error		
450.27	-138.94	-23.54	29.3	32.58	8.13
	178.54	-30.51		29.3	8.13
		0			16.16
<i>Principal Stress Max :</i>	508.73	s₁			
<i>Principal Stress Min :</i>	120.08	s₂			
<i>Direction Of Principal Stress :</i>	-22.82	α			
<i>Max Shear Stress :</i>	194.33				

Sample №17

Stress Tensor			Error		
306.53	195.46	-19.28	39.25	43.51	10.86
	388.91	34.72		39.25	10.86
		0			21.61

<i>Principal Stress Max :</i>	547.48	S1
<i>Principal Stress Min :</i>	147.97	S2
<i>Direction Of Principal Stress :</i>	-39.05	α
<i>Max Shear Stress :</i>	199.75	

Sample №18

Stress Tensor				Error		
	315.31	-5.88	28.79	19.31	21.47	5.36
		191.68	6.74		19.31	5.36
			0			10.65
<i>Principal Stress Max :</i>	315.59	S1				
<i>Principal Stress Min :</i>	191.4	S2				
<i>Direction Of Principal Stress :</i>	-2.72	α				
<i>Max Shear Stress :</i>	62.09					

Sample №19

Stress Tensor				Error		
	487.55	-128.88	29.28	8.99	10	2.5
		536.54	-7.31		8.99	2.5
			0			4.96
<i>Principal Stress Max :</i>	643.23	S1				
<i>Principal Stress Min :</i>	380.86	S2				
<i>Direction Of Principal Stress :</i>	39.62	α				
<i>Max Shear Stress :</i>	131.18					

Sample №20

Stress Tensor				Error		
	261.56	3.89	16.21	19.18	21.33	5.32
		578.13	-32.41		19.18	5.32
			0			10.58
<i>Principal Stress Max :</i>	578.18	S1				
<i>Principal Stress Min :</i>	261.51	S2				
<i>Direction Of Principal Stress :</i>	-0.7	α				
<i>Max Shear Stress :</i>	158.33					

Sample №21

Stress Tensor			Error			
	530.33	-122.51	98.99	11.49	12.78	3.19
		475.36	-71.21		11.49	3.19
			0			6.34
<i>Principal Stress Max :</i>	628.4		s₁			
<i>Principal Stress Min :</i>	377.29		s₂			
<i>Direction Of Principal Stress :</i>	-38.68		α			
<i>Max Shear Stress :</i>	125.55					

Sample №23

Stress Tensor			Error			
	392.05	285	57.65	10.78	11.39	2.42
		759.93	99.24		10.78	2.42
			0			5.93
<i>Principal Stress Max :</i>	915.2		s₁			
<i>Principal Stress Min :</i>	236.79		s₂			
<i>Direction Of Principal Stress :</i>	-28.58		α			
<i>Max Shear Stress :</i>	339.2					

Sample №24a

Stress Tensor			Error			
	765.37	-317.04	47.93	40.9	45.54	11.38
		635.18	-60.07		40.95	11.59
			0			22.59
<i>Principal Stress Max :</i>	1023.93		s₁			
<i>Principal Stress Min :</i>	376.62		s₂			
<i>Direction Of Principal Stress :</i>	-39.2		α			
<i>Max Shear Stress :</i>	323.66					

Sample №24b

Stress Tensor			Error			
	559.5	10.65	-32.5	28.94	32.37	8.07
		619.68	8.5		29.37	8.34
			0			16.11
<i>Principal Stress Max :</i>	621.51		s₁			
<i>Principal Stress Min :</i>	557.67		s₂			

Direction Of Principal Stress : -9.75
 α
Max Shear Stress : 31.92

Sample №24c

Stress Tensor				Error		
	273.23	-238.12	31.47	1.89	2.1	0.52
		675.63	5.1		1.89	0.52
			0			1.04
<i>Principal Stress Max :</i>	786.17		s1			
<i>Principal Stress Min :</i>	162.69		s2			
<i>Direction Of Principal Stress</i> :	24.9		α			
<i>Max Shear Stress :</i>	311.74					

....

Appendix 3. Roughness of the top surface of DMLS samples (μm)

Sample No.	Ra 0°	Ra 90°	Average \pm S.D.	Rz 0°	Rz 90°	Average \pm S.D.
1	1.4	1.5	1.5 \pm 0.05	5.5	7.0	6.1 \pm 0.61
1	1.4	1.5		5.7	6.4	
1	1.4	1.5		5.5	6.2	
2	5.7	5.7	5.4 \pm 0.39	29.8	27.9	29 \pm 0.97
2	5.4	4.9		29.7	28.4	
2	5.7	4.9		28.3	30.2	
4	3.7	4.1	4.1 \pm 0.87	20.1	23.3	22.1 \pm 2.56
4	3.7	3.7		20.2	20.1	
4	5.9	3.7		26.5	22.6	
5	4.2	6.4	4.8 \pm 1.22	19.9	30.0	22.6 \pm 5.74
5	3.6	4.2		18.8	18.7	
5	4.1	6.4		18.3	30.0	
6	4.3	4.6	4.4 \pm 0.15	23.4	27.5	23.9 \pm 2.52
6	4.4	4.4		23.0	25.6	
6	4.2	4.3		20.1	23.6	
8	5.3	5.2	4.5 \pm 0.66	27.8	29.0	22.8 \pm 3.73
8	4.1	4.1		20.8	20.1	
8	4.6	3.5		20.9	18.9	
8	5.0	4.0		23.6	21.2	
9	3.3	4.6	4.3 \pm 0.66	17.6	22.6	21.8 \pm 3.65
9	5.3	4.1		26.3	19.6	
9	4.1	4.6		19.3	24.1	
9	3.5	4.8		18.1	26.7	
11	1.5	1.6	1.5 \pm 0.05	5.6	6.2	6.0 \pm 0.472
11	1.5	1.6		5.4	6.8	
11	1.5	1.5		6.1	6.1	
12	2.1	2.3	2.0 \pm 0.22	11.7	11.6	10.9 \pm 0.97
12	1.7	2.1		9.3	10.4	
12	1.9	2.0		10.5	11.7	
14	4.5	3.4	3.7 \pm 0.59	25.6	17.3	19.5 \pm 3.89
14	3.8	2.8		20.0	13.8	
14	3.8	4.0		20.5	19.6	
16	4.3	3.9	4.2 \pm 0.79	20.9	26.1	22.3 \pm 4.25
16	4.8	3.9		25.4	19.2	
16	3.3	4.6		18.7	26.3	
16	5.7	5.0		27.9	24.3	
16	3.8	3.1		18.7	15.3	
Substrate	1.0	0.3	0.7 \pm 0.32	5.4	1.9	4.0 \pm 1.83
	0.8	0.6		5.7	3.1	

Appendix 4. Vickers microhardness of as-built samples (HV_{0.3})

№ of indentation	XZ plane	XY plane	YZ plane
1	393	374	406
2	363	377	379
3	363	382	390
4	355	376	380
5	349	385	420
6	390	395	399
7	388	369	396
8	403	393	396
9	378	374	392
10	431	363	381
11	383	384	376
12	378	383	387
13	380	389	417
14	406	396	378
15	378	377	389
16	403	414	387
17	392	405	380
18	400	389	398
19	401	393	397
20	379	393	372
21	399	380	383
22	422	380	385
23	398	398	385
24	379	373	379
25	372	388	402
26	389	405	397
27	391	398	406
28	401	398	395
29	392	398	395
30	432	379	395
Average	390	387	391
S.D.	19.5	11.9	11.6
	389±14.8		

Appendix 5. Vickers microhardness of stress-relieved samples

№ of indentation	HV_{0.3}
1	375
2	394
3	392
4	395
5	370
6	395
7	395
8	369
9	391
10	380
11	364
12	374
13	359
14	371
15	350
16	381
17	380
18	370
19	396
20	378
21	390
22	355
23	356
24	363
25	335
26	347
27	347
28	384
29	390
30	384
Average ±S.D.	374±17

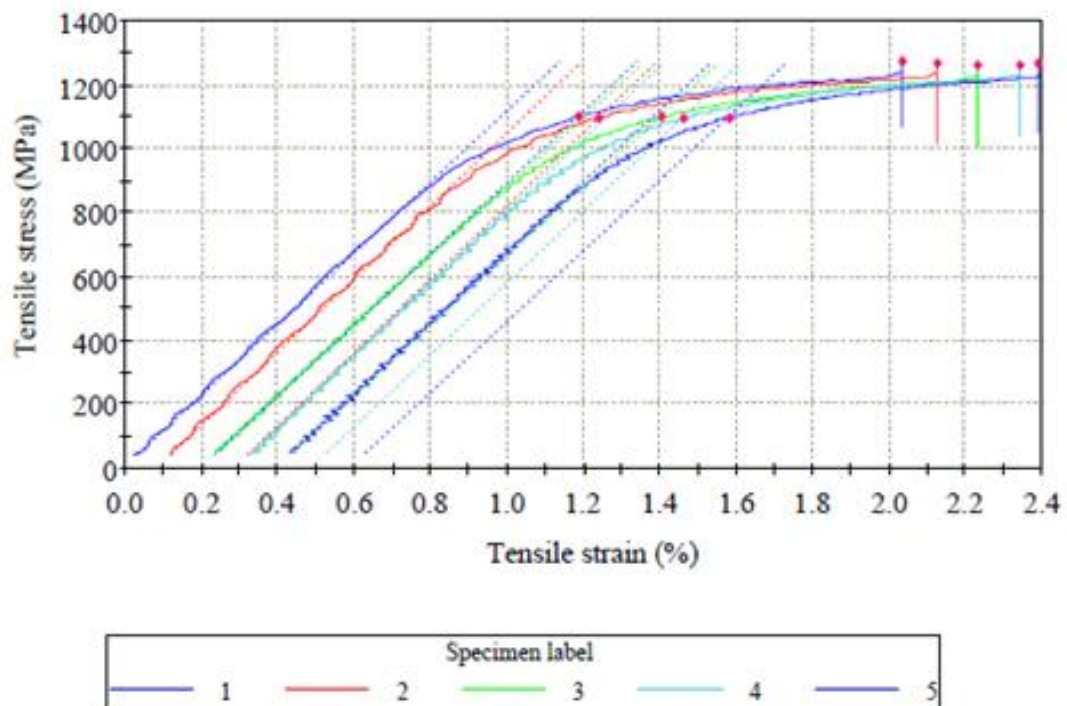
Appendix 6. Mechanical properties of as-built horizontal samples

Report No.:	
Laboratory Name	CSIR Materials Testing Laboratory
Company	CUT
Operator ID	203406
Method description	LM-WP-402 - ASTM E8 M
Sample description	Ti6Al4V
Test Date	14/12/2015

	Specimen label	Area (mm ²)	Tensile stress at Yield (Offset 0.2 %) (MPa)	Modulus (Chord 200 MPa - 800 MPa) (GPa)	UTS (MPa)	Elongation (%) 4-D	Area Reduction (%)
	1	14.79	1100.66	111.2	1271.24	8.83	24.94
	2	14.79	1095.97	114.6	1265.91	9.09	25.34
	3	14.73	1098.69	109.1	1259.32	9.80	29.33
	4	14.73	1096.31	113.0	1260.75	9.70	25.79
	5	14.66	1096.56	110.9	1265.51	9.55	22.63
Mean		14.74	1097.64	111.8	1264.75	9.40	25.61
Coefficient of Variation		0.386	0.182	1.888	0.381	4.436	9.427
Range		0.14	4.70	5.5	11.92	0.97	6.71
Standard Deviation		0.057	1.999	2.110	4.819	0.417	2.414
Minimum		14.66	1095.97	109.1	1259.32	8.83	22.63
Maximum		14.79	1100.66	114.6	1271.24	9.80	29.33
Median		14.73	1096.56	111.2	1265.51	9.55	25.34

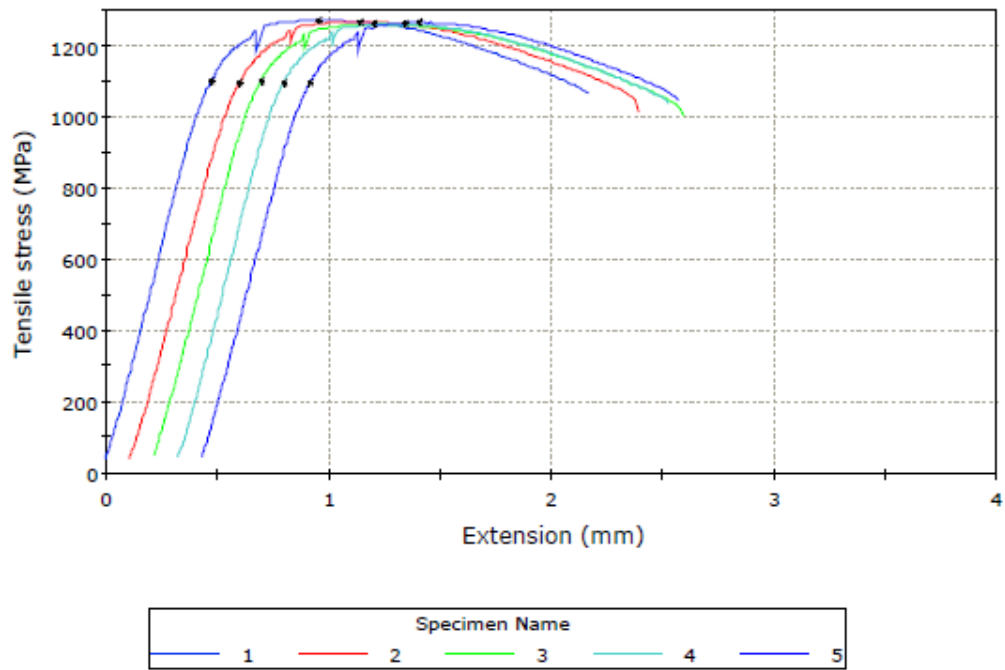
Graph 1

Specimen 1 to 5



Graph 2

Specimen 1 to 5



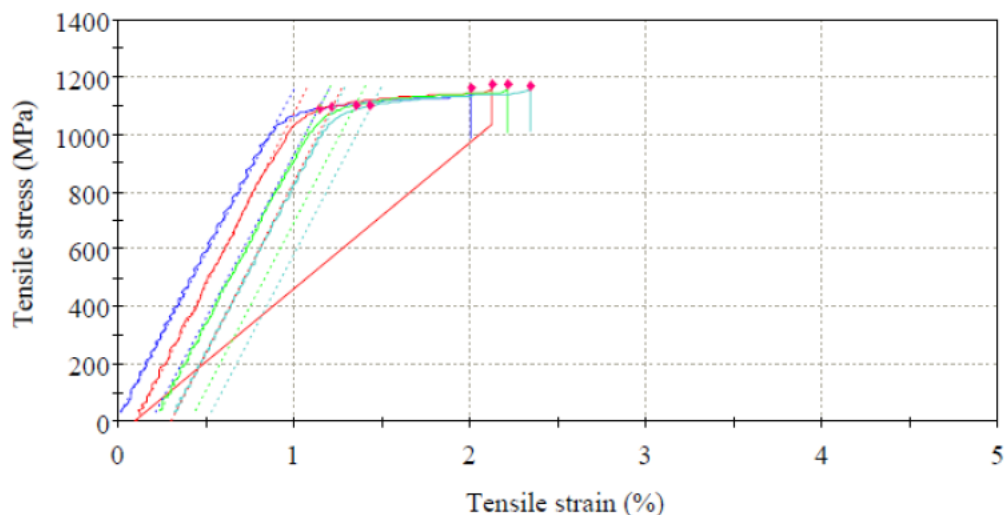
Appendix 7. Mechanical properties of the stress-relieved samples

Report No.:	
Laboratory Name	CSIR Materials Testing Laboratory
Company	CUT
Operator ID	203406
Method description	LM-WP-402 - ASTM E8 M
Sample description	Ti6Al4V-650Deg-3hrs stress relieved
Test Date	15/02/2016

	Specimen label	Area (mm ²)	Tensile stress at Yield (Offset 0.2 %) (MPa)	Modulus (Chord 200 MPa - 800 MPa) (GPa)	UTS (MPa)	Elongation (%) 4.D	Area Reduction (%)
1	Horizontal-650-3hrs-1	19.63	1090.07	114.0	1160.10	10.81	30.44
2	Horizontal-650-3hrs-2	19.40	1097.88	120.0	1172.98	10.26	28.59
3	Horizontal-650-3hrs-3	19.48	1103.60	116.4	1173.60	10.71	29.21
4	Horizontal-650-3hrs-4	19.48	1099.24	117.7	1170.53	10.66	28.53
Mean		19.50	1097.70	117.0	1169.30	10.61	29.19
Coefficient of Variation		0.505	0.514	2.154	0.537	2.279	3.045
Range		0.23	13.53	6.0	13.51	0.55	1.91
Standard Deviation		0.099	5.639	2.520	6.278	0.242	0.889
Minimum		19.40	1090.07	114.0	1160.10	10.26	28.53
Maximum		19.63	1103.60	120.0	1173.60	10.81	30.44
Median		19.48	1098.56	117.1	1171.75	10.68	28.90

Graph 1

Specimen 1 to 4



Specimen label			
—	Horizontal-650-3hrs-1	—	Horizontal-650-3hrs-2
—	Horizontal-650-3hrs-3	—	Horizontal-650-3hrs-4

Graph 2

Specimen 1 to 4

